Dissertation

submitted to the

Combined Faculties of the Natural Sciences and Mathematics

of the Ruperto - Carola University of Heidelberg, Germany

for the degree of

Doctor of Natural Sciences

Put forward by

Rahul Vasudev Nair Kannan

born in Chennai, India

Oral examination: June 27th, 2014

Hydrodynamic simulations of galaxy formation in a cosmological context

Referees: Dr. Andrea Valerio Macciò
Prof. Dr. Volker Springel

Hydrodynamic simulations of galaxy formation in a cosmological context

Abstract: The formation of galaxies and their subsequent evolution through cosmic time is governed by a variety of complex physical processes such as gas cooling, star formation, feedback and galaxy mergers. This thesis studies these effects on galaxy properties using hydrodynamical simulations. The first part explores the effect of mergers on the morphology of galaxies beginning with the question of whether small mergers can create holes in the gas distribution. I follow this with a look at how major mergers form galactic spheroids. The second part of the thesis shifts to examining the role of stellar feedback in regulating star formation. A cosmological volume is presented that includes pre-supernova stellar feedback in addition to supernova feedback. The statistical properties of the galaxies in the volume compare well with the observed ones. Finally, we introduce a new, computationally efficient model to calculate the gas cooling rate in the presence of local radiation fields. The model uses simple assumptions for radiative transfer to propagate local photoionizing radiation throughout the entire simulation volume. The new method shows promise as a preventive feedback that regulates the star formation rate of $L_\star$ galaxies by reducing gas accretion rather than resorting to explosive energy input from stars.

Hydrodynamische Simulationen von Galaxienentstehung unter kosmologischen Rahmenbedingungen

Zusammenfassung: Die Entstehung von Galaxien und deren Entwicklung wird durch eine Vielzahl komplexer physikalischer Phänomene bestimmt. Dazu gehören Kühlprozesse von Gasen, die Entstehung von Sternen und deren Wechselwirkung mit interstellarer Materie sowie Galaxienzusammenstöße. Diese Arbeit befasst sich mit den Konsequenzen dieser Phänomene für die Eigenschaften von Galaxien anhand von Ergebnissen hydrodynamischer Simulationen. Zunächst werden die Auswirkungen von Galaxienzusammenstößen untersucht. Dabei soll beantwortet werden, ob kleine Zusammenstöße gasfreie Löcher erzeugen und ob durch große Zusammenstöße Halos entstehen können. Der zweite Teil der Arbeit beschäftigt sich damit, welche Rolle die Wechselwirkung der Sternpopulation mit der interstellaren Materie für die Regulation der Sternenstehungsrate spielt. Ich beschreibe die statistischen Eigenschaften von Galaxien in einem Ausschnitt des Universums. Dieser wurde unter Berücksichtigung der Auswirkungen von Sternwinden und Supernovaexplosionen simuliert. Die Ergebnisse stimmen mit entsprechenden Beobachtungen überein. Abschließend wird ein neues Modell zur Berechnung der Gaskühlrate unter dem Einfluss lokaler Strahlungsquellen vorgestellt. Es bedient sich einfacher Annahmen für Strahlungstransportprozesse und benötigt verleichsweise geringe Rechenleistung um die lokale Ausbreitung photoionisierender Strahlung zu modellieren. Im

Gegensatz zur Rückkopplung der stellaren Population wird mit dieser Methode die Sternentstehung durch eine Verringerung der Gasakkretion reguliert und bietet somit eine vielversprechende Möglichkeit zur Regulierung der Sternpopulation von $L_\star$ Galaxien.

कॊ ।आद्धा वेद क।इह प्रवॊचत् कुत ।आअजाता कुत ।इयं विसृष्टि: ।
अर्वाग्देवा ।आस्य विसर्जनेनाथाकॊ वेद यत ।आबभूव ॥

इयं विसृष्टिर्यत ।आबभूव यदि वा दधे यदि वा न ।
यॊ ।आस्याध्यक्ष: परमे व्यॊमन्त्सॊ आंग वेद यदि वा न वेद ॥

Who really knows and who can say?
Whence was it produced and whence came this creation?
The Gods came later, with the creation of this Universe.
Who then knows whence it first came into being?
Whence this creation has arisen?
Perhaps it formed itself, perhaps it did not.
The One who surveys it all from his highest heaven,
only He knows, or perhaps even He does not.

Creation hymn in Rig Veda (10:129) - Translated by W. Doniger O'Flaherty

Contents

List of Figures

List of Tables

Chapter 1

Introduction

Astronomy is one of the oldest sciences. Since the beginning, mankind has been fascinated by the night sky. Many ancient astronomers looked up into the night sky and wondered how the objects came to be and what the Earth's place was in the cosmos. The sky was a mystical place associated with gods and spirits for ancient cultures around the world. In western thought, the Earth remained as the center of the cosmos for many centuries. In the 4^{th} century B.C., the Greek astronomers had realized that the Sun, Moon, planets and stars move together through the sky each day. This led Plato to believe that the 'heavens' revolved around a round Earth located at the center of the Universe.

This geocentric view persisted until the 16^{th} Century when Nicolaus Copernicus postulated that a Universe with the Sun at the center and planets revolving around it and the Moon revolving around the rotating Earth (Heliocentric theory) provided a far simpler explanation of the planetary motions. During the course of the seventeenth century, this theory gained widespread acceptance helped by the observations of Galileo Galilei and theory of Sir Isaac Newton. Galileo discovered the four large moons of Jupiter, which provided a useful analog of the Earth-Moon system. Sir Isaac Newton provided a mathematical explanation that linked the motions of such bodies with the force that causes an apple to fall from a tree, gravity. Newton postulated that gravity attracts any two bodies together as the inverse square of their separation and directly proportional to their masses. His theory of gravity provided the necessary mathematical framework for describing and predicting the motion of celestial bodies.

In the eighteenth century, William Herschel observed diffuse patches of light which he called 'nebulae'. He considered these to be island universes. He argued that the Milky-Way was a separate disc shaped island universe with the Sun in the center. He considered the other nebulae to be similar systems at large distances.

Whether these island universes were distinct systems or part of the Milky Way was debated until the 1920s. It is epitomized by the Curtis-Shapley debate. Harlow Shapley

favoured a Universe which consisted of only the Milky Way (MW) (Shapley, 1919), whereas Heber Curtis argued that the Milky Way is one of many spiral nebulae in the Universe (Curtis, 1920). The answer to this debate was conclusively established by the work of Edwin Hubble. Hubble identified Cepheid variables in several spiral nebulae, including the Andromeda and Triangulum Nebulae and using the Cepheid period-luminosity relation (Leavitt Law, Leavitt, 1908) he concluded that these nebulae were too distant to be part of the Milky Way and were, in fact, entire island universes outside our own (Hubble, 1925, 1929b). We now recognize these island universes as massive self gravitating systems of stars, gas and dark matter called galaxies.
When Hubble further studied the distinct galaxies, he also discovered that they were not only distant, but also moving rapidly away from us, with a speed proportional to the distance (Hubble, 1929a).

$$v = H_0 d \tag{1.1}$$

This is called Hubble's Law, where H_0 is Hubble constant. Hubble's Law expanded the size of the known Universe and finally changed the paradigm that the Earth was at the center of it. It also provided evidence for the fact that the size of the Universe might not be constant and that an understanding of the evolution of the Universe is required to understand how galaxies grow inside it. The formation and evolution of galaxies in an expanding Universe is one of the most important challenges of modern Astrophysical theory and we will be dealing with parts of this question in this thesis. However, in order to study galaxy formation, we need to know more about the cosmological evolution of the Universe within which galaxies form and evolve.

1.1 Principles of Modern Cosmology

Albert Einstein laid down the foundations of modern theoretical cosmology, with his publication of the cosmological implications of General Relativity (Einstein, 1917). It was known that static Universes are unstable under gravity because gravity has the effect of amplifying small density variations. Therefore a static Universe was in a state of unstable equilibrium. Einstein realized that he could solve this problem by introducing an additional term to his field equations, a cosmological constant Λ.

$$R_{\mu\nu} - \frac{1}{2} R g_{\mu\nu} + \Lambda g_{\mu\nu} = \frac{8\pi G}{c^4} T_{\mu\nu} \tag{1.2}$$

where $R_{\mu\nu}$ is the Ricci curvature tensor, R the Ricci scalar, the $g_{\mu\nu}$ metric tensor, G is Newton's gravitational constant, c the speed of light in vacuum, and $T_{\mu\nu}$ the stress-energy tensor.
The application of this field equation to the entire Universe is accomplished by using two simplifying assumptions: the observable Universe appears to be spatially homogeneous

and isotropic on large scales. Homogeneity implies that the Universe looks the same at each point while isotropy implies that the Universe looks the same in all directions. The most general spacetime metric consistent with homogeneity and isotropy is given by

$$ds^2 = -c^2dt^2 + a(t)^2\left[\frac{dr^2}{1-kr^2} + r^2(d\theta^2 + \sin^2\theta d\phi^2)\right] \tag{1.3}$$

called the Robertson-Walker (RW) metric (Robertson, 1935). This metric is derived from purely geometric considerations, independent of general relativity. The function $a(t)$ is the scale factor which keeps track of the expansion or contraction of the Universe. Geometrically k describes curvature of space, with $k = 1$ corresponding to a closed geometry of the Universe, $k = 0$ a flat geometry and $k = -1$ for an open Universe.
Applying Einstein's equation to the RW metric we get what is known as the Friedmann equations

$$H^2 = \left(\frac{\dot{a}}{a}\right)^2 = \frac{8\pi G}{3}\sum_i \rho_i - \frac{kc^2}{a^2} + \frac{\Lambda c^2}{3} \tag{1.4}$$

where ρ_i denotes all different types of energy in the Universe. We can also derive an acceleration equation given by

$$\frac{\ddot{a}}{a} = \frac{-4\pi G}{3}\sum_i(\rho_i + \frac{3p_i}{c^2}) + \frac{\Lambda c^2}{3} \tag{1.5}$$

where and p_i is the corresponding pressure of the energy density component ρ_i. In fact if we know the energy density components ρ_i, then the evolution of the scale factor, a, can be solved uniquely using only Eq. 1.4, without the need for Eq. 1.5.
With the discovery of the velocity-distance relation by Hubble, Einstein regretted the inclusion of Λ. In 1932 Einstein and de Sitter showed for $\Lambda = 0$ and $k = 0$, we can define a critical density, corresponding to a flat geometry (Einstein & de Sitter, 1932).

$$\sum_i \rho_i = \rho_c = \frac{3H^2}{8\pi G} \tag{1.6}$$

This critical density separates an expanding open and hyperbolic geometries from closed spherical geometries that will eventually collapse. The individual contributions from various density components in the Universe can be quoted as a function of a conveniently defined density parameter

$$\Omega_i = \frac{\rho_i}{\rho_c}|_{z=0} \tag{1.7}$$

defined at the present time. ρ_i and ρ_c are the energy density of the component 'i' and the critical density of the Universe respectively.

1.2 Contents of the Universe

By the end of 1930's it was realized that the solution to the figuring out the evolutionary history of the Universe lay in the determination of the various components of the Friedmann equation such as the present Hubble constant $H_0 = \frac{\dot{a}}{a}|_{z=0}$, the mean density of the Universe and its value compared to the critical density of the Universe, the curvature of the Universe and the value of the cosmological constant.

1.2.1 Baryons

The determination of these parameters turned out to be very difficult observationally. Initially astronomers, in an attempt to measure the mean density of the Universe, started to measure the mass of all the stars in the galactic neighbourhood. This had been done by a lot of researches and the value they obtained was way below the critical value.

$$\Omega_{stars} \sim 0.005 \pm 0.005 \tag{1.8}$$

However stars are not the only ordinary (or baryonic) matter in the Universe. There is a substantial amount of gas in the Universe that has not yet been converted into stars. Directly measuring the Ω_{gas} is quite complicated. Fortunately the theory of Big Bang Nucleosynthesis (BBN) which was advocated and developed by George Gamow and his associates had the ability to predict the mass content of baryons in the Universe. BBN is believed to be responsible for the formation of most of light elements other than Hydrogen in the Universe. The initial calculations were performed by Alpher et al. (1948) under the assumption of a free sea of neutrons and that the nucleosynthesis only took place when the temperature had fallen below $k_B T = 0.1$ Mev. The theory proposed that all atomic nuclei are produced by the successive capture of neutrons, one mass unit at a time. They were the first ones to show that that the Universe had to go through a early hot dense phase in order to synthesize the elements.
Building on this work Alpher & Herman (1948) carried out improved calculations of primordial nucleosynthesis, with cosmic expansion taken into account. They figured out that the very high temperatures at early epochs meant that the Universe during that time was radiation dominated and that the matter and radiation were in thermal equilibrium. As the Universe expanded it cooled until electrons and protons recombined into neutral atoms. At this stage photon and matter field decoupled and were no longer in thermal equilibrium (recombination epoch). Now photons were free to propagate with the temperature of the Universe at recombination imprinted on it. They came to the conclusion that the cooled remnant of the hot early phase will be present in the Universe today and they estimated the temperature of this thermal background to be about 5 K. In 1965, the cosmic microwave background radiation (remnant of the hot

dense phase of the Universe) was discovered by accident by Arno Penzias and Robert Wilson (Penzias & Wilson, 1965). They found a constant, isotropic and unpolarized excess noise temperature of about 3.5 ± 1 K when they were commissioning an antenna for communications. Immediately afterwards, Roll & Wilkinson (1966) had measured a background temperature of 3.0 ± 0.5 K at the wavelength of 3.2 cm, confirming the black body nature of the spectrum.

This discovery and confirmation of the cosmic microwave background (CMB) radiation in 1964 secured the Big Bang as the best theory of the origin and evolution of the Universe. Correspondingly BBN theory, best explains the formation of light elements in the Universe and it matches the observed light element abundances only if $\Omega_b \sim 0.04$.

1.2.2 Dark Matter

In fact there is evidence that there is more than just baryonic matter in the Universe. In 1933 Fritz Zwicky applied the virial theorem to the Coma cluster and deduced that it has about $\sim$ 400 times the mass contained in the visible stars (Zwicky, 1933). He concluded that there must be a lot more *dark* or *hidden matter* compared to the visible matter in the clusters. Sinclair Smith came to the same conclusion in 1936 for the Virgo cluster (Smith, 1936). This idea of *hidden* or *dark matter* was largely ignored until the 1970's, when Vera Rubin (Rubin et al., 1980) observed flat rotation curves of galaxies to very large radii. A galaxy rotation curve shows the rotational velocity of matter as a function of it's distance from the center. If the stars in the galaxies follow Keplerian motion then the velocity of the stars can be given by

$$v = \sqrt{\frac{Gm(< R)}{R}} \tag{1.9}$$

where $m(< R)$ is the mass within radius R. At large distances enclosing most of the visible parts of the galaxy we expect the velocity to drop as the square root of the radius. Therefore flat rotation curves give an indication that there must be more matter present in a galaxy even after the visible matter ends. Initial estimates suggested that $\Omega_m \sim 0.2$, with the baryonic matter just a small fraction of the total matter density of the Universe.

1.2.3 Dark Energy

Recently there has been direct evidence for a new component in the Universe called dark energy (non-zero Ω_Λ), from observations of supernovae of a type Ia whose intrinsic luminosities are close to uniform (Riess et al. 1998; Perlmutter et al. 1999). The observed brightness as a function of the wavelength shift of the radiation probes the geometry of

spacetime. Their measurements agree with a cosmological model with $\Omega_k = 0$, meaning no space curvature, and $\Omega_\lambda \sim 0.7$.

Hence the Friedmann equations can be decomposed into its constituent parts and be written as

$$H^2 = \left(\frac{\dot{a}}{a}\right)^2 = H_0^2 \left(\frac{\Omega_r}{a^4} + \frac{\Omega_m}{a^3} + \frac{\Omega_k}{a^2} + \Omega_\Lambda\right) \tag{1.10}$$

The various components that contribute to the energy density of the Universe given by Ω_r the radiation density, Ω_m the matter density (baryonic+dark), Ω_k the curvature term and finally Ω_Λ the energy density contribution from the cosmological constant. The exact values of the various density parameters is measured today from CMB anisotropies, which we discuss in detail in the next section.

1.3 ΛCDM model and growth of large scale structure in the Universe

In the previous section we have described the component parts that make up the Universe. Along with the Friedmann equations of motion it fully describes the cosmological evolution of the Universe. This cosmological model provides the initial conditions and the evolutionary framework for cosmological structure formation. The current cosmological model which best describes the Universe is called Λ Cold Dark Matter (ΛCDM) model and it integrates nicely the cosmological theories, models of gravitational structure formation, CMB anisotropies, dark matter, dark energy, flat geometry and galaxy properties.

The Universe we live in today is homogeneous, but only when averaged over very large scales. On small scales, the Universe we see is highly inhomogeneous. Our Universe is full of complex structure, created by gravitational instability acting on tiny seed perturbations in the early universe. These seed perturbations are thought to have been produced during the inflationary epoch of the Universe. Inflation has the effect of smoothing out inhomogeneities, anisotropies and the curvature of space, thereby pushing the Universe to a very simple state, in which it is completely dominated by the inflaton field and the only significant inhomogeneities are the tiny quantum fluctuations in the inflaton. These fluctuations can be described by Gaussian random fields and have nearly the same power on all scales ($P(k) \propto Ak^n$ with $n \sim 1$). We can quantify these fluctuations by the δ_x parameter, which is defined as

$$\rho(\vec{x}, t) = \bar{\rho}(t)[1 + \delta_x(\vec{x}, t)] \tag{1.11}$$

At early epochs, $\delta_x << 1$ for perturbation of all scales. This also implies that the perturbation is in the linear regime. The description of the density fluctuation field is

statistical hence it is convenient to study perturbations in Fourier space. The Fourier expansion of δ_x is:

$$\delta_x(\vec{x},t) = \int \frac{d^3k}{(2\pi)^3}\delta_k(\vec{k},t)e^{i\vec{k}.\vec{x}} \tag{1.12}$$

The Fourier modes δ_k evolve independently while the perturbations are in the linear regime. Additionally for a Gaussian random field, any statistical quantity of interest can be specified in terms of the power spectrum $P(k)$ defined by

$$\left\langle \delta_k(\vec{k})\delta_k^*(\vec{k'}) \right\rangle = (2\pi)^3\delta_D(\vec{k}-\vec{k'})P(k) \tag{1.13}$$

where δ_D is the Dirac delta function.

We can then write down the time evolution of each individual Fourier mode δ_k by applying the Jeans equation, which in k space can be written as

$$\ddot{\delta_k} + 2H\dot{\delta_k} + \left[\frac{c_s^2k^2}{a^2} - 4\pi G\bar{\rho}\right]\delta_k = 0 \tag{1.14}$$

Since dark matter interacts only through gravity, the sound speed, $c_s = 0$, which means that the primordial density perturbations can grow even before recombination by attracting dark matter to the center of the potential wells. The density perturbations come into the particle horizon first at radiation dominated and then later matter dominated epochs. The growth rate of these fluctuations due to gravity is different at different epochs. This difference in the growth rates results in the modified power spectrum at later times (Dodelson, 2003). The slope of the power spectrum changes as the function of the scale length. This behavior can be quantified by using the transfer function, $T(k,z)$, which is defined by

$$P(k,z) = P(k)T^2(k,z) \tag{1.15}$$

where $P(k)$ is the power spectrum of the primordial density fluctuations and $P(k,z)$ is the transmitted power spectrum at redshift z.

For baryons, however, there is finite speed of sound in the photon-baryon plasma ($c_s \neq 0$) which exists in the Universe before recombination. Thus Eq. 1.14 suggests that the photon-baryon plasma will undergo oscillations as the gravity tries to compress the plasma while radiation pressure will try to push material outwards of the potential wells. The baryon power spectrum before decoupling is therefore associated with the acoustic oscillations of the photon-baryon plasma. The spatial inhomogeneity at the epoch of recombination is seen today as temperature anisotropy in the CMB radiation field due to the fact that the angular temperature fluctuation distribution is simply the projection of spatial temperature fluctuation. The amplitude and position of the peaks in the CMB power spectrum is very sensitive to the cosmological parameters. Thus the

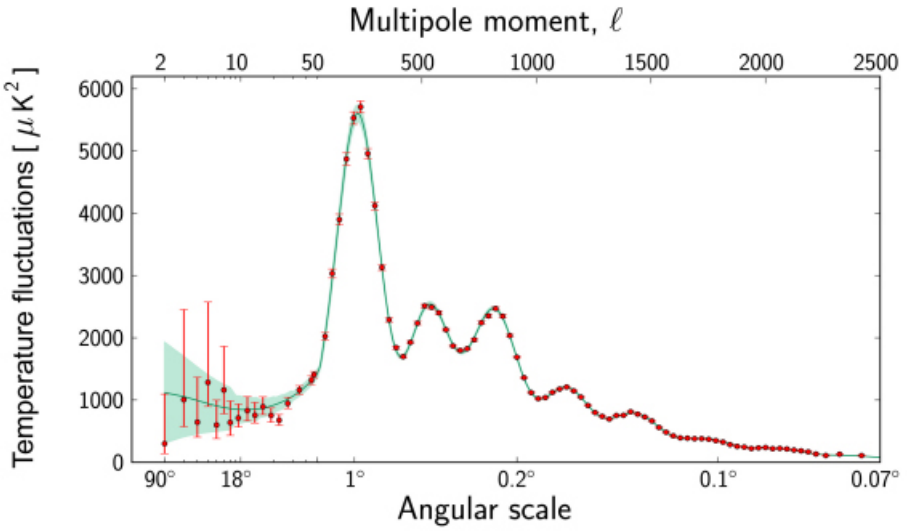

Figure 1.1 The Planck power spectrum. Credits: ESA and the Planck collaboration

CMB power spectrum (Fig. 1.1) can be used to extract the cosmological parameters with a large accuracy.

Sound waves stop oscillating at recombination when the baryons release the photons. Modes that reach extrema of their oscillation by recombination will carry enhanced temperature fluctuations. The spatial frequency of these temperature peaks are related to the fundamental distance scale of the sound horizon at recombination. Therefore the first peak of the CMB power spectrum represents the mode that compressed once inside potential wells before recombination, the second the mode that compressed and then rarefied, the third the mode that compressed then rarefied then compressed again and so on. The acoustic peak scale and its angular extent provides the angular diameter distance to recombination which in turn is very sensitive to the curvature and expansion history of the Universe

Baryons weigh down the photon-baryon plasma and add mass to the oscillating system. The odd numbered acoustic peaks are associated with compression and they are enhanced by an increase in the amount of baryons in the Universe. The even numbered peaks are associated with rarefaction and they are suppressed. Thus with the addition of baryons the odd peaks are enhanced over the even peaks.

The amplitude of the third peak is sensitive to the matter-radiation density ratio. Raising the dark matter density reduces the overall amplitude of the peaks. Lowering the dark matter density eliminates the baryon loading effect. This implies that a high third peak is an indication of dark matter. With three peaks, the dark matter contribution can be disentangled from the baryons. The matter to radiation ratio also controls the age of the Universe at recombination. This was the leading order ambiguity in the measurement of the spatial curvature of the Universe. That was resolved when the first least

three peaks were precisely measured and they point to the fact that $k = 0$, $\Omega_b = 0.049$ and $\Omega_m = 0.31$ (Planck Collaboration et al., 2013). This means that the physical density of the Universe is equal to the critical density defined by equation 1.6 which implies that $\Omega_{tot} = 1$. These observations also point to the fact that we live in a double dark Universe dominated by dark energy and dark matter with the observable matter in the Universe making up just a small fraction of the total energy density of the Universe. The peaks at the high l, act as a consistency check on the measurements made from the first three peaks. Hence we can see that the CMB power spectrum provides us with a simple but elegant and powerful method to measure the cosmological parameters. The accurate measurements of cosmological parameters from CMB confirms the ΛCDM model of the Universe.

1.3.1 Non-linear structure formation

The questions which arises next is how do the fluctuations in dark matter and baryons evolve after recombination? We see a large variety of structure in the current Universe in large galaxy redshift surveys. These redshift surveys such as the CfA redshift survey (Geller & Huchra, 1989), Two Degree Field Galaxy Redshift Survey (2dFGRS, Folkes et al. 1999) and Sloan Digital Sky Survey (SDSS, Ahn et al. 2014) showed that the galaxies are also not distributed randomly throughout the Universe. They are found to lie in clusters, filaments and void like structures which contain almost no galaxies.
As the fluctuations grow in amplitude, the evolution becomes too complex. One of the methods to model the growth of structures in a slightly non-linear regime was put forward by Zel'dovich (1970). The Zel'dovich approximation provides an intuitive way to understand the formation of the cosmic web. The basic assumption of the of this method is that a particle continues to move in the directions of it's initial displacement. In comoving co-ordinates the equation can be written down as

$$\vec{x}(t) = \vec{x}_i - c(t)\vec{f}(\vec{x}_i) \tag{1.16}$$

So what are the functions $c(t)$ and $\vec{f}(\vec{x}_i)$? We can write down the mass conservation before orbit crossing for any geometry as

$$\rho(\vec{x}, t)a^3 d^3\vec{x} = \rho_i(\vec{x_i})d^3\vec{x_i} \tag{1.17}$$

Using linear algebra we get

$$\rho(\vec{x}, t) = \rho_i(\vec{x_i})a^{-3}\left(\det\left(\frac{\mathrm{d}\,\overrightarrow{x}}{\mathrm{d}\,\overrightarrow{x_i}}\right)\right)^{-1} \tag{1.18}$$

but from Eq. 1.16

$$\left(\frac{d\vec{x}}{d\vec{x_i}}\right)_{jk} = \delta_{jk} - c(t)\frac{\partial f_j}{\partial x_k} \tag{1.19}$$

therefore we can rewrite Eq. 1.18 as

$$\rho(\vec{x},t) = \rho_i(\vec{x_i})a^{-3}\frac{1}{(1-c\lambda_1)(1-c\lambda_2)(1-c\lambda_3)} \tag{1.20}$$

or

$$1+\delta(\vec{x},t) = \frac{1}{(1-c\lambda_1)(1-c\lambda_2)(1-c\lambda_3)} \tag{1.21}$$

where $\lambda_1 > \lambda_2 > \lambda_3$ are the eigenvalues of the deformation tensor $\partial f/\partial x$. When $c(t) > 0$, i.e. the Universe is expanding, we can see that if $\lambda_i > 0$ this implies collapse in the direction of the i^{th} eigenvector. It is clear from this equation that collapse happens first along the axis associated with the first (largest) eigenvalue. Hence, collapse leads to flattened structures, called (Zel'dovich) pancakes. Therefore, this model automatically provides an explanation for the cosmic web structure of matter in the Universe.
In the linear regime ($\lambda_i << 1$) Eq. 1.21 can be reduced to

$$\delta(\vec{x},t) = 1 + c(\lambda_1+\lambda_2+\lambda_3) \tag{1.22}$$

Therefore in the linear regime $\delta(\vec{x},t) = c(t)Tr.(\vec{\nabla}\cdot\vec{f}) = c(t)(\vec{\nabla}\cdot\vec{f})$. Comparing this with the growth of perturbations in the linear regime $\delta(\vec{x},t) = D(t)\delta_i$, we get that $c(t) = D(t)$ and $(\vec{\nabla}\cdot\vec{f}) = \delta_i$ (where $D(t)$ is the linear growth factor). The poisson equation tells us that $\delta_i = \nabla^2\Phi_i/4\pi G\bar{\rho}_i$. Therefore we can write down the Zel'dovich equation (Eq. 1.16) as

$$\vec{x}(t) = \vec{x}_i - D(t)\frac{\vec{\nabla}\Phi_i}{4\pi G\bar{\rho}_i} \tag{1.23}$$

The Zel'dovich approximation makes no oversimplified assumptions about geometry and it remains accurate in the quasi-linear regime. It is accurate simply because it becomes exact in the limit of planar perturbations and this accuracy makes it one of the most important tools to generate initial conditions for N-body simulations. To generate the initial conditions, the particles are placed initially in a regular grid and the initial potentials are derived form the matter power spectrum just after recombination (taken from CMB data). The particles are then evolved according to Eq. 1.23, until the time of first shell crossing, which is around $z \sim 100$ (but depends on resolution of simulations). This picture of the Universe at $z \sim 100$ acts as the initial condition for numerical N-body codes, which evolve the positions of particles through time by a brute force calculation of gravitational force on the the particles (described in §1.5). These simulations are very accurate in the highly non-linear regime as there are no assumptions involved. Such simulations, like the Millennium simulation (Springel et al., 2005b) get the general large scale structure of the Universe right (see Fig. 1.2) .

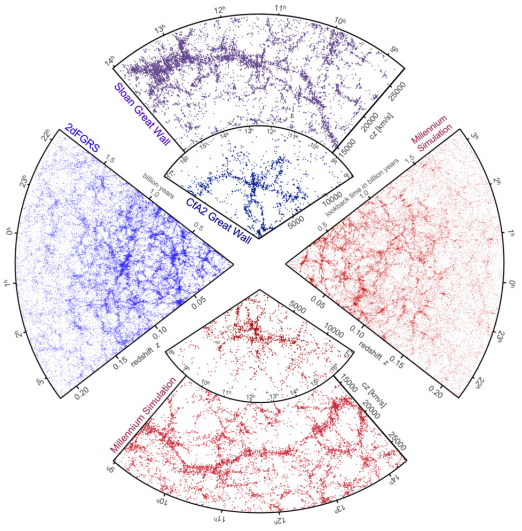

Figure 1.2 The large scale structure of the Universe : comparison between observations (CFA redshift survey, SDSS, adFGRS) and numerical simulations (Millennium simulation). Image credits: Springel et al. (2006)

The excellent match between observations which trace the visible baryonic matter and N-body simulations which predict the nature of dark matter structures implies that on large scales the baryonic matter follows the dark matter distribution because only gravity affects structure formation on large scales.

1.4 Galaxy formation and evolution

On scales smaller than $\sim$ 1 Mpc, it is much more difficult to explain and predict the nature of structures, because it requires the understanding of various baryonic processes like gas cooling, star formation, feedback and mergers, which occur during galaxy formation and evolution. The ΛCDM scenario provides the initial conditions and the evolutionary framework for modelling structure growth while the baryonic processes in addition to gravity dictate the evolution of visible matter on small scales.

1.4.1 Properties of observed galaxies

Observationally, galaxies show a wide range of morphologies and structures like discs, spiral arms, bars, bulges and massive spheroids. Hubble (1926) divided galaxies into three main categories ellipticals, spirals and dwarfs. The elliptical galaxies are spheroidal in shape. They mainly consist of old population of stars and hence have a higher flux in the red end of the spectrum. They lack cold gas and dust, which also implies that they are non-star forming. They have very little internal morphological structure and are mainly supported by the velocity dispersion of it's constituent stars. The surface

brightness is well described by a 'de Vaucouleur' profile (de Vaucouleurs, 1948). They are usually found in dense environments as it is thought that mergers between galaxies is the main formation mechanism for these giant ellipticals.
A second class of galaxies are called spirals. They exhibit a rotationally supported flattened disc with spiral arm structures in the disc and a central bulge. They have observable amounts of cold gas along with dust and a significant amount of star formation. They might also exhibit a bar like structure, which is usually formed due to gravitational instabilities either from secular factors or due to mergers. The discs have an exponential profile (Freeman, 1970), which is a direct consequence of the angular momentum conservation during radiative cooling of the halo gas.
A third type of galaxies are called dwarf galaxies and as their name suggest they are small stellar systems found in very low mass dark matter haloes ($< 10^{10}\mathrm{M}_{\odot}$). They usually contain young stars and do not have any particular morphological type. Their structure is highly disrupted by mergers and feedback. Essentially, galaxy formation research tries to model the formation and evolution of the various types of galaxies using the same physics.

1.4.2 Gas Accretion

Theoretically, the standard picture of galaxy formation was first put forward by White & Rees (1978). The basic idea is that the initial density fluctuations grow by gravity and form dark matter haloes which acquire angular momentum via tidal torques from neighbouring protohaloes. Then the bayonic matter (i.e. gas) falls into these dark matter potential wells. The fraction of the baryonic matter that is bound to dark matter haloes depends on the depth of the potential wells and the pressure of the gas. For example, when the Universe reionizes, the temperate and hence the pressure of the baryons increase, which results in a lower baryon fraction in low mass galaxies (Okamoto et al., 2008). When the gas does accrete the infalling gas experiences an accretion shock and is heated to the virial temperature of the halo (Binney, 1977).

1.4.3 Gas Cooling

The shock heated gas then cools through radiative processes. At typical densities of the astrophysical plasma two-body radiative processes are the most important such as free-free emission or bremsstrahlung, radiative recombination, collisional ionization and collisional excitation. However, the flux density of the incident radiation field can also have a large effect on the gas cooling rate (Kannan et al., 2014b). The photon - matter interactions can either reduce the cooling of the gas through photoionization (thereby reducing the amount of atoms available for collisional excitation) or increase the temperature of the gas through photoheating. If the net cooling rate is given by

$\Lambda(T, n_H, Z, U)$ (where T is the temperature of the gas, n_H is the density, Z is the metallicity and U is a parameter which quantifies the incident radiation field) then we can define a cooling time given by

$$t_{cool} = \frac{3nk_BT}{2\Lambda} \tag{1.24}$$

In order to understand the importance of cooling we need to compare the cooling time with the free fall time of the system $t_{ff} \propto 1/\sqrt{G\rho_{sys}}$.
By comparing these two different time scales we can establish different regimes of gas cooling in galaxies (Rees & Ostriker, 1977; White & Frenk, 1991)

- $t_{cool} > t_{ff}$: The system is in quasi-hydrostatic equilibrium. The gas contracts and cools, but very slowly and the system has time to adjust and get back to hydrostatic equilibrium
- $t_{cool} < t_{ff}$: Gas cooling is catastrophic. The cooling is so efficient that the system does not have enough time to establish hydrostatic equilibrium and all the gas cools down to the center and forms stars at a very high rate.

The latter case applies to haloes of masses smaller than approximately $\sim 10^{12}\mathrm{M}_{\odot}$, while the former applies to more massive haloes. The cooling flow from the quasistatic hot atmosphere is the process that basically limits the fuel for star formation in the center of galaxies (Silk, 1977; Kannan et al., 2014b). Therefore calculating the gas cooling rate accurately is very important.

1.4.4 Formation of galactic discs

The angular momentum of the gas in the halo arises in the same way as that of the dark matter halo, i.e., tidal torques from large scale structure. Since radiative cooling is an angular momentum conserving process the gas forms self-gravitating disc like structures after cooling.
The sizes of galactic discs was first calculated by Fall & Efstathiou (1980) and later refined by Mo et al. (1998) using the fact that the observed disc profiles were exponential and that the discs have to be thin and centrifugally balanced. They derived that the scale length R_d of a disc, which has an exponential surface density profile

$$\Sigma(R) = \Sigma_0 exp(-R/R_d) \tag{1.25}$$

is given by

$$R_d = \frac{1}{\sqrt{2}} \left(\frac{j_d}{m_d} \right) \lambda r_{200} \tag{1.26}$$

where j_d is the fraction of the halo angular momentum in the disc, m_d fraction of halo mass in the disc λ is the spin parameter of the halo and r_{200} is the radius at which the

mean density of the halo is 200 times the mean density of the Universe. This model was very successful in matching the observed sizes of discs.

1.4.5 Stability of galactic discs

Once the discs form, there is the question of how stable they really are? The criterion for the stability of thin discs was derived by Toomre (1964). This criterion is quantified by the Q parameter defined as:

$$Q = \frac{\kappa\sigma}{\pi G\Sigma} \tag{1.27}$$

where κ is the epicyclic frequency of the disc and Σ is the surface density. Qualitatively this equation describes the balance between the local gravitational force Σ which causes the disc to collapse and the rotational (κ) and pressure (σ) support which tries to make the disc stable. The disc is unstable if the gravitational force is larger than the rotational and pressure forces, i.e., $Q < 1$. If the disc become locally unstable then it collapses to form what are called Giant Molecular Clouds (GMCs). The clouds eventually themselves become unstable and fragment into stars. Star formation also occurs when the disc becomes globally unstable. Perturbations on the scale of the disc can no longer be studied by using the Toomre Criterion, as it applies only to local instabilities. A pioneering numerical study of the global stability of discs was performed by Ostriker & Peebles (1973), who showed that rapidly rotating self gravitating stellar systems with the properties of observed discs would be unstable to $m = 2$ modes but the addition of a spherical halo component stabilized the disc. They also concluded that in order for the disc to be stable the dark matter halo component inside of the disc must be comparable to the stellar disc. Therefore normalized, the halo mass in the spirals must be much larger than the stellar mass. This result lent further credence to the dark matter theory.

1.4.6 Star Formation

Gravitational instabilities of the cold gas clouds triggers cloud collapse and eventually the formation of stars. To a first approximation the star formation rate can be quantified by the following equation

$$\frac{d\rho_*}{dt} \propto \frac{\rho_{gas}}{t_{dyn}} \tag{1.28}$$

which says that the star formation rate (SFR) density is proportional to the local density of the gas (ρ_{gas}) and the local dynamical time (t_{dyn}). The dynamical time is the time taken by a gravitationally unstable cloud to collapse on itself and is given by

$$t_{dyn} \propto \frac{1}{\sqrt{G\rho_{gas}}} \tag{1.29}$$

Therefore

$$\frac{d\rho}{dt} \propto \rho_{gas}^{3/2} \tag{1.30}$$

This model is a three dimensional representation of the observed two dimensional Kennicutt-Schmidt relation (Schmidt 1959; Kennicutt 1998).

1.4.7 Feedback

It was realized very early that star formation in the dark matter haloes is very inefficient. This inefficiency was attributed to feedback from stars (Larson, 1974; White & Rees, 1978; Dekel & Silk, 1986) and active galactic nuclei (AGN) (Springel et al., 2005b; Di Matteo et al., 2005; Croton et al., 2006; Sijacki et al., 2007). Stars inject energy and momentum back into the gas in form of stellar winds, photoheating, radiation pressure and supernova (SNe) feedback. There are two kinds of SNe feedback mechanism currently considered, kinetic feedback and thermal feedback. Kinetic feedback models concentrate on imparting momentum to the surrounding gas and ejecting it out of the disc and maybe the halo itself, while thermal feedback models focus on heating the surrounding gas and relying on gas pressure to generate galactic scale outflows. Modelling these processes remains quite a challenge for modern galaxy formation theories. We will discuss various feedback mechanisms in more detail in Chapters 4 & 5.

1.4.8 Mergers

In addition to processes discussed above, due to the hierarchical nature of structure formation, galaxies accrete other galactic systems. The merging satellite galaxies lose energy through dynamical friction, falls to the center and merges with the central galaxy. Such merger events change the morphology of galaxies. For example, an elliptical galaxy is thought to be formed by a merger of two, approximately equal mass, spiral galaxies (see Chapter 3 for more details). In addition to changing the morphology, there might also be a spike in the star formation rate, as the merger induces torques which drives gas to the center and forms stars. After such a merger event, a disc can reform by accreting high angular momentum gas from it's halo.

1.5 Numerical simulations of galaxy formation

As described in §1.4, the theory of galaxy formation and evolution, requires modelling various complex physical phenomenon such as gravity, hydrodynamics, gas cooling, star formation physics, feedback from stars and AGN and to some extent the effect of astrophysical radiation fields. Today the most popular tool used to study galaxy formation

and evolution are numerical N-body+hydrodynamic simulations. This is because the direct simulation is often the only robust and accurate method for predicting the outcome of the highly non-linear and diverse physical processes which effect galaxy formation.

1.5.1 Gravity

N-body (gravity only) simulations are widely used to study large scale structure of the Universe. A wealth of information has been derived using N-body simulations, like the global properties of dark matter haloes, mass and angular momentum distribution (Barnes & Efstathiou, 1987), merger histories (Lacey & Cole, 1993), density profiles of dark matter (Navarro et al., 1997), properties of single galaxies such as the dynamics of merger between galaxies (Toomre & Toomre, 1972) and also the stability of galactic discs (Ostriker & Peebles, 1973).

There are many algorithms used to solve the gravitational interaction between a large number of particles. The simplest and the most direct method is called the Particle-Particle (PP) method (Gould & Tobochnik, 1988). Here the force on each particle 'i' is calculated by

$$\vec{F_i} = -\sum_{j \neq i} \frac{G m_i m_j}{r_{ij}^3} \vec{r}_{ij} \tag{1.31}$$

This method is very accurate and is useful in the regime where two-body interactions between particles cannot be ignored (eg. globular cluster dynamics). However the computational cost is $\mathcal{O}(N^2)$, and hence it is not suitable for calculating gravity for a large number of particles.

A faster and computationally efficient method for calculating gravity is the Particle-Mesh (PM) method (Bertschinger & Gelb, 1991) . It treats the force as a field quantity by approximating it on a mesh. The density is interpolated from particles to the mesh. Then the gravitational potential can be calculated by using the Poisson's equation

$$\nabla^2 \Phi = 4\pi G \rho \tag{1.32}$$

for the gravitational potential Φ, using an Fast Fourier Transform (FFT) technique. In the frequency domain the Poisson equation reduces to the simple form

$$\hat{\Phi} = -\frac{1}{k^2} 4\pi G \hat{\rho} \tag{1.33}$$

and the force $\hat{F}$ is just

$$\hat{F} = ik\hat{\Phi} \tag{1.34}$$

where k is the wavenumber and the hats denote the Fourier transforms. The main advantage of the PM methods is speed, with the computational cost of $\mathcal{O}(N \ \log N)$

operations. However as the algorithm is not adaptive, it does not automatically resolve high density regions where particles accumulate.

In order to resolve the problem of low resolution of nearby forces a Particle-Particle/Particle-Mesh algorithm was developed (Brandt & Lubrecht, 1990). This method consists of two parts, a PM part computes the long range slowly varying forces while the forces from nearby particles are calculated using a PP algorithm. Strong clustering of particles at later times makes the PP part of the algorithm very computationally expensive. To solve this problem, Couchman (1991), introduced "mesh-refined" P3M algorithm (AP3M). The algorithm adaptively refines grid sizes and shifts some of the burden of the PP computation to high-resolution FFTs.

An alternative to the PM methods are the hierarchical tree algorithms, which have an intrinsic adaptive force resolution (Appel, 1985; Barnes & Hut, 1986). This method involves arranging particles in a hierarchical tree structure by refining the computational domain into smaller and smaller regions. The Barnes & Hut (1986) algorithm involved refining each cell into two equal parts in each direction, called the oct-tree. There are of course other ways to construct a tree such as the k-D (binary) tree structure in which bisections are done recursively through their longest axis of the cells. Of the two hydrodynamic simulation codes that we use in the thesis GADGET-2 (Springel, 2005) uses the oct-tree, while GASOLINE (Wadsley et al., 2004), whose gravity algorithm is based on PKDGRAV (Stadel, 2001), uses the k-D tree structure. The tree structure partitions the mass distribution into a hierarchy of localized regions. The force from other particles in the region near the particle in question is calculated accurately, while the distant regions are explored more coarsely by treating distant clumps of particles as single massive pseudo-particles, centered on the center of mass of the corresponding region. A force computation proceeds by walking the tree and summing up force contributions from the tree nodes. A node of size l is opened only if the distance r from the particle to the center of mass of the node is less than r_{crit}

$$r_{crit} \sim \frac{l}{\theta} \tag{1.35}$$

where θ is the accuracy parameter also called the opening angle. If $r > r_{crit}$, then the gravity walk along that node is terminated otherwise it is opened, and the walk is continued to all its siblings. The opening angle θ decides the accuracy of the gravity calculation. For smaller values of θ the force is very accurate, in fact in the limit of θ approaching zero, the tree algorithm performs the PP calculation of the gravity force, which is computationally expensive. For optimal opening angles, the computational cost can be reduced considerably and is of $\mathcal{O}(N \log N)$. The tree codes are gridless, have no preferred geometry and are inherently adaptive. This makes the tree algorithm

particularly effective in simulating systems with wide dynamical range, like merging galaxies.

1.5.2 Hydrodynamics

The major advantage of hydrodynamical simulations over N-body simulations, is that they model the properties of the visible matter. They are a very powerful tool to understand the details of various baryonic processes that play an important role in galaxy formation. These simulations were used in studying a variety of baryonic processes like galactic disc formation (Katz & Gunn, 1991; Katz, 1992), the effects of galaxy mergers on it's morphology and star formation rate (Mihos & Hernquist, 1996; Cox et al., 2006a), etc. These simulations were the first to identify the angular momentum problem in galaxies. In analytic galaxy formation models like Fall & Efstathiou (1980); Mo et al. (1998), it is assumed that the angular momentum of the gas that cools is conserved and this simple assumption easily reproduces the sizes of present day galactic discs (see §1.4). However, these models built up unnaturally large bulges (van den Bosch et al., 2002). The first generation cosmological hydrodynamical simulations also revealed that the simulated discs were too concentrated in the center (Navarro & Benz, 1991; Navarro et al., 1995; Navarro & Steinmetz, 1997). This was because the low angular momentum gas in the halo immediately cooled to the center and formed stars. It was later realized that feedback processes from stars (and later Active Galactic Nuclei), were needed in order to blow away low angular momentum material from the halo of the galaxy. Modern simulations with strong stellar feedback mechanisms reproduce the observed sizes and flat rotation curves of disc galaxies (Robertson et al., 2004; Okamoto et al., 2005; Governato et al., 2010; Stinson et al., 2013a; Kannan et al., 2014b; Marinacci et al., 2014). This implies that we must somehow model star formation and feedback physics in the hydrodynamics simulations and since these processes take place below the resolution limit of current simulations, sub-grid empirical models become necessary, which will be discussed in more details Chapters 4 & 5. Here we will briefly describe the fundamentals of hydrodynamics and its implementation.

There are three main algorithms employed to simulate hydrodynamics in galaxy formation codes: Eulerian grid-based hydrodynamics (Stone & Norman, 1992; Cen, 1992; Teyssier, 2002), Lagrangian smoothed particle hydrodynamics (SPH) (Lucy, 1977; Gingold & Monaghan, 1977; Monaghan, 1992; Wadsley et al., 2004; Springel, 2005) and moving mesh hydrodynamics (Springel, 2010a; Duffell & MacFadyen, 2011). The Eulerian methods discretize space and solves the equations of motion in the reference frame of a static observer. While Lagrangian smooth particle hydrodynamics codes discretize mass and solve equations of motion in the reference of each moving fluid element. The moving mesh codes discretize space but the grid is not static, it moves along with the

flow of the fluid element. In this thesis we use SPH to study galaxy formation and we will briefly describe the technique below.[1]

The basic equations which govern hydrodynamics are the conservation of mass, momentum and energy (also called Navier Stokes equations). They can be derived from the moments of the collisional Boltzmann equation

$$\frac{\partial f}{\partial t} + \sum_i \dot{x}_i \frac{\partial f}{\partial x_i} + \sum_i \dot{v}_i \frac{\partial f}{\partial v_i} = \frac{\partial f}{\partial t}|_c \tag{1.36}$$

where $f(\vec{x}, \vec{v}, t)$ is the distribution function defined such that $f(\vec{x}, \vec{v}, t) d^3x d^3v$ = probability of finding a particle in phase space volume $d^3x d^3v$ centered on $\vec{x}, \vec{v}$ at time t. Therefore

$$\int\int f(\vec{x}, \vec{v}, t) d^3x d^3v = N \text{ (Total number of particles in the system)} \tag{1.37}$$

Multiplying Eq. 1.36 with mass of the particle m and integrating over d^3v we get the mass conservation equation

$$\frac{D\rho}{Dt} = \frac{\partial \rho}{\partial t} + \vec{u} \cdot \vec{\nabla} \rho = -\rho \vec{\nabla} \cdot \vec{u} \tag{1.38}$$

where $\vec{u} = \langle \vec{v} \rangle$ is the mean fluid velocity at $(\vec{x}, t)$ ρ is the density and $D/Dt = \partial/\partial t + \vec{u} \cdot \vec{\nabla}$ is the Lagrangian derivative.

Multiplying Eq. 1.36 $m\vec{v}$ and integrating over d^3v we get the momentum conservation equation

$$\frac{D\vec{u}}{Dt} = \frac{\partial \vec{u}}{\partial t} + \vec{u} \cdot \vec{\nabla} \vec{u} = -\frac{\vec{\nabla} P}{\rho} + \frac{\vec{\nabla} \cdot \overleftrightarrow{\pi}}{\rho} \tag{1.39}$$

P is the pressure and $\overleftrightarrow{\pi}$ is the viscous stress tensor.

Finally multiplying Eq. 1.36 with mv^2 and integrating over d^3v we get the energy conservation equation

$$\frac{D\epsilon}{Dt} = \frac{\partial \epsilon}{\partial t} + \vec{u} \cdot \vec{\nabla} \epsilon = -\frac{P}{\rho} \vec{\nabla} \cdot \vec{u} - \frac{1}{\rho} \vec{\nabla} \cdot \vec{F} + \frac{1}{\rho} \Psi \tag{1.40}$$

where ϵ is the specific internal energy (internal energy per unit mass), $\vec{F}$ is the conduction heat flux and Ψ is the viscous dissipation rate. Along with the equation of state $\epsilon = 1/(\gamma - 1)\frac{P}{\rho}$, these equation completely describe the dynamics of a perfect ideal gas. In many astrophysical applications diffusive effects are assumed to be much smaller than dynamical effects and hence generally $\overleftrightarrow{\pi} = 0$, $\vec{F} = 0$ and $\Psi = 0$. In this limit the gas is said to be inviscid and non-conducting.

[1] In the thesis we use two SPH codes GADGET-2 and GASOLINE . They use slightly different versions of SPH. Here we describe in detail the GASOLINE implementation and briefly discuss the differences between the two codes.

1.5.3 Smoothed Particle Hydrodynamics

At the heart of SPH is the concept of discretization of the fluid into mass elements. Any hydrodynamic quantity is estimated using kernel interpolations. For any quantity $F(\vec{r})$, the interpolated version is given by

$$F_s(\vec{r}) = \int F(\vec{r}) w(|\vec{r} - \vec{r'}|, h) d\vec{r'} \tag{1.41}$$

where $w(\vec{r}, h)$ is the smoothing kernel and h is the characteristic width of the element. Most modern SPH implementations use the cubic spline kernel adopted from Hernquist & Katz (1989), which in three dimensions is defined as

$$w\left(q = \frac{|r|}{2h}\right) = \frac{8}{\pi} \begin{cases} 1 - 6q^2 + 6q^3 & 0 \leq q \leq 1/2 \\ 2(1-q)^3 & 1/2 < q \leq 1 \\ 0 & q > 1 \end{cases} \tag{1.42}$$

Recently there have been other kernels used in an effort to make the SPH implementation more accurate (Read & Hayfield, 2012).

The discretization of the field in mass implies that the field is known for a set of points $F_i = F(\vec{r_i})$, with an associated mass of m_i and density ρ_i. Provided that the points are sufficiently well sampled the integral in Eq. 1.41 can be approximated as

$$F_i = \sum_{j=i}^{N} \frac{m_j}{\rho_j} w(|\vec{r_i} - \vec{r_j}|, h) \tag{1.43}$$

This interpolation is accurate to second order in 1D, and the requirement that $h \geq d$ (d is the mean particle distance) implies that the minimum number of neighbours should be $N \approx 33$ in three dimensions (Springel, 2010b). However for momentum and energy conservation, a symmetric kernel, $W_{ij} = W_{ji}$, is required, therefore a kernel-average of the form

$$W_{ij} = \frac{1}{2} \left[w(|\vec{r_i} - \vec{r_j}|, h_i) + w(|\vec{r_i} - \vec{r_j}|, h_j) \right] \tag{1.44}$$

is used. Then the density can be calculated by the sum over the particles

$$\rho_i = \sum_{j=1}^{N} m_j W_{ij} \tag{1.45}$$

One can then easily show that the discretized form of the equation of motion or the momentum conservation equation (without diffusive and self-gravity terms) can be written as

$$\frac{D\vec{u_i}}{Dt} = -\sum_{j=1}^{N} m_j \left(\frac{P_i}{\rho_i^2} + \frac{P_j}{\rho_j^2} \right) \vec{\nabla} W_{ij} \tag{1.46}$$

and the heat equation takes the form of

$$\frac{D\epsilon_i}{Dt} = \frac{P_i}{\rho_i^2}\sum_{j=1}^{N} m_j \vec{u}_{ij} \cdot \vec{\nabla}_i W_{ij} \tag{1.47}$$

where $\vec{u}_{ij} = \vec{u_i} - \vec{u_j}$.

Another formulation of the SPH equations (used in GADGET-2) is given by Springel & Hernquist (2002), who present an entropy conserving scheme, where the energy is calculated using the equation of state (Eq. 1.48) instead of Eq. 1.47

$$\epsilon_i = A_i \frac{\rho^{\gamma-1}}{\gamma - 1} \tag{1.48}$$

where A_i is the entropy of the particle.

Even when starting with smooth initial conditions, gas dynamics may readily produce discontinuities in the form of shocks and contact discontinuities. Under these conditions the gas dynamics can no longer be described by an inviscid fluid. Thus the SPH equations must be modified, so that the gas dynamics mimics dissipation in shocks. This is accomplished in SPH using the artificial viscosity, which then adds an additional term to the momentum equation

$$\frac{D\vec{u_i}}{Dt}|_{visc} = -\sum_{j=1}^{N} m_j \pi_{ij} \vec{\nabla}_i W_{ij} \tag{1.49}$$

The change in internal energy due to viscous heating is given by

$$\frac{D\epsilon_i}{Dt}|_{visc} = \frac{1}{2}\sum_{j=1}^{N} m_j \pi_{ij} \vec{u}_{ij} \cdot \vec{\nabla}_i W_{ij} \tag{1.50}$$

and the change in the entropy is given by

$$\frac{DA_i}{Dt}|_{visc} = \frac{1}{2}\frac{\gamma - 1}{\rho_i^{\gamma-1}}\sum_{j=1}^{N} m_j \pi_{ij} \vec{u}_{ij} \cdot \vec{\nabla}_i W_{ij} \tag{1.51}$$

The most commonly used form of artificial viscosity is

$$\pi_{ij} = \begin{cases} \frac{-\alpha \frac{1}{2}(c_i + c_j)\mu_{ij} + \beta\mu_{ij}^2}{\frac{1}{2}(\rho_i + \rho_j)} & \vec{u}_{ij}.\vec{r}_{ij} < 0 \\ 0 & otherwise \end{cases} \tag{1.52}$$

with

$$\mu_{ij} = \frac{h_{ij}\vec{u_{ij}} \cdot \vec{r_{ij}}}{|\vec{r_{ij}}|^2 + \eta h_{ij}^2} \tag{1.53}$$

where $\alpha = 1$, $\beta = 2$ and $\eta = 0.01$ and c is the sound speed.

This formulation of SPH is very powerful and well suited for modeling gas dynamics. We use two SPH codes, GADGET-2 (Springel, 2005) in Chapters 2 & 3 and GASOLINE (Wadsley et al., 2004) in Chapters 4 & 5 of the Thesis. Till now we have described how the codes compute the gravitational and hydrodynamic forces, however as discussed in §1.4, there are other important baryonic processes that effect galaxies like gas cooling star formation and feedback. The resolution of current simulations if not enough to resolve these processes in detail and hence some kind of sub-grid models are used to mimic the effects of these processes in galaxy formation. These sub-grid models are different for different codes and hence we briefly describe the models in the relevant Chapters of the Thesis.

1.6 Structure of the Thesis

In this thesis we investigate many outstanding problems of galaxy formation and evolution using hydrodynamic simulations. The thesis is structured as follows: In Chapter 2 we investigate the effects of the most minor of merger events (merger ratio 1:1000), namely, the interaction between dark matter sub-haloes and the gaseous disc of the galaxy . We entertain the idea that these interactions can produce holes and shells in the HI discs of observed nearby galaxies. We first introduce the observational evidence for the HI holes and shells and discuss some mechanisms that are thought be behind the formation of these holes. We then introduce the idea that dark matter sub-haloes interacting with the disc of the primary galaxy can be a formation mechanism for the more massive of the observed holes. We then explain the numerical setup for the study and then apply them to investigate the effect of single dark-matter sub-halo interaction with the disc, as a function of dark matter sub-halo mass, impact velocity and gas content. The study is extended to a cosmological setup, where multiple dark matter sub-haloes are allowed to interact with the disc, with the orbits taken from a full cosmological simulation.

In Chapter 3 we investigate the effect of high merger ratio events from $1:50$ to $1:1$. These merger events are thought to change the morphology of interacting galaxies. We use the method introduced by Moster et al. (2014), which derives the initial conditions of galaxy mergers such as the properties of merging galaxies and their relative orbits, from Semi-Analytic Models (SAMs) and then use hydrodynamical codes to simulate the actual merger event. We simulate a wide range of merger events using this method and look at the mass transfer channels during a merger, like the amount of satellite mass given to bulge, amount of disc mass transferred to the bulge, amount of disc mass transferred to the stellar halo and the amount of gas mass transferred to the bulge. These mass transfer channels are quantified as a function of merger parameters, which in turn can be used as a input recipe for SAM's. We also investigate the impact of the

hot halo on the mass transfer channels and also look the sites of star bursts (bulge or disc) during mergers.

In Chapter 4 we shift the focus from morphology to the impact of feedback on the statistical properties of galaxies. We simulate a representative volume of Universe with a new feedback model, described in Stinson et al. (2013b), which includes short range photoheating from massive stars (mimicking creation of Strömgren spheres) in addition to the classical supernova feedback. The statistical properties of the simulated galaxies such as the stellar-halo mass relation, the galaxy stellar mass function, the star formation history of the Universe etc., are compared to the observed relations. First we discuss these results for high redshift galaxies and then limited results at $z = 0$ are shown along with the convergence tests of the code that we use.

In Chapter 5 we introduce a novel method which accounts for the local radiation flux while calculating gas cooling in hydrodynamic simulations of galaxy formation (Local Photoionization Feedback; LPF). The model uses simple assumptions for absorption of ultra-violet (UV) photons and an optically thin approximation to propagate local radiation field throughout the entire simulation volume. The Chapter starts with a discussion on some of the drawbacks of the stellar feedback model used in Chapter 4 and the need for calculating gas cooling accurately in simulations. Then, the importance of local radiation field on gas cooling is emphasized. We then list the basic principles of radiative gas cooling and justify the decomposition of the total cooling rate into primordial and metal cooling components. Then the spectrum and flux of local radiation sources in galaxies, such as radiation form massive stars, X-rays from shock heated gas and radiation form old population of stars, are discussed in detail along with the effect these sources have on the cooling curve of the gas. We then proceed to the detailed description of the numerical implementation of this method in the hydrodynamical code Gasoline and some test case gas cooling calculations with this new implementation are shown. Finally we test the effect of this new cooling calculation in a cosmological simulation of a Milky-Way type galaxy. Two simulations of the same galaxy with and without the new cooling calculation is performed and compared.

Finally in Chapter 6 we summarize the methods and results that were used in the thesis to study galaxy formation and evolution. We also give an insight into the importance of the LPF and how local radiation fields can be used to solve many outstanding problems in galaxy formation theory such as the formation of massive red and dead galaxies, observational signatures of LPF, mainly from metal abundance measurements in galactic haloes etc. Finally we list some of the improvements we would like to make to the LPF model.

Chapter 2

HI holes and shells

Mergers are an ubiquitous part of hierarchical structure formation. Major mergers are thought to completely change the morphology of interacting galaxies, while minor mergers induce local instabilities and minor star bursts. In this Chapter we look at the most minor of merger events (merger ratio 1:1000), specifically we test the idea that low mass dark matter sub-halo interaction with the disc of the primary galaxy might give rise to holes and shells, observed in the neutral hydrogen (HI) distribution of many nearby galaxies like M31 (Brinks 1981, Brinks & Bajaja 1986), M33 (Deul & den Hartog, 1990), Holmberg II (Puche et al., 1992), M101 and NGC 6946 (Kamphuis, 1993), IC 10 (Wilcots & Miller, 1998), SMC (Staveley-Smith et al., 1997) , LMC (Kim et al., 1998) and IC 2574 (Walter & Brinks, 1999).

These hole and shell like structures are typically regions of low HI density distributed across the entire galaxy, and come in various sizes ranging from a few 100 pc to about 1.5 kpc. Their expansion velocity sets an upper limit to their dynamical age (typically about about 10 - 60 Myr, cf. Walter & Brinks 1999 for IC 2574). The formation of HI holes and shells has often been ascribed to the action of stellar winds and supernova explosions occurring in OB associations and young stellar clusters (cf. Weaver et al. 1977; Tenorio-Tagle & Bodenheimer 1988; van der Hulst 1996). Based on a simple model of holes created by O and B stars, Oey & Clarke (1997) successfully predicted the observed number distribution of holes in the SMC, lending support to this hypothesis. More recently, the analysis conducted by Ott et al. (2001), Simpson et al. (2005), Weisz et al. (2009a) and Cannon et al. (2011) have shown that the stellar content of HI holes in Holmberg I and II, DDO 88 and 165 can release enough mechanical energy to drive the formation of holes on timescales similar to what is observed. In particular, Weisz et al. (2009a) were able to show that all the holes in Holmberg II observed with HST contain multiple stellar populations of different age. Warren et al. (2011) studied the

The work presented in this Chapter has been published in Kannan et al. (2012).

HI holes in five dwarf galaxies (DDO 181, Holmberg I, M81 Dwarf A, Sextans A and UGC 8508), and failed to detect a young star cluster at the center of the observed HI holes. They thus suggested that large holes may form due to multiple episodes of star formation.

There is more observational evidence against a single burst of star formation being responsible for the creation of HI holes. For example, no robust spatial correlation was found by Kim et al. (1999) between the distribution of the Hα emission and the HI holes in the LMC. Hatzidimitriou et al. (2005) estimated that the holes in the SMC not associated with a young star cluster are a factor of 1.5 more than those exhibiting relatively young stars at their center. In the Galaxy, the distribution of radio pulsars compared to that of holes seem to indicate that holes can not be produced by the supernova explosions of a single age stellar population (Perna & Gaensler, 2004). Pasquali et al. (2008) found that the most recent episode of star formation has taken place preferentially at the rims of the HI holes in IC 2574, exception made for the supergiant shell which indeed embeds a young star cluster (cf. Stewart & Walter 2000; Weisz et al. 2009b). Rhode et al. (1999) observed the HI holes in Holmberg II in search of the descendants (stars of spectral types B, A and F) of those clusters whose supernovae would have produced the holes. They measured an integrated light of the stars within the holes inconsistent with the hypothesis of a young star cluster triggering the formation of a HI hole. In the case of IC 1613, its largest HI shell was found to host about 27 OB associations whose energy can not sustain the formation and expansion of the shell (Borissova et al. 2004; Silich et al. 2006).

Some authors have proposed alternative formation hypotheses to the SNe origin. Efremov et al. (1998) and Loeb & Perna (1998) postulate that a high-energy gamma ray burst (GRB) from the death of a single massive star could create kpc sized holes in the Inter Stellar Medium (ISM), thus offering an explanation for holes without a detectable underlying cluster. These authors assume the energy from GRBs is emitted isotropically. However, GRBs release most of their energy in bi-directional beams (eg., Blandford & Znajek 1977 mechanism), making this scenario less likely to produce large HI holes.

Another mechanism proposed is the infall of gas clouds (Tenorio-Tagle et al., 1987). One observational prediction of this model is a half-circle arc seen in an HI position-velocity diagram. The half-circle arc arises from the gas being pushed to one direction, corresponding to the direction of travel of the high velocity clouds. Some observational support for this idea is reported by Heiles (Heiles 1979, 1984) who point out that the most energetic Galactic shells in their study all have half-circle arc signatures in position-velocity space (Kamphuis et al. 1991).

Here, we investigate an alternative formation scenario, where holes and shells in extended HI discs are the result of interaction of the gaseous disc with dark matter (DM) sub-haloes. The Lambda Cold Dark Matter (LCDM) model predicts the existence of

thousands of dark matter substructures within the dark matter halo of every galaxy (e.g. Springel et al. 2008 and reference therein). The majority of these sub-haloes is "dark" i.e. does not host a satellite galaxy or any visible stellar structures (e.g. Macciò et al. 2010; Font et al. 2011). If these sub-halo population is able to produce the observed holes in galactic HI discs, like the one of IC 2574, then this might provide a new way of detecting the presence of non-luminous DM haloes. For example, the number of holes could then be linked statistically to the amount of substructure in the dark matter distribution and thus provide a unique way to asses the nature of dark matter and by extension to test the ΛCDM model.

Perturbations on a stellar disc due to (massive) satellites have been extensively studied in the recent years (e.g. Kazantzidis et al. 2008; Moster et al. 2010a and references therein), while less attention has been given to the effect of low mass DM clumps on an extended gaseous disc, with few exceptions. Bekki & Chiba (2006) investigate how the impact of dark matter sub-haloes orbiting a gas-rich disc galaxy embedded in a massive dark matter halo influences the dynamical evolution of the outer HI gas disc of the galaxy. They show that the impact of dark matter sub-haloes ("dark impact") can be important for better understanding the origin of star formation discovered in the extreme outer regions of disc galaxies. They also discuss the possibility that this kind of dark impact will be able to produce holes in the gas distribution. In their study they adopted a model, which did not include multiple events, a live dark matter halo (they adopted an analytic fixed potential), cooling and star formation.

A new attempt to detect the imprint of the dark satellites in the HI disc of the Milky Way has been recently made. In a series of papers Chakrabarti & Blitz (2009, 2011) examine tidal interactions between perturbing dark sub-haloes and the gas disc of the Milky Way using high-resolution Smoothed Particle Hydrodynamics simulations. They compare their numerical results to the observed HI map of the Milky Way, and find that the Fourier amplitudes of the planar disturbances are best fitted by a perturbing dark sub-halo with a mass that is one-hundredth of the Milky Way with a pericentric distance of 5 kpc. More recently (Chang & Chakrabarti 2011) develop a perturbative approach to study the excitation of disturbance in the extended atomic hydrogen discs of galaxies produced by passing dark matter sub-haloes. They show that the properties of dark matter sub-haloes can be inferred from the profile and amplitude of the different perturbed energy modes of the disc.

Motivated by these recent studies, we use high resolution hydro-dynamical simulations to study in detail the interaction of DM sub-haloes with a galactic gaseous disc. Our primary goal is to see under which conditions DM satellites are able to create holes that resemble the observed ones and whether the majority of these holes can be explained by dark satellites-disc interactions. We model our primary galaxy on the nearby dwarf galaxy IC 2574 and try to replicate its observed features in our simulations. After

having described our numerical setup, we will first present results of a single satellite-disc interaction, for different satellite orbital parameters and gas content. Then we will use satellite parameters (mass, velocity and position) directly obtained from high resolution N-body simulations to study the frequency of DM sub-halo disc encounters. Finally we will discuss the implications of our results.

2.1 Numerical Simulations

We make use of the parallel TreeSPH-code GADGET-2 (described in Chapter 1) in this work. Radiative cooling is implemented for a primordial mixture of hydrogen and helium following Katz et al. (1996) and a spatially uniform time-independent local ultraviolet background in the optically thin limit (Haardt & Madau, 1996) is included. The SPH properties of the gas particles are averaged over the standard GADGET-2 kernel using 64 SPH particles. Additionally, the minimum SPH smoothing length is required to be equal to the gravitational softening length in order to prevent artificial stabilization of small gas clumps at low resolution (Bate & Burkert, 1997).
All simulations have been performed with a high force accuracy of $\alpha_{force} = 0.005$ and a time integration accuracy of $\eta_{acc} = 0.02$ (for further details see Springel 2005). Star Formation (SF) and the associated heating by supernovae (SN) are modeled following the sub-resolution multiphase interstellar medium (ISM) model described in Springel & Hernquist (2003). The ISM in the model is treated as a two-phase medium with cold clouds embedded in a hot component at pressure equilibrium. Cold clouds form stars in dense ($\rho > \rho_{th}$) regions on a time-scale chosen to match observations (Kennicutt, 1998). The threshold density ρ_{th} is determined self-consistently by demanding that the equation of state (EOS) is continuous at the onset of SF. We do not include feedback from accreting black holes (AGN feedback) in our simulations as there is no evidence of AGN activity in dwarf galaxies like the one studied here. In our runs, the parameters for the star formation and feedback are adjusted to match the Kroupa initial mass function (IMF) as specified by Kroupa (2001). The SF time-scale is set to $t_*^0 = 3.5$ Gyr, the cloud evaporation parameter to $A_0 = 1250$ and the SN temperature to $T_{SN} = 1.25 \times 10^8 K$.

2.1.1 Primary Galaxy Setup

We apply the method given by Springel et al. (2005a) to construct the central galaxy. The central galaxy consists of an exponential stellar disc. In order to match the almost constant radial gas density profile of IC 2574, we have modeled the gas disc by two components. A radial exponential component and a constant radial profile which falls off rapidly at a specified scale radius. The stellar disc has a mass $M_{\rm disc}$, the gaseous disc has a mass $M_{\rm gas}$, with a spherical bulge with mass $M_{\rm b}$ embedded in a dark matter halo

of mass $M_{\rm vir}$. The halo has a Hernquist (1990) profile with a scale radius corresponding to a Navarro Frenk & White halo (NFW; Navarro et al. 1997) with a scale-length of $r_{\rm s}$ and a concentration parameter $c_{\rm vir} = R_{\rm vir}/r_{\rm s}$. We use the results of Macciò et al. (2008) to compute halo concentration as a function of virial mass. The scale-lengths r_d of the exponential gaseous and stellar discs are assumed to be equal, and are determined using the model of Macciò et al. (2008), assuming that the fractional angular momentum of the total disc $j_{\rm d} = (J_{\rm gas} + J_{\rm disc})/J_{\rm vir}$ is equal to the global disc mass fraction $m_{\rm d} = (M_{\rm gas} + M_{\rm disc})/M_{\rm vir}$ for a constant halo spin λ. This is equivalent to assuming that the specific angular momentum of the material that forms the disc is the same as that of the initial dark matter halo, and is conserved during the process of disc formation. The vertical structure of the stellar disc is described by a radially independent $sech^2$ profile with a scale-height z_0 , and the vertical velocity dispersion is set equal to the radial velocity dispersion. The vertical structure of the gaseous disc is computed self-consistently as a function of the surface density by requiring a balance of the galactic potential and the pressure given by the EOS. The stellar bulge is constructed using the Hernquist (1990) profile with a scale- length r_b .

We build a primary galaxy which matches the properties of IC 2574 (mass profiles taken from Leroy et al. 2008). The galaxy has a halo of mass $M_{200} = 10^{11} M_{\odot}$ obtained from the stellar mass, from the recipe given in Moster et al. (2010b), containing a stellar disc of mass $M_{\rm disc} = 3.16 \times 10^8 M_{\odot}$, a gaseous disc component of mass $M_{\rm gas} = 1.8 \times 10^9 M_{\odot}$ with 80 % of the gas in the HI disc, a small bulge of mass $M_{\rm bulge} = 3.16 \times 10^7 M_{\odot}$. The DM halo has a concentration parameter of $c_{200} = 8.47$. The scale radius of the disc (stellar & the exponential component of the gaseous disc) is $r_{\rm d} = 2.1$ kpc and the scale radius of the slab of gas is $r_{\rm slab} = 4.5$ kpc. Once we fix $r_{\rm d}$ we compute the halo spin parameter from the recipe of Mo et al. (1998) which results in a value of $\lambda = 0.047$. The disc scale-height is fixed at $z_0 = 0.15$ kpc and scale radius of the bulge is set at $r_{\rm b} = 0.095$ kpc. The galaxy has $N_{\rm DM} = 10^6$ DM particles, $N_{\rm disc} = 10^5$ in the stellar disc, $N_{\rm bulge} = 10^4$ in the bulge, and $N_{\rm gas} = 5.7 \times 10^5$ gaseous disc particles. The force resolution (softening) is 101,80,57 pc for dark matter, gas, and stars respectively In order to have a stable initial condition we evolve this primary galaxy in isolation for 1 Gyr. The initial conditions were chosen in such a way that the surface density of the gas match the observed density of IC 2574 after evolving for 1 Gyr as shown in Figure 2.1.

2.2 Simulation Results

We here present the results of our numerical experiments. We mainly run three kinds of simulations: single encounter with a pure DM sub-halo (no gas or stars); single encounter with a DM sub-halo containing a small gas fraction; and multiple, cosmologically

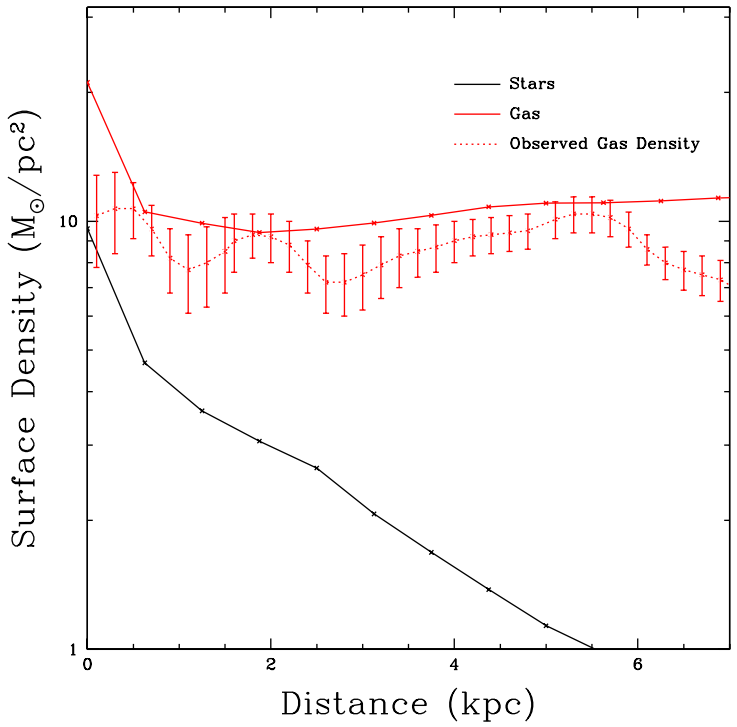

Figure 2.1 The red line is the gas surface density and the black line is the surface density of stars in the inner 7 kpc of IC 2574. The observational data is taken from Figure 27 of (Leroy et al., 2008). The error bars represent the rms uncertainty value.

motivated encounters.

These single halo simulations are simplistic experiments designed to explore the effect of sub-halo/disc interactions. Orbit, mass and gas content are not meant to represent the typical case. An cosmological motivated run with multiple interactions will be presented in §2.2.3.

2.2.1 Pure DM Sub-halo Interaction

In this section we investigate the dynamical impact of a pure DM halo on the gaseous disc. The mass of the sub-halo is first fixed at a value of $M_{\rm sb} = 10^8 M_\odot$. We want to have a highly concentrated sub-halo to act like a 'bullet' in the interaction. To do this we start with a $M_{200} = 10^{10} M_\odot$ halo and then carve out 99% of its mass and create a $10^8 \mathrm{M}_\odot$ halo. This is justified, as it has been shown that the sub-haloes passing through the primary halo of a galaxy get tidally stripped and can lose up to 90% and in some extreme cases 99% of their mass during their orbit (see Peñarrubia et al. 2008; Macciò et al. 2010). The total number of DM particles in the halo has been set to $N_{DM} = 1000$. Starting from a lower mass halo (e.g $10^9 \mathrm{M}_\odot$) would have resulted in a less concentrated 'bullet', hence our choice maximizes the dynamical effect on the disc. This sub-halo is

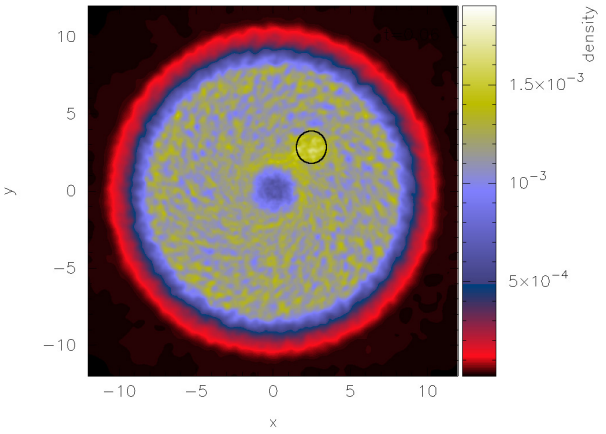

Figure 2.2 Surface density map of the gaseous disc after the passage of the pure DM sub-halo of mass $10^8 M_\odot$. Such an encounter leads to a gas overdensity (marked by a circle). The units of density in this plot are in $10^{10} M_\odot kpc^{-2}$. The 2D contour plots were made using the visualization software SPLASH (Price 2007).

placed at a distance of 5 kpc above the gaseous disc of the primary galaxy and given an initial velocity of $v_z = 150$ kms^{-1} perpendicular and pointing towards the galactic disc. Figure 2.2 shows a surface density map of the gaseous disc after the passage of the sub-halo.

As it emerges clearly from Figure 2.2, a pure DM sub-halo is unable to form a hole, instead it gives rise to a localized high density region (marked by a circle). This is due to the fact that the DM particles are collisionless. Due to the lack of contact forces the sub-halo cannot push away the gas particles. DM can only gravitationally focus the gas in a stream behind its path of motion (Bondi-Hoyle accretion;Edgar 2004;Bondi & Hoyle 1944; Bondi 1952) which gives rise to higher surface density in the region it passes through. These high density peaks are $20\% - 25\%$ denser than the mean density of the disc, and they last for about $80 - 90$ Myr, after which they are destroyed by the dispersion of the gas and the differential rotation of the disc. The fundamental result of this first experiment is that a pure dark matter sub-halo is not able to create a hole in the gaseous disc.

2.2.2 Gaseous Sub-Halo Interaction

Since a pure DM halo is not able to displace the gas in the disc, a medium which interacts through gravity as well as contact forces is needed in order to push the gas away from its motion path. A gaseous medium will provide the required contact forces to push the gas away and form holes. We construct the DM sub-halo with the same mass and concentration parameter as described in the previous section and in addition we also add a hot gaseous component. The hot gas has a beta profile with $\beta = 2/3$, a spin factor of $\alpha = 4$ and a core radius of 90 pc (see Moster et al. 2011 and §3.1.3 for more details

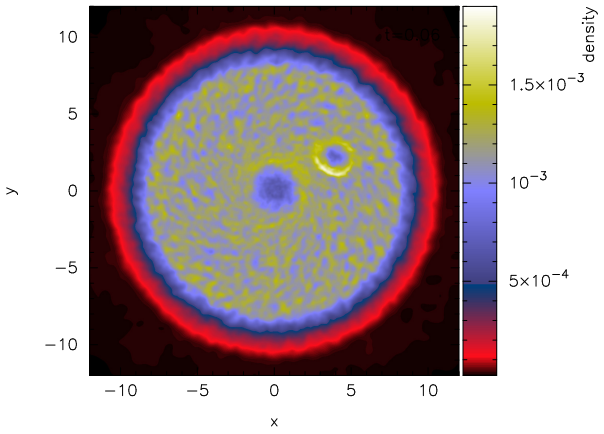

Figure 2.3 Effect of the interaction between a DM sub-halo containing 3.2% of gas by mass(DM mass = $10^8 M_\odot$).

about the numerical implementation of the hot gas component). These sub-haloes are expected to have a very low amount of gas (if any), due to re-ionization (e.g. Okamoto et al. 2008). [1]

Moreover we are interested in "dark" satellites, so we do not want the gas in the sub-haloes to form stars, hence we choose a very low gas fraction (i.e. fraction of mass in gas relative to the DM mass) in these sub-haloes: $M_{gas}/M_{DM} \approx 0.03$. We consider only an hot gas component; as haloes containing cold gas (and possibly stars), will be directly detectable; while, in this work, we are interested in testing the effects of the more numerous, undetected, dark satellite population, which is predicted by the cold dark matter model. We then place this new sub-halo on the exact same orbit of the pure dark matter experiment and let it interact with the gaseous disc as described in the previous section.

The hot gas in the halo is able to displace the gas in the disc and produce a low density region (a hole), associated with an expanding high density shock wave as shown in Figure 2.3. For our chosen parameters the hole has a diameter of about 1.5 kpc and lasts for about 60 Myr. The lifetime of the holes is decided by two factors, the pressure gradient and the differential rotation. Our simulations suggest that the pressure gradient causes the hole to be filled by gas long before it gets destroyed by the differential rotation, although differential rotation becomes important for very large holes. For typical hole sizes of $1-2$ kpc we find an average hole lifetime of about 50-60 Myr; in agreement with the dynamical ages estimated by Walter & Brinks (1999).

Another interesting feature of this simulation is the enhanced star formation on the rim of the hole, as shown in Figure 2.4. New stars have preferentially formed on the high density edges of the hole, while the hole itself contains very few new stars. This result

[1] Actually since we started from a 10^{10}M$_\odot$ halo, our halo could possibly contain some stars, but in this experiment we decided to neglect this component, since it won't change the overall picture.

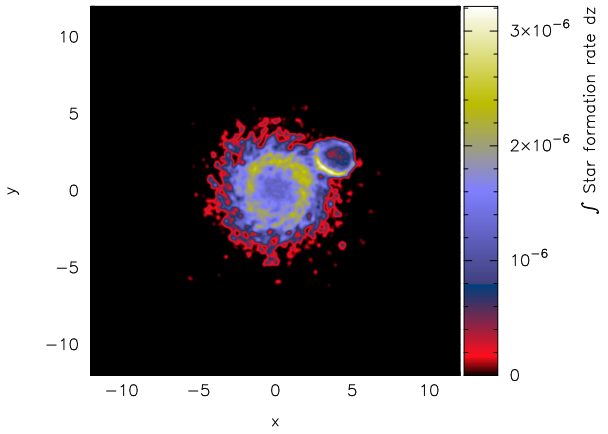

Figure 2.4 Star formation rate, showing clearly the ring of new stars formed along the rim of the hole. The units of SFR surface density in this plot are in $10^{10} M_{\odot} kpc^{-2}$.

is in agreement with the ages of the stars associated with the HI holes in IC 2574 as derived by Pasquali et al. (2008), via comparison of observed UBV colors with those predicted by synthetic stellar populations (for more details see Pasquali et al. 2008).

We then run a series of simulations for different percentages of gas fraction of the DM sub-haloes, keeping all other simulation parameters constant. The effect of a pure DM sub-halo and a sub-halo containing gas are inherently different. Figure 2.5 shows the relative surface density profiles of the gas along a strip of width 1 kpc joining the center of the galaxy and the center of the hole, for different sub-halo gas fractions (including the case of no gas). A pure DM sub-halo (in blue) produces a peak of increased density while a gaseous halo produces a low density region surrounded by high density wave. This density wave increases the density in the rim of the hole above the star formation density threshold ($\rho_{\rm th}$), thus triggering star formation all along the rim of the hole. As expected, the size of the hole and the extent to which the disc is perturbed depends on the gas fraction of the infalling DM sub-halo.

The impact with a sub-halo will create a net velocity gradient along the sub-halo trajectory in the vertical component of the HI gas. This signature could in principle disentangle different formation scenarios for the HI holes. Figure 2.6 shows the velocity in the z-component (perpendicular to the disc plane - $V_{z,disc}$ which equals zero in the unperturbed case) along the same strip as mentioned above. Here the infalling haloes has two different gas fractions, 3.2% (green line) & 0.8% (red line) with a velocity of v_z = 150 km s^{-1} and a halo with a gas fraction of 0.8% with a veloocity of v_z = 300 km s^{-1}. A higher sub-halo initial velocity and/or a larger gas fraction imparts more energy to the disc in the impact direction and hence produces a stronger signature in $v_{z,disc}$. This plot shows that the effect is small and would be very hard to detect in real observations as the effect is of the same order as the typical velocity resolution of HI observations of nearby galaxies (e.g. Walter et al. 2008)

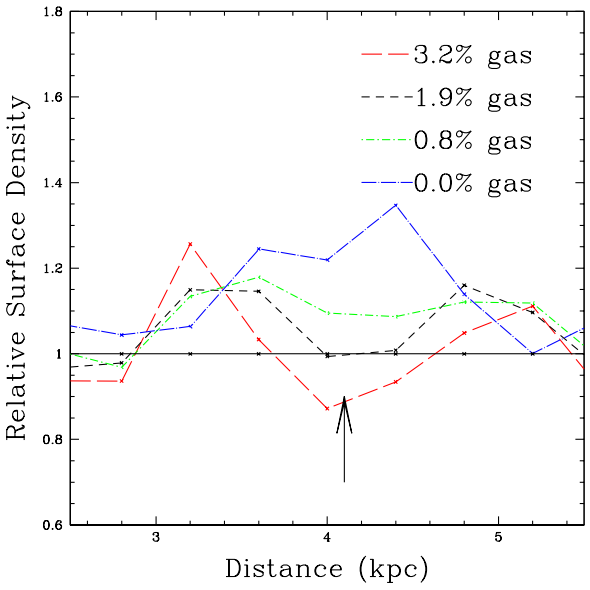

Figure 2.5 The effect of the interaction between DM sub-haloes with different gas fractions and the disc The curves denotes the relative surface density variation with respect to the isolated disc, upon the interaction with a halo with 3.2 % gas (red), 1.9% gas (black), 0.8% gas (green) and 0% gas (blue). The arrow indicates to point of impact of the haloes. (DM mass = $10^8 M_\odot$)

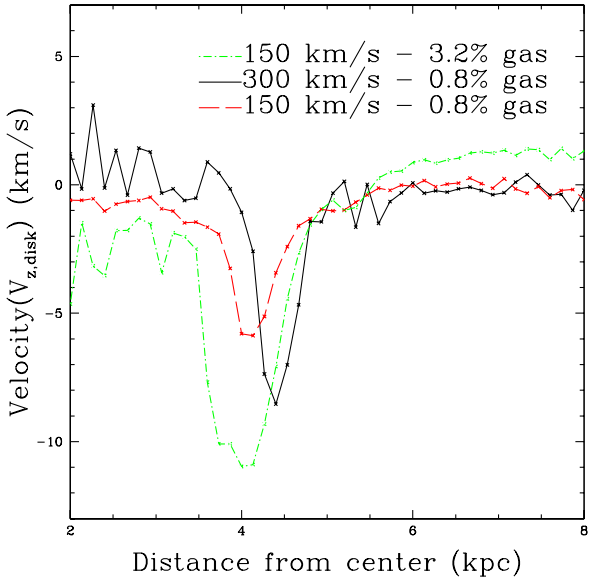

Figure 2.6 Variation of $V_{z,disc}$ with initial velocity. The red curve traces the change in the velocity profile in the z direction for a halo which has 0.8% gas and velocity of v_z = 150 km s^{-1} and the black line for v_z = 300 km s^{-1}, the green curve is for a gas fraction of 3.2% and velocity of 150 km s^{-1}.

2.2.3 Cosmological runs

Our previous simplified setups have shown that dark matter sub-haloes that contain a small fraction of gas can in principle create holes in the HI distribution that resemble the observed ones. The next question to answer now is whether there are enough DM satellites to reproduce the number of observed holes in a galaxy similar to IC 2574.

To answer this question we turn to cosmological N-body simulations which give us the mass, size, velocity and orbital parameters of sub-haloes of the reference galaxy IC 2574. We use the publicly available database of satellite distribution in the Via Lactea II (VLII) simulation (Diemand et al. 2007, 2008). Unfortunately the mass of the parent halo in the VLII simulation ($2 \times 10^{12} M_{\odot}$) is higher than the estimated mass of the halo of our reference galaxy IC 2574 ($10^{11} M_{\odot}$). We thus decide to scale down the properties of the sub-haloes using the following simple dynamically motivated scaling relations:

$$M' = M/10 \tag{2.1}$$

$$v'_{x,y,z} = \frac{v_{x,y,z}}{10^{1/3}} \tag{2.2}$$

$$x' = \frac{x}{10^{1/3}} \quad y' = \frac{y}{10^{1/3}} \quad z' = \frac{z}{10^{1/3}}. \tag{2.3}$$

In order to test that we have not introduced any biases in the satellite properties by rescaling them, we run an additional N-body simulation of a $M = 10^{11} M_{\odot}$ dark matter halo, at a resolution lower than the VLII. We have selected the candidate halo from an existing low resolution dark matter simulation (350^3 particles within 90 Mpc, see Neistein et al. 2010) and re-simulated them at higher resolution using the volume renormalization technique (Katz & White, 1993). The total number of particles within the virial radius at $z = 0$ is $\approx 3.3 \times 10^6$, which gives a mass per particle of $3.05 \times 10^4 \mathrm{M}_{\odot}$. We will refer to this simulation as M11, while we will use M12 for the rescaled version of the VLII simulation. Figure 2.7 shows that sub-haloes of both runs occupy the same phase-space region, which confirms that our simple scaling is valid as first order approximation.[2] We use both satellite distributions (form M11 and M12) in our cosmologically motivated tests.

These N-body simulations predict that a large number of sub-haloes are present around a typical galaxy of $10^{11} M_{\odot}$. In fact we have 798 sub-haloes from the M12 simulation and 468 from the M11 simulation, with masses larger than $10^6 M_{\odot}$, our resolution limit in the N-body simulations. Not all of these haloes pass through the disc. Most of them have nearly circular orbits. Only a few of them have orbits which take them close enough to the center of the halo, and hence interact with the disc, these are the haloes we are interested in. We find interacting haloes by integrating orbits of all sub-haloes in a static

[2] The shelf of high velocity subhaloes at a given distance is due to the higher halo statistics in M12, that allows a better sampling of the tails (positive and negative) of the velocity distribution.

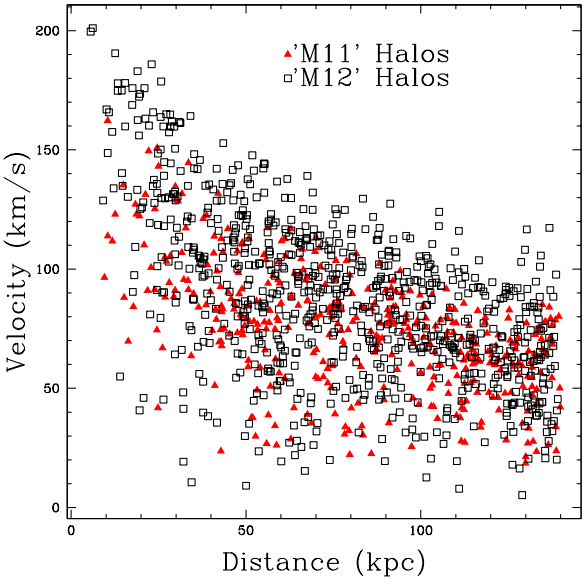

Figure 2.7 The velocity as a function of distance for the M12 sub-haloes(black open squares) after being scaled down and M11 ones (red triangles).

potential for 1 Gyr. This static potential is parametrized with an NFW profile, with the same virial radius and concentration of the original halo extracted from the N-body simulation at $z = 0$.[3] A interaction is defined as the passage of the sub-halo within a cylinder of radius $R = \sqrt{x^2 + y^2} < 8$ kpc and a height $-2 < h_z < 2$ centered at the center of the halo. We obtain a sample of 37 dark matter sub-haloes for M12 and 13 for M11, where the lower number of satellites in the M11 run is due to the its lower resolution compared to the VLII simulation.

In both the M12 and M11 runs DM sub-halo masses range between $1.1 \times 10^6 M_\odot - 1.3 \times 10^7 M_\odot$. We divide these haloes into five halo mass bins. The number of particles in each mass bin and their properties are given in Table 2.1. All haloes in this run have a gas fraction 5% by mass. We put this relatively large amount of gas in these haloes so as to get an upper limit to the number of holes which can be formed.

For each of the mass bins we generate a synthetic halo, using a recipe, which is slightly different from the single halo simulation presented in the previous section. We create a spherical NFW halo with a density contrast of $\Delta = 1000$ with respect to the critical density of the universe, as is typical for sub-haloes (the density contrast for isolated virialized haloes is normally assumed to be $\Delta_{vir} \approx 100$). Each of these haloes contains a gaseous halo in hydrostatic equilibrium with the DM potential. Finally we place back

[3]We use as starting point the Nbody results at $z_i = 0$. Our integration time of 1 Gyr would in principle require $z_i = 0.079$. Such a tiny difference should not affect the sub-halo mass function on the small scales as considered in this work ($M \approx 10^7 M_\odot$).

Table 2.1. Number of haloes and their properties

Mass($M_\odot$)	$N_H - M12$	$N_H - M11$	c_{200}	N_{DM}	N_{Gas}
5.56×10^6	26	10	44.16	556	446
1.01×10^7	7	0	41.65	1010	799
1.46×10^7	3	2	40.16	1463	1158
1.91×10^7	0	0	-	-	-
2.37×10^7	1	1	38.34	2371	1876

Note. — The first column denotes M_{200} in units of solar mass, the second, number of haloes in M12 run, the third, number of haloes in M11 run, the fourth, concentration parameter, the fifth, number of DM particles used to sample the halo and sixth, number of gas particles used to sample the gas in the halo

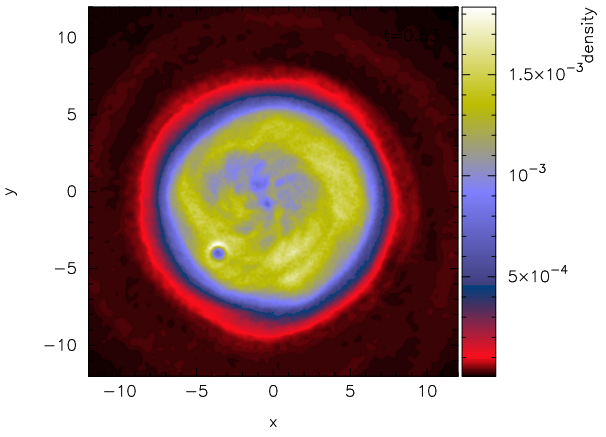

Figure 2.8 Surface density map of the gaseous disc at a particular snapshot of the cosmological run with no winds where the hole is clearly seen at (-4,-4). The units of density are the same as mentioned in previous surface density plots.

our synthetic haloes around the primary galaxy at the same position and with the same velocity as obtained from the N-body simulations.

A combination of high mass and high velocity is needed to produce holes as shown in the previous section. Due to the different orbital parameters such as angle of impact, velocity and mass of the halo, the lifetime of the holes is more varied, ranging from a mere 10 Myr to as much as 70 Myr. Figure 2.8 shows the surface density map of the gaseous disc after 0.53 Gyr, a circular hole of about 1 kpc can be seen in lower left corner of the simulation. The structure seen at the center of the galaxy is the result of local instabilities and star formation.

We now quantify how many holes are produced with respect to observations. We focus on large holes ($R > 1$ kpc), since smaller features can be more easily explained by

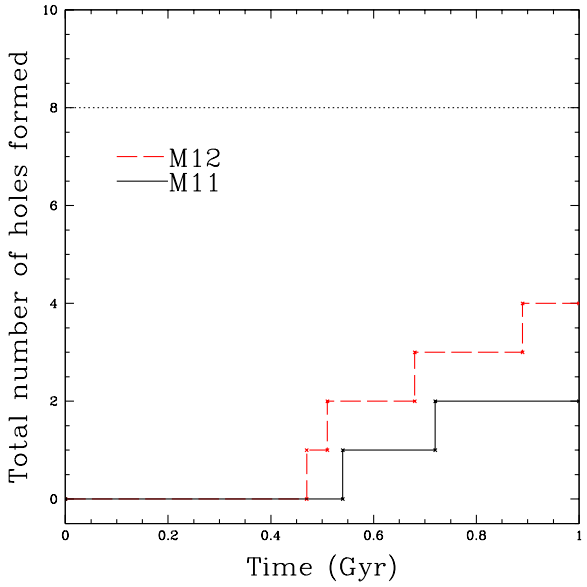

Figure 2.9 Plot showing the cumulative number of holes formed in a span of 1 Gyr in the M11 and M12 simulations. The horizontal black dotted line is the number of holes($d > 1$ kpc) in one snapshot of IC 2574 (Walter & Brinks, 1999). The lower number of holes in the M11 run is, primarily due to its low resolution (compared to M12).

supernovae explosions, stellar winds or a combination of both.

In both our simulation setups (M11 and M12) we observe only $3-4$ events in the 1 Gyr running time (Figure 2.9), with no more than one hole in a particular snapshot (Figure 2.8). On the other hand Walter & Brinks (1999) observed a total of 8 holes with radii greater that 1 kpc in a single "snapshot" of IC 2574 (dotted line in Figure 2.9). The number of holes formed in the M11 run is lower primarily due to lack of resolution (when compared to M12). This results in an under estimation of the total number of low mass satellites.

It emerges clearly that while DM sub-haloes are in principle able to create holes in the HI gas, when a cosmologically motivated sub-halo distribution is used the number of predicted haloes do not match the observed one. This leads us to conclude that the sub-halo - disc interaction is not the principal mechanism to create the observed HI holes.

We note that the number of holes shown in Figure 2.9 is just an upper limit. So far we have assumed that DM sub-haloes will keep their gas (needed to displace the gas in the H I disc) all the way down to the galaxy center, completely neglecting the effect of ram pressure. The ram pressure against the hot gas surrounding the galaxy could partially or totally remove the baryonic content of the sub-halo and make it even more inefficient in producing holes. In order to test this scenario we run an additional simulation, in which we turn on isotropic galactic winds while running the central galaxy in isolation for 1

Gyr to stabilize it (see section 2.1). These winds preferentially expel gas perpendicular to the plane of the disc as it faces the least hindrance in this direction. This creates shells of gas surrounding the galactic plane. This gas (slightly colder than the gas inside the sub-haloes) is efficient is stripping all the gas from the sub-haloes.
When this new initial condition (central galaxy run with winds on) is evolved together with sub-haloes 1 Gyr, it produces virtually no holes. This experiment shows that it is indeed very difficult for the sub-haloes to retain a sufficient amount of gas to perturb the central HI disc. This points to a different process being responsible of the production of large holes in the HI distribution.

2.3 Conclusions & Discussion

Atomic hydrogen (HI) observations of nearby galaxies reveal complex gas distributions. In many systems, the neutral interstellar medium (ISM) contains holes, shells, and/or cavities. In order to understand the origin of these features, we numerically investigate how the impact of dark matter sub-haloes orbiting a gas-rich disc galaxy embedded in a massive dark matter halo influences the dynamical evolution of the HI gas disc of the galaxy. We mainly focus our attention on the creation of large holes ($R > 1$ kpc) in the HI distribution, commonly found in observations of nearby galaxies.
We create a central galaxy resembling the properties of the well-studied dwarf galaxy IC2475 and we bombard its gaseous disc with dark matter dominated satellites. The dark matter, stellar and gas components of both the primary galaxy and the satellites are all live (i.e. made of particles) and a full hydro-dynamical code (GADGET2) including cooling, star formation and feedback is used for these merger simulations.
Our experiment shows that a pure dark matter sub-halo ($M = 10^8 M_\odot$) is not able to displace the gas in the disc, instead due to gravitational focusing it gives rise to a localized high density region. This kind of dark impact might be able to induce star formation in the outer part of the extended gas disc, but cannot create large holes. This result was not unexpected: DM particles interact only through gravity and do not have the necessary contact force to push the gas away from the disc.
These high density tidal imprints can be characterized and studied in order to obtain the properties of the impacting dark sub-halo as done by Chang & Chakrabarti (2011) especially for relatively massive dark satellites (1:100).
To produce holes we need particles which have contact forces, hence we assume a small amount of gas to be present in the dark matter sub-halo. Even a gas fraction as low as 0.8% in a halo of mass $10^8 M_\odot$ with a velocity of 150 km/s is able to produce a detectable low density region. On average holes have a lifetime of about $20 - 60$ Myr, depending on the halo density, gas mass and impact velocity.

We then use satellite properties directly extracted from high resolution Nbody cosmological simulation (Via Lactea II, Diemand et al. 2008), to check how many holes are predicted in the commonly assumed Cold Dark Matter model.
These cosmological motivated runs show that sub-haloes with a relatively high gas fraction (5%), are able to produce a total of about 3-4 large holes ($R > 1$ kpc) in an integration time of 1 Gyr. This number is significantly lower than the number of observed holes of the same size in IC2475 galaxy. If the effect of ram pressure is taken into account, the dark matter satellites tend to loose a significant fraction of their gas content, making them even less efficient at perturbing the HI disc.
We conclude that, although DM matter satellites with a modest gas content are in principle able to create holes with a radius of order 1 kpc, disc - sub-halo interaction are not the primary channel through which these holes form in real galaxies. We consider it likely that other astrophysical processes like supernova explosions, stellar winds, high velocity clouds, or a combination of the above factors are the main causes for the observed complex geometry of extended HI discs.

Chapter 3

From discs to bulges: Role of galaxy mergers in bulge formation

In Chapter 2 we have investigated the effect of extremely minor merger events on the morphology of HI discs. We continue in the same vain in this Chapter and look at how larger merger ratio events affect the morphology of the interacting galaxies. These mergers are considered to be the formation mechanism behind the so called "classical" bulges (i.e. whose properties are similar to Elliptical galaxies, see e.g Davies & Illingworth 1983; Dutton et al. 2013). Therefore investigating the physics of mergers is quite important to understand how elliptical galaxies are formed. The effectiveness of the mergers in converting discs to spheroids also sets the the relative abundance of discs and ellipticals in the Universe.

Observationally, many authors have tried to figure out the relative contribution of bulge and disc components in galaxies in the local universe. Gadotti (2009) calculated the stellar mass content and distribution for each galaxy component, and showed that, for galaxies more massive than 10^{10} $M_{\odot}$ in the local universe, 32 per cent of the total stellar mass is contained in ellipticals, and the corresponding values for discs, bulges and bars are 36, 28 and 4 per cent respectively. Classical bulges contain 25 per cent of the total stellar mass, while pseudo-bulges contain 3 per cent. Kormendy et al. (2010) find four galaxies consistent with being pure disc galaxies and 7 galaxies, including the Milky Way, with pseudo bulges. Given the dearth of classical bulges in their sample, they thus estimate that around $58 - 74\%$ of the galaxies in their sample did not undergo violent mergers in their past and thus they claim that the formation of these massive bulgeless galaxies represents a challenge for current models of galaxy formation. The most refined study of the morphological mix in the SDSS volume has been discussed in Wilman & Erwin (2012); they provide the fraction of galaxies showing a given morphological and activity classification as a function of stellar and parent halo masses. They find that the fraction of elliptical galaxies is a strong function of stellar mass; it is also a strong

function of halo mass, but only for central galaxies. This is treated as evidence for a scenario where elliptical galaxies are always formed, probably via mergers, as central galaxies within their haloes, with satellite galaxies being previously central galaxies accreted onto a larger halo.

Different theoretical tools have been employed to explain and understand these observational evidences. Bulge formation processes in Semi Analytic Models (SAMs) and their relative importance has been studied in detail in a number of recent papers (De Lucia et al. 2010; Fontanot et al. 2011). The general consensus in these works is that, despite the leading role played by galaxy mergers, secular process like disc instability might be key in intermediate-mass galaxies ($10^{10} < M/\mathrm{M}_{\odot} < 10^{11}$): therefore our limited understanding of this mechanism is a limitation for the models' ability of reproducing the morphological mix. In particular, Fontanot et al. (2011) showed that the observed abundance of massive galaxies without a classical bulge is consistent with the predicted abundance of bulgeless galaxies only for a model where disc instability process is not considered. On the other hand, Wilman et al. (in preparation) find that SAMs overpredict the fraction of bulge-dominated galaxies for $M_{\star} > 10^{10.5}\mathrm{M}_{\odot}$ - despite correctly reproducing the fraction of passive galaxies as a function of stellar mass. This implies that even though the merging histories of the haloes are correct, the channels of bulge formation in SAMs are too efficient and revision of the modelling of these physical processes is needed.

Hopkins et al. (2009a) showed that a major factor which determines the morphology of the galaxy after undergoing a merger is the amount of gas in the disc. They suggest that this gas can suppress the transformation of disc to bulge during mergers, providing a mechanism for disc survival in major mergers. They obtain disc dominated remnants even for $1:1$ gas rich mergers. This result has major implications for the amount of bulge dominated galaxies found in the local universe (Hopkins et al. 2009b).

In this paper we re-examine the disc to bulge transformation during mergers. We adopt an hybrid method, first developed by Moster et al. (2014) which is based on high resolution hydrodynamical simulations of merger systems. The dark matter halo properties and their orbital parameters are directly extracted form cosmological simulations, while the properties of the galaxies hosted by those haloes are predicted using a Semi Analytic Model (SAM) of galaxy formation.

In this way we gain the advantages of the merger simulations (high resolution and correct treatment of gas physics) and the SAM (cosmological background). Simultaneously, the computational cost is comparably low, so that a meaningful sample can be modelled in a short amount of time. Given the typical resolution of these hydrodynamical simulations, this method is well suited to resolve the small scales, relevant for the study of the evolution of the stellar components of galaxies and their scale parameters, such as the disc scale length and height, and for the evolution of galaxy morphology. This approach

allows us to achieve the best resolution possible within a reasonable amount of time, while being able to model a sample of galaxies in the correct cosmological context.
We describe the numerical techniques used to simulate mergers in section 3.1 and also give a brief introduction of the SAM used in this study. We enumerate the results in section 3.2 and the conclusions and discussions are given in section 3.3

3.1 Models

In this section we briefly describe the methods that have been used in this paper. These are the code to create initial disc galaxy models, the semi-analytic model used to populate N-body merger trees with galaxies and the hydrodynamic code used to simulate the merger event. Throughout this paper we adapt cosmological parameters chosen to match results from WMAP-3 (Spergel et al., 2007) for a flat ΛCDM cosmological model: $\Omega_m = 0.26$, $\Omega_\Lambda = 0.74$, $h = H_0/(100 \text{ km s}^{-1} \text{ Mpc}^{-1}) = 0.72$, $\sigma_8 = 0.77$ and $n = 0.95$. We adopt a Kroupa (2001) IMF and compute all stellar masses accordingly.

3.1.1 Merger Tree generation : PINOCCHIO

To construct the Dark Matter halo merger trees we make use of the PINOCCHIO code (Monaco et al., 2002). PINOCCHIO uses a scheme based on Lagrangian perturbation theory, and it allows a detailed reconstruction of the DM haloes, with known positions, velocities and angular momenta, and of their merger trees, in excellent agreement with the results of N-body simulations, (see e.g. Li et al. 2007), with a very fine time sampling that provides tracking of merging times without restriction to a fixed grid in time (as in N-body simulations). However, at variance to N-body trees PINOCCHIO DM haloes are not allowed to decrease in mass, and the code does not track the evolution of DM substructures once they have been accreted by the main halo: however, these differences do not constitute a limitation in our case, since the mass evolution of DM substructures is explicitly tracked by the hydrodynamical simulation.

3.1.2 Semi-analytical model: MORGANA

The PINOCCHIO merger trees has then been used as input for the Semi Analytical Model (SAM) MORGANA (Monaco et al. 2007). In SAMs, the evolution of the baryonic component is followed by means of approximate, yet physically grounded, analytical prescriptions for modelling the relevant physical processes (such as gas cooling, star formation and feedback) and their interplay, as a function of the physical properties of model galaxies (like their cold gas and stellar content). These analytical prescriptions involve a number of parameters, usually calibrated by comparing model predictions with a well

defined set of low-redshift observations. Despite (and thanks to) this simplified approach, SAMs have turned into a flexible and powerful tool to explore a broad range of specific physical assumptions, over scales that could not be directly simulated simultaneously (ranging from the accretion onto a super-massive black hole on sub-pc scales to the Mpc scales involved in cosmological structure formation). In the following we will briefly describe the treatment of the most relevant processes leading to bulge formation in MORGANA (see De Lucia et al. 2011, for a discussion of the different channels for bulge formation in different SAMs).

MORGANA distinguishes between minor and major galaxy mergers; the threshold of the two events being defined by a mass ratio between secondary and primary galaxy of 0.3. The orbital decay of dark matter subhaloes and galaxy mergers are modelled using the fitting formulae defined by Taffoni et al. (2003). In case of a minor merger, the stellar mass and the cold gas of the secondary galaxy are completely given to the bulge component of the remnant galaxy, while the disc is considered unaffected. On the other hand, in case of major mergers, the whole stellar and gaseous disc of the merging galaxies are destroyed and relaxed into a spheroidal remnant. In both cases, any cold gas eventually associated with the bulge can be efficiently converted into stars, on very short time-scales (effectively triggering a 'starburst'). At later times, the remnant spheroidal galaxy can grow a new disc, if cooling processes are effective in the parent halo. In particular for this work, we make use of the standard realization of MORGANA defined in De Lucia et al. (2011).

3.1.3 Galaxy models for N-body simulations

To construct the galaxy models used as initial conditions in our simulations we apply the method described in Springel et al. (2005a) with the extension by Moster et al. (2011). Each system is composed of a cold gaseous disc, a stellar disc and a stellar bulge with masses $M_{\rm cg}$, $M_{\rm disc}$ and $M_{\rm b}$ embedded in a halo that consists of hot gas (Tumlinson et al., 2011b) and dark matter with masses $M_{\rm hg}$ and $M_{\rm dm}$.

The gaseous and stellar discs are rotationally supported and have exponential surface density profiles. The scale length of the gaseous disc $r_{\rm g}$ is related to that of the stellar disc $r_{\rm d}$ by $r_{\rm g} = \chi r_{\rm d}$. The structure of the stellar disc, gasoues disc, bulge and dark matter halo are setup by the method described in §2.1.1 (except that we do not include a constant radial component of gas disc in this work).

In addition, we also include a hot gaseous halo. We use the method employed by Moster et al. (2011). Briefly, the hot halo is modeled as a slowly rotating halo with a spherical density profile. A observationally motivated β-profile (Cavaliere & Fusco-Femiano 1976,

Jones & Forman 1984, Eke et al. 1998) is used:

$$\rho_{\rm hg}(r) = \rho_0 \left[1 + \left(\frac{r}{r_{\rm c}}\right)^2\right]^{-\frac{3}{2}\beta} , \tag{3.1}$$

which has three free parameters: the central density ρ_0, the core radius $r_{\rm c}$ and the outer slope parameter β. Following Moster et al. (2011), $\beta = 2/3$ (Jones & Forman, 1984), $r_{\rm c} = 0.22 r_{\rm s}$ (Makino et al., 1998) is adopted and ρ_0 is fixed such that the hot gas mass within the virial radius is $M_{\rm hg}$.

The temperature profile is fixed by assuming an isotropic model and hydrostatic equilibrium inside the galactic potential such that it is supported by pressure. In addition, the hot gaseous halo is rotating around the spin axis of the discs with a specific angular momentum $j_{\rm hg}$ that is a multiple of the specific angular momentum of the dark matter halo $j_{\rm dm}$ such that $j_{\rm hg} = \alpha j_{\rm dm}$. The angular momentum distribution is assumed to scale with the product of the cylindrical distance from the spin axis R and the circular velocity at this distance: $j(R) \propto R\, v_{\rm circ}(R)$.

For the spin factor α one finds in high resolution cosmological simulations that at low redshift ($z \lesssim 2$) it is generally larger than 1, as feedback processes preferentially remove low angular momentum material from the halo (Governato et al., 2010). Similarly, Moster et al. (2011) constrain α by using isolated simulations of a MW-like galaxy and demanding that the evolution of the average stellar mass and scale-length found observationally be reproduced. The model that agrees best with the observational constraints is that with a spin factor of $\alpha = 4$. We use this value throughout this work.

3.1.4 Simulations of Semi-Analytic Merger Trees

In this section we describe a method which combines the advantages of merger simulations (high resolution and detailed treatment of gas physics) with the advantages of SAMs (cosmological background). Specifically, we use SAMs to populate N-body merger trees (extracted from the PINOCCHIO run) with galaxies and then use them as the initial conditions for hydrodynamical multiple merger simulations.

The details of this method has been described in detail in Moster et al. (2014). A brief schematic view of our method is presented in Figure 3.1. The first step is to select a dark matter merger tree from the large-scale N-body simulation and use the SAM to predict the properties of the baryonic components of each halo at every time-step. A resulting merger tree is shown in the left side of Figure 3.1 where the time runs from top to bottom. A starting time t_i is chosen, after which we want to simulate this tree. In the simple example, the main system experiences four mergers after t_i. Predictions by the SAM for the central galaxy of the main halo at t_i are used to create a particle realization with the galaxy generator, as indicated by the brown arrow. This model galaxy is shown

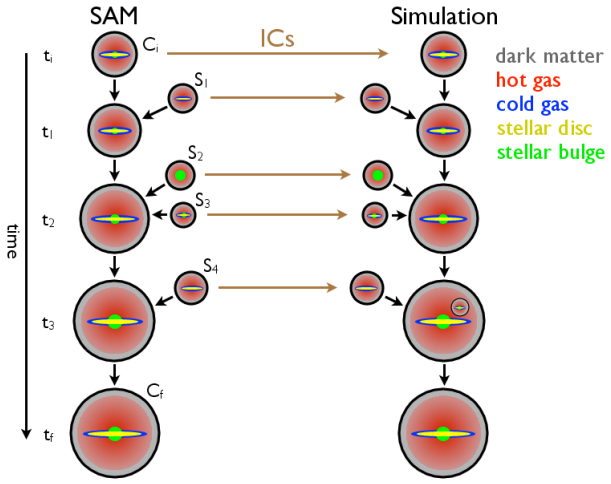

Figure 3.1 Schematic view of the combination between semi-analytic models and merger simulations (taken from Moster et al. 2014). On the left side the semi-analytic merger tree is shown and the time runs from top to bottom. At the starting time t_i, initial conditions for the central galaxy are created using the properties of the central galaxy in the SAM at this time. This system is then simulated with the hydrodynamical code until the time of the first merger t_1, where the first satellite S_1 galaxy is put into the simulation using the properties predicted by the SAM. The resulting merger is simulated until the next galaxies (S_2 and S_3) enter the main halo at t_2, at which point they are also included in the simulation. This procedure is repeated for all mergers until the final time of the run t_f.

in the top right of Figure 3.1 and in the example consists of a dark matter halo (grey), a hot gaseous halo (red), a cold gaseous disc (blue), a stellar disc (yellow) and a small stellar bulge (green). This galaxy is evolved with the hydrodynamical code until the time t_1 when the first satellite galaxy S_1 enters the main halo. A particle realization of the S_1 system (dark halo and galaxy) is then created using the semi-analytic prediction for the galaxy properties and included in the simulation at the virial radius of the main halo. The orbital parameters of S_1 (position and velocity at the time of accretion) are directly taken from the N-body simulation, in this way "naturally" creating a cosmologically motivated merger. This system is evolved with the hydrodynamical code, until the next satellite galaxy enters the main halo. This process is repeated for all merging satellites until the final time t_f.

The model thus requires two main steps: creating particle realizations of galaxies as predicted by the SAM and combining the these initial conditions in a simulations as determined by the merger tree (i.e. every galaxy has to enter the simulation at the specified time and position). This means we first have to specify how the information about the galaxy properties that is computed with the SAM, is transformed into three dimensional particle based galaxy models that can be simulated with a hydrodynamic code. Then we have to determine how the satellite galaxies are included in the simulation, so their

Table 3.1 Summary of the parameters used for the simulations of merger trees and their fiducial value.

Parameter	Description	Fiducial value
z_i	Redshift at the start of the simulation	1.0
$\mu_{\rm min}$	Minimum dark matter mass ratio	0.03
ζ	Ratio of scaleheight and scalelength of the stellar disc	0.15
χ	Ratio of scalelengths between gaseous and stellar disc	1.5
ξ	Ratio of gaseous halo core radius and dark matter halo scaleradius	0.22
$\beta_{\rm hg}$	Slope parameter of gaseous halo	0.67
α	Ratio of specific angular momentum between gaseous and dark halo	4.0
N_*	Expected final number of stellar particles in the central galaxy	200 000
κ	Ratio of dark matter and stellar particle mass	15.0
$N_{\rm res,sat}$	Ratio of satellite and central galaxy particle mass	1.0
$N_{\rm min}$	Minimum number of particles in one component	100
ϵ_1	Softening length in kpc for particle of mass $m = 10^{10}{\rm M}_\odot$	32.0
t_0^*	Gas consumption time-scale in Gyr for star formation model	$3.5^\dagger$
A_0	Cloud evaporation parameter for star formation model	$1250.0^\dagger$
$\beta_{\rm SF}$	Mass fraction of massive stars for star formation model	$0.16^\dagger$
$T_{\rm SN}$	Effective supernova temperature in K for feedback model	$1.25 \times 10^{8\dagger}$
ζ	Mass loading factor for wind model	1.0
$v_{\rm wind}$	Initial wind velocity in $\,{\rm km\,s^{-1}}$ for wind model	500.0

† The star formation parameters assume a Kroupa IMF.

position and velocity have to be calculated. We note that the starting time t_i, or the starting redshift z_i, respectively, can also be chosen such that the simulation starts at a very early epoch. In this case the central galaxy consists only of a dark matter halo and hot gas in this halo. The dark matter will then grow by mergers and smooth accretion, and the stellar disc and bulge will form as a result of cooling and accretion of gas, and merger events. All parameters used to construct our galaxies from the initial conditions given by the SAM and the other simulation parameters are taken from Moster et al. (2014) and they are reproduced in the Table 3.1.

Finally, the hydrodynamical simulations of the semi analytic merger trees are performed using the TreeSPH-code GADGET-2 (Springel, 2005, also described in Chapter 1). The simulation parameters for the code are the same as described in §2.1.

3.2 Morphological evolution of galaxies

As mentioned earlier the most important processes which dictates the morphology of galaxies are mergers and close encounters. These processes are known to trigger mass transfer into the central bulge through different channels; the main ones being : (i) accretion of satellite material onto the bulge of the central galaxy (central bulge) during

a merger, (ii) the transfer of material from the disc of the central galaxy (central disc) to central bulge and (iii) funnelling of gas towards the centre and subsequent star formation, As described in Sec. 3.1.2, SAMs use simple prescriptions for mass transfer through these channels. Are these prescriptions correct? For example the simple assumption that during a major merger all the material of the central disc goes into the bulge has been contradicted by Hopkins et al. (2009a), who showed that discs can survive major mergers if they are gas rich. Chang et al. (2013) showed that a disc dominated satellite will be more easily tidally stripped as it orbits a halo before it finally mergers, which reduces the amount of material given by the satellite to the central bulge.
Here we test different different scenarios using high resolution hydrodynamical simulations of galaxy mergers, starting from the initial conditions given by the semi-analytic model as described in the previous section. We simulate a total of 13 merger events covering a range of different merger histories and galaxy properties. The merger trees and their parameters are given in Table 3.2. For each tree we also perform an 'isolation' run, i.e. a run where the central galaxy is evolved without any mergers from $z = 1$ to the present time.

3.2.1 Bulge/Disc Decomposition

There are many different ways to decompose the mass of a galaxy into its basic morphological entities i.e., disc and bulge, for example fitting surface brightness profiles with a bulge and disc component (e.g., Robertson et al. 2006), kinematic decompositions based on one or two dimensional kinematic maps (e.g. Cox et al. 2006b) and three dimensional component fits. All these methods rely heavily on the viewing angle. In this paper we make use of the six dimensional phase space of $(\mathrm{x}, \mathrm{y}, \mathrm{z}, \mathrm{v_x}, \mathrm{v_y}, \mathrm{v_z})$, to track the bulge and the disc components of the primary galaxy, throughout the simulation. The galaxy in question is viewed edge on i.e., the angular momentum vector of the disc is placed parallel to the z axis. Now for a purely rotating disc the circular velocity of a given particle, at a distance r is given by

$$v_c = \sqrt{\frac{GM(<r)}{r}} \tag{3.2}$$

and the specific angular momentum of the particle will be

$$l_c = r\sqrt{\frac{GM(<r)}{r}} \tag{3.3}$$

If a particle is purely rotationally supported then the ratio of its specific angular momentum in the z direction and l_c will be equal to 1.

$$l_{rot} = \frac{l_p}{l_c} \tag{3.4}$$

Table 3.2 Table listing the properties of simulated merger trees

Tree/Sat ID	z_{enter} [a]	μ [b]	μ_b [c]	$log(M_h)$ [d]	$log(M_*)$ [e]	$log(M_{cg})$ [f]	η(orbit) [g]
Tree 18989	1.0	-	-	11.70	9.92	10.06	-
Sat 1	0.98	0.37	0.83	11.27	9.92	9.65	0.20
Tree 28678	1.0	-	-	11.67	10.44	9.62	-
Sat 1	0.46	0.56	0.16	11.47	9.66	8.74	0.44
Tree 80891	1.0	-	-	11.86	10.61	9.65	-
Sat 1	0.81	0.05	0.037	10.67	8.80	8.92	0.81
Tree 65521	1.0	-	-	11.81	10.48	10.21	-
Sat 1	0.77	0.10	0.05	10.84	9.05	8.93	0.43
Tree 154448	1.0	-	-	11.631	10.60	9.83	-
Sat 1	0.67	0.97	0.74	11.651	10.74	8.79	0.42
Tree 215240	1.0	-	-	11.54	9.84	9.88	-
Sat 1	0.37	0.76	0.47	11.52	9.86	8.21	0.13
Tree 455141	1.0	-	-	11.39	10.14	9.54	-
Sat 1	0.56	0.88	0.38	11.45	9.48	9.54	0.56
Tree 114590	1.0	-	-	11.15	9.16	8.96	-
Sat 1	0.92	0.86	0.84	11.10	9.12	9.32	0.71
Tree 28837	1.0	-	-	11.86	10.42	9.94	-
Sat 1	0.72	0.04	0.01	10.52	8.48	7.33	0.31
Tree 350	1.0	-	-	11.90	10.77	9.84	-
Sat 1	0.96	0.13	0.041	11.02	9.25	8.67	0.35
Sat 2	0.95	0.04	0.016	10.53	8.75	8.52	0.21
Sat 3	0.93	0.04	0.009	10.62	8.67	7.73	0.36
Tree 2536	1.0	-	-	11.63	10.36	10.15	-
Sat 1	0.79	0.12	0.025	10.75	8.76	8.28	0.69
Sat 2	0.75	0.29	0.312	11.20	9.98	6.20	0.66
Sat 3	0.46	0.19	0.135	11.18	9.46	8.94	0.31
Tree 187460	1.0	-	-	10.94	9.14	9.21	-
Sat 1	0.70	0.80	0.85	11.09	9.17	8.82	1.05
Sat 2	0.61	0.66	0.79	11.32	9.26	8.10	0.63
Tree 159419	1.0	-	-	11.05	9.08	8.26	-
Sat 1	0.89	0.52	0.41	10.79	8.75	7.80	0.18
Sat 2	0.88	0.77	0.66	11.15	9.34	8.15	0.49

[a] Redshift of entry of the halo
[b] Dark Matter merger ratio
[c] Baryon merger ratio
[d] Dark Matter mass
[e] Stellar mass
[f] Cold gas mass
[g] Circularity parameter

where

$$l_p = r(x, y) \times v(x, y) \tag{3.5}$$

is the specific angular momentum of the particle in the z direction. If we consider all the stellar component of a sample galaxy from our simulations and plot the distribution of the mass fraction as a function of the rotational support i.e., l_p/l_c (Fig. 3.2(a)), we expect it to be bi-modal with the rotationally supported disc particles distributed around $l_{rot} \approx 1$ and the velocity dispersion (σ) supported bulge particles grouping around $l_{rot} \approx 0$. This decomposition on a sample galaxy at redshift z=1, from our catalog (tree 350) gives a $B/T \sim 0.7$, which is confirmed by the initial conditions taken from the SAM. The stellar density maps (figure 3.2(b)) also confirm that this is a bulge dominated galaxy.

Figures 3.3(a),3.3(b) show the effect of a minor and major merger and how the angular momentum distribution of matter in the central galaxy changes in our simulations. A minor merger does not particularly affect the morphology of the galaxy (Fig.3.3(a)) which remains disc dominated (tree 65521). On the other hand a multiple major merger completely changes the galaxy morphology as shown in of Fig. 3.3(b). A disc dominated galaxy turns into bulge dominated one with a very small hint of a remnant disc (tree 187460).

This method also allows us the track the mass flow into the central bulge during the whole simulation, as shown in figure 3.4 (tree 65521; $\mu = 0.1$) and 3.5 (tree 18989; $\mu = 0.76$). These figures show the evolution of various properties as a function of simulation time. The top left panel in these figures shows the evolution of the bulge/total ratio of the central galaxy in both merger (solid curve) and isolation (dotted line). During a minor merger the difference between the B/T ratio is minimal whereas when a galaxy undergoes a major merger the B/T ratio increases considerably. The middle panel on the left shows the distance of the satellite to the central galaxy. Due to the dependence of the merging time on the mass ratio of the merger, a low mass merger satellite spends more time orbiting the primary galaxy. The bottom panel on the left shows the mass loss of the satellite. The low mass satellite undergoes numerous close encounters, losing most mass of its mass to the central halo in the process, whereas the high mass satellite has fewer orbits and deposits almost all of its mass into the primary. The top panel on the right shows the amount of satellite stellar mass given to the central bulge and it is seen that a minor satellite deposits very little of its stellar mass into the central bulge owing to the fact that most of its mass is stripped away and lost to the halo during its descent while a massive satellite deposits almost all of its mass into the central bulge as it spends less time orbiting and it is also able to hold on to more of its mass before it merges. The middle panel on the right shows the evolution of the amount of central stellar disc mass given to the central bulge during a merger (solid curve) and in isolation (dotted curve).

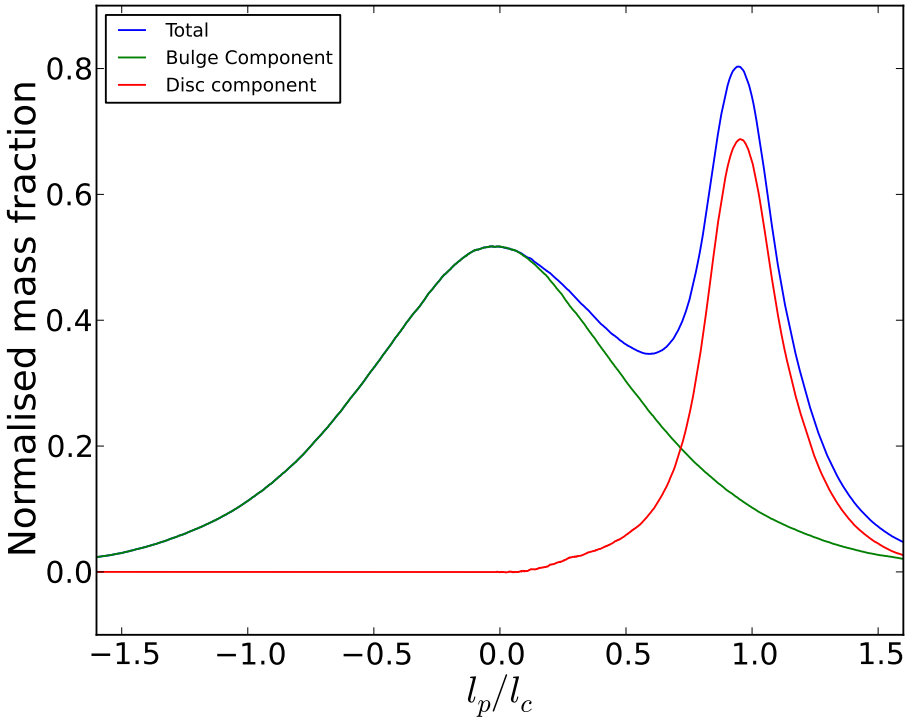

(a) The mass distribution of the stellar component of the galaxy as a function of the rotational support. There is clearly a bi-modal distribution, with clear difference between the bulge (green) and disc (red) components, which can be easily decomposed to get the mass in each component. This particular decomposition yields a $B/T \approx 0.7$

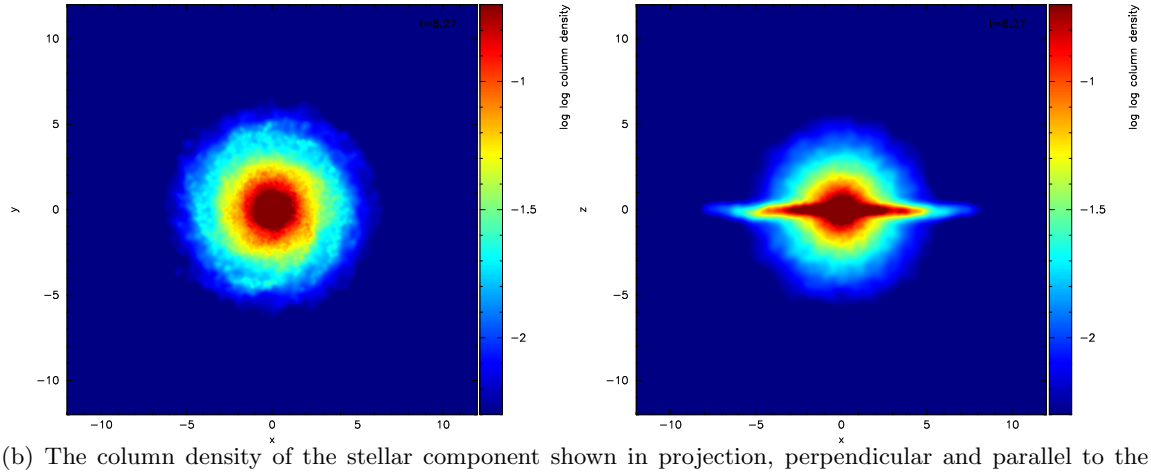

(b) The column density of the stellar component shown in projection, perpendicular and parallel to the total angular momentum axis of the galaxy

Figure 3.2 An sample decomposition of a bulge dominated galaxy in our simulations

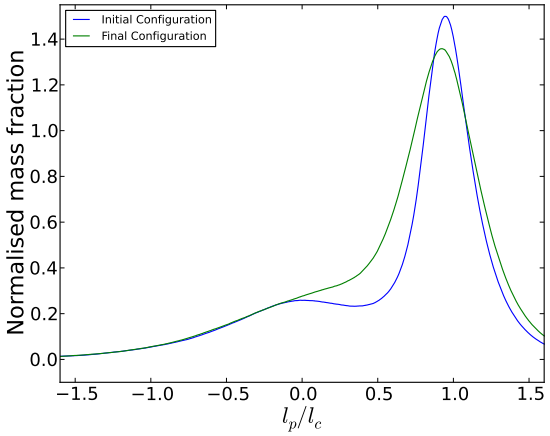

(a)

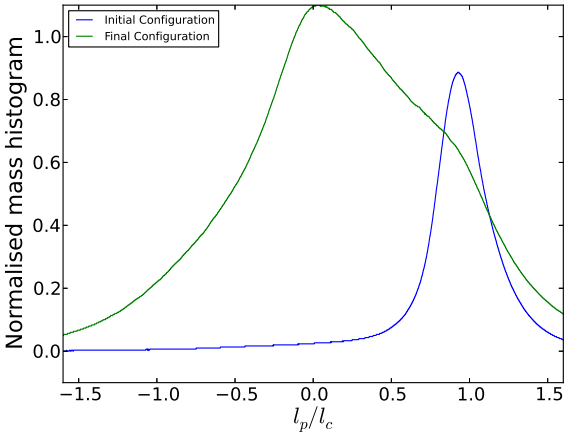

(b)

Figure 3.3 Change in the angular momentum distribution of the central galaxy before and after a merger event. Left Panel (Fig 3a): Change in stellar mass distribution of the central galaxy after undergoing a 1:10 merger. The merger heats up the thin disc, leaving the bulge almost completely unaltered. Right Panel (Fig 3b): Change in stellar mass distribution of the central galaxy after undergoing a 1:1.31 merger. Due to the high merger ratio, the galaxy builds up a large bulge.

There is almost no mass transfer form the central disc to the central bulge in case of a minor merger, but during a major merger about 30% of the central stellar disc ends up in the central bulge. This number is very small compared to most SAM prescriptions which assume that almost all the stellar mass of the central disc ends up in the bulge during a major merger. As we will discuss later a large fraction of the central disc gets dispersed into the stellar halo, and a small remnant disc survives. The bottom panel on the right, shows the composition of the central bulge. The brown line denotes the fraction of stars which existed in the central bulge at the start of the simulation, the blue line is the contribution from the satellite and the black (solid and dotted) lines are

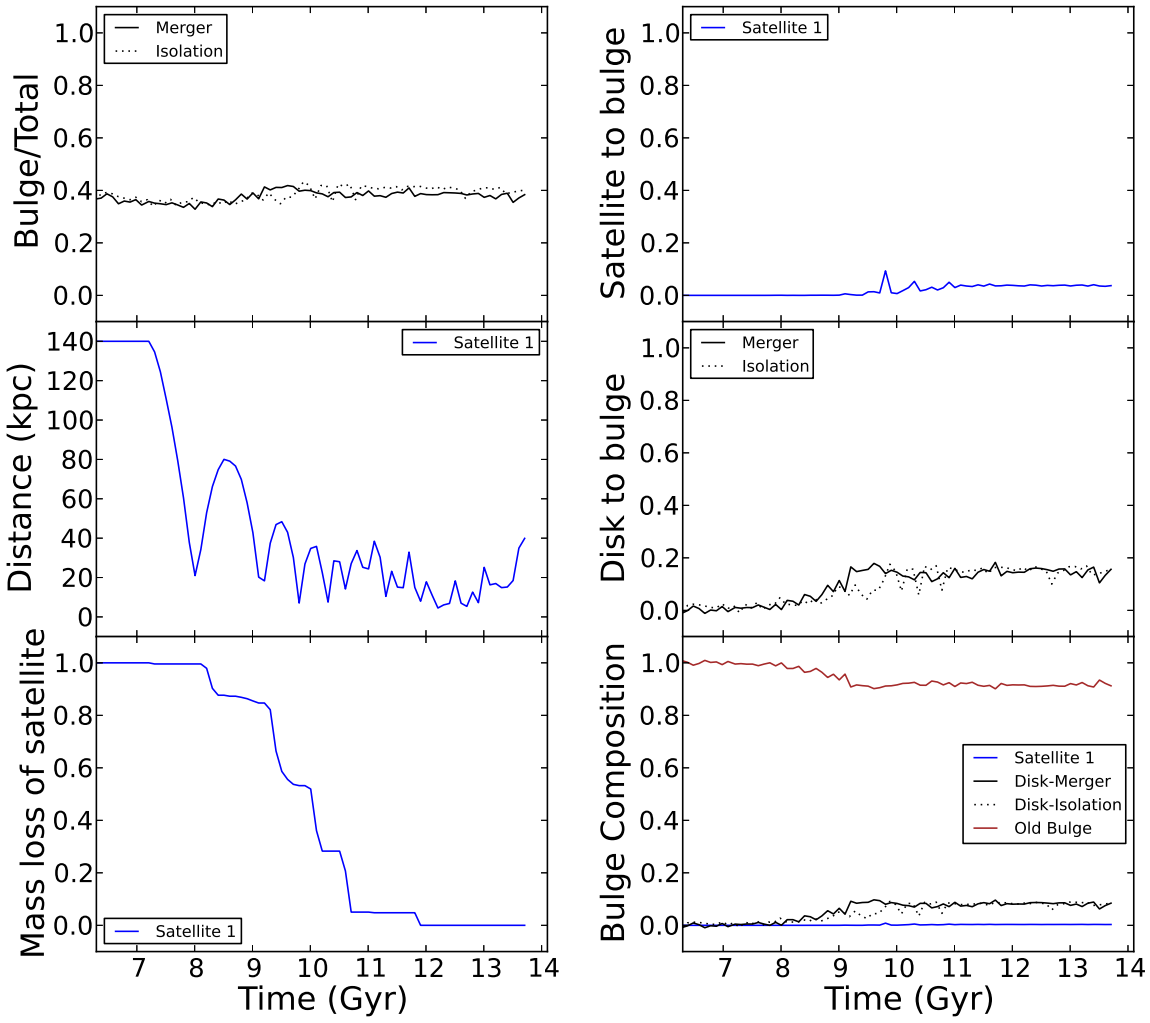

Figure 3.4 Plot showing the evolution of various quantities as a function of time for a galaxy with a merger ratio of $\mu = 0.1$. Panel 1 - Evolution of B/T in both the isolated and merger runs, Panel 2 - Distance of the satellite form the centre of the primary galaxy, Panel 3 - Mass loss of the stellar component of the satellite as it orbits in the primary halo of the central galaxy, Panel 4 - Stellar mass of the satellite given to bulge of the primary galaxy, Panel 5 - Amount of initial disc mass given to the bulge, and panel 6 - Composition of the bulge.

the contribution from the central disc during a merger and in isolation. As expected the low mass satellite contributes little, while a high mass satellite contributes a large amount of material to the bulge and, in the end, it dominates the bulge composition in this particular example.

In the following sections we look closely at the various channel for mass transfer into the bulge and try to quantify them with simple, physically motivated, empirical relations.

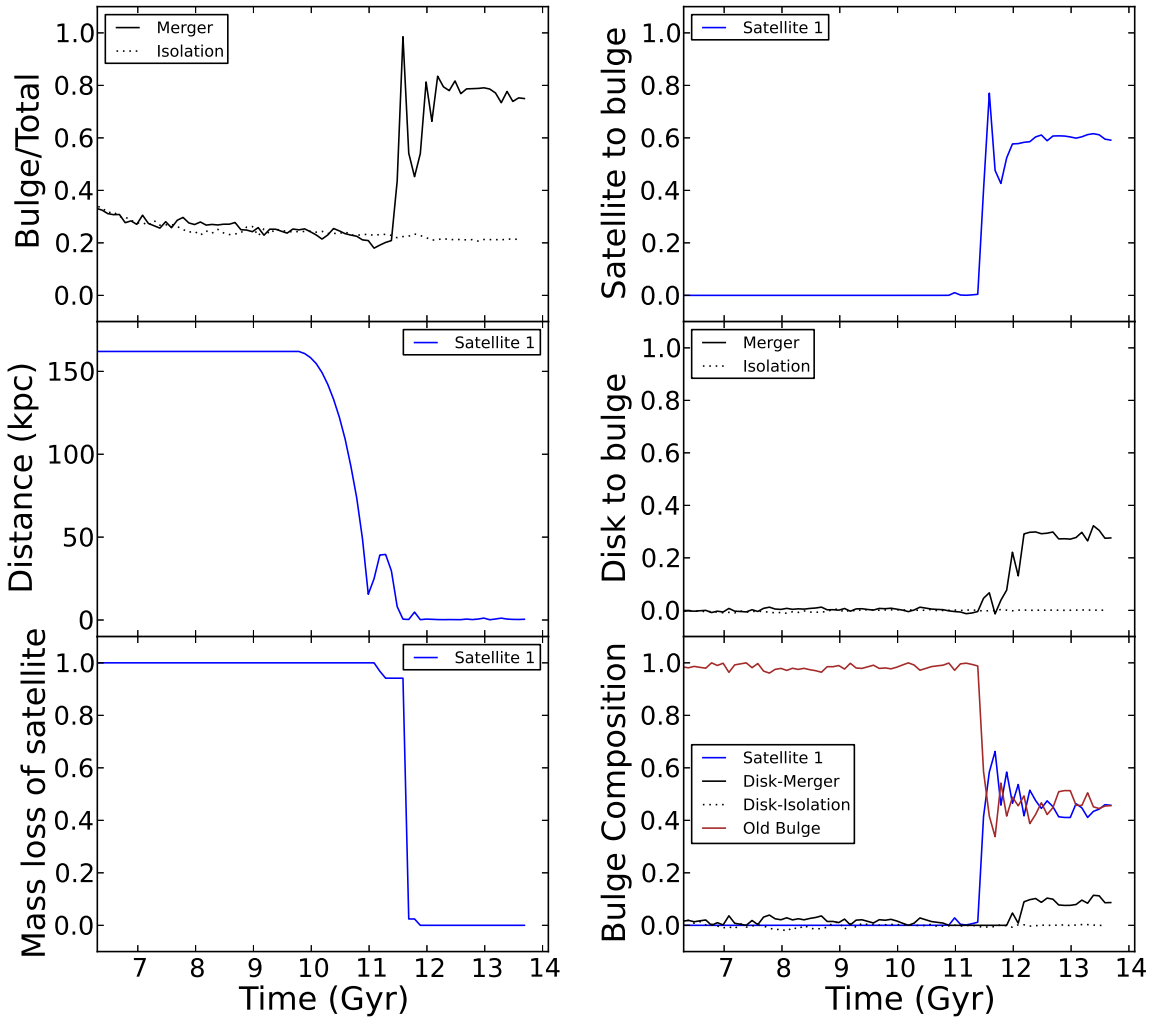

Figure 3.5 Plot showing the evolution of various quantities as a function of time for a galaxy with a merger ratio of $\mu = 0.37$. The panels are the same as described in Figure 3.4

3.2.2 Where does the satellite mass end up?

As mentioned previously, the MORGANA model employs a simple set of formulae to evolve the bulge mass during mergers. For example it is assumed that the whole satellite mass is added to the bulge, irrespectively of the mass ratio between the satellite and the host and/or the orbit of the satellite, similar prescriptions hold for most SAMs.

A satellite on a circular orbit, will orbit the galaxy for a longer time before merging. As consequence it will deposit a large amount of its dark matter and stellar mass in the halo, before finally merging with the central galaxy (e.g. Chang et al. 2013).

We define f_{sb} as the fraction of the initial (before infall) mass of the satellite given to the central bulge. This fraction will mainly depend on two factors: the merger mass ratio μ and the eccentricity of the orbit e. This latter quantity could be expressed as a function of the ratio between the orbital angular momentum of the satellite (j) and $j_c(E)$ the angular momentum of a circular orbit with the same energy as the satellite, i.e.,

$$\eta = \frac{j}{j_c(E)}. \tag{3.6}$$

We expect f_{sb} to be directly proportional to the halo merger ratio μ and inversely proportional to $\exp(1.9\eta)$, where the exponential function and the proportionality factor of 1.9 comes from the relation between η and the total merger time for satellites derived by Boylan-Kolchin et al. (2008) from cosmological simulations. The parameter $\mu/exp(1.9\eta)$ is a proxy for the the number of close encounters a satellite experiences before the final merger. This is an important number as it determines the effective merger ratio after mass loss in the orbit, and the gravitational impulse of the satellite on the central galaxy will be proportional to this parameter. Moreover the extra orbital dependence $\exp(1.9\eta)$ gives a better fit to our simulation results and decreases the χ^2 by a factor larger than 2 in all our empirically derived relations for the bulge mass growth through various channels.

Figure 3.6 show the results for f_{sb} from our suite of simulations (blue stars). The simulations data show a significant dependence of f_{sb} on the satellite mass and orbit. In minor mergers the satellite has a longer dynamical friction time and hence will deposit more mass (stars and dark matter) in the host halo. The opposite is true in major mergers (high μ) or in mergers with low η, in which case the satellite will fall directly onto the central galaxy, depositing the majority of its stellar mass in the central bulge. We have tried to capture this behaviour with a simple fitting formula:

$$f_{sb} = \frac{5.21x}{1 + 4.21x} \text{ where } x = \frac{\mu}{\exp[1.9\eta]} \tag{3.7}$$

represented by the green line in figure 3.6, which is a fair representation of the simulations results, while being still simple to implement in analytical models.

3.2.3 Where does the central disc mass end up?

Another major channel to build up the bulge is the transfer of mass from the central disc (stars and gas) into the central bulge during a merger (f_{db}). In the MORGANA code the following formula is used to determine the mass (M_{db}) transferred through this channel is given by:

$$f_{db} = \frac{M_{db}}{M_{disc}} = \begin{cases} 0 & \mu \leq 0.3 \\ 1 & \mu > 0.3 \end{cases} \tag{3.8}$$

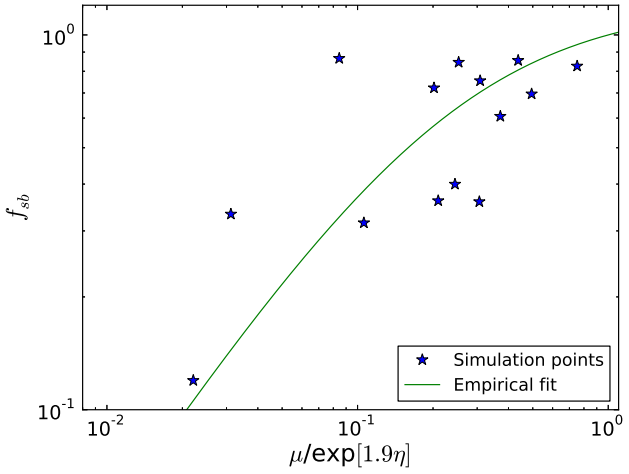

Figure 3.6 The fraction of satellite mass given to the central bulge as a function of their DM merger ratios and orbital parameters. The green curve is out fit to the simulated data (blue stars).

where M_{disc} is the central disc mass (stars and gas). On the other hand the gaseous and stellar components of the disc behave differently as pointed out by H09. They have shown that if the central disc is gas rich then only a small amount of its initial gas is funnelled into the bulge. This mass transfer is given by the following relation

$$f_{cgb} = (1 - f_{gas})\mu \tag{3.9}$$

where f_{cgb} is the fraction of the central disc gas mass transferred to the central bulge, and f_{gas} is the gas fraction of the central disc (ratio between gaseous and stellar disc mass) and μ is the merger ratio.

In this section we show the results of single merger events in our simulations inventory. The effect of multiple mergers on the central disc are very hard to entangle and they do more damage than single isolated mergers. We also see a stronger dependence on the baryonic merger ratio (μ_b) than the DM merger ratio μ for all of the central disc mass transfer channels. This is not surprising since the central disc is mainly perturbed by the innermost baryonic component of the incoming satellite.

Results from our simulations are shown in figure 3.7. As discussed earlier we find an extra (weak) dependence of f_{cgb} on the merging satellite orbital parameter. We find an empirical relation for the amount of mass transfer into the bulge given by

$$f_{cgb} = min\left[1, 1.3(1 - f_{gas})\frac{\mu_b}{exp[1.9\eta]}\right] \tag{3.10}$$

shown as solid (green) line in figure 3.7. We confirm previous results on the importance of the gas fraction in determining the gas transfer from central disc to central bulge,

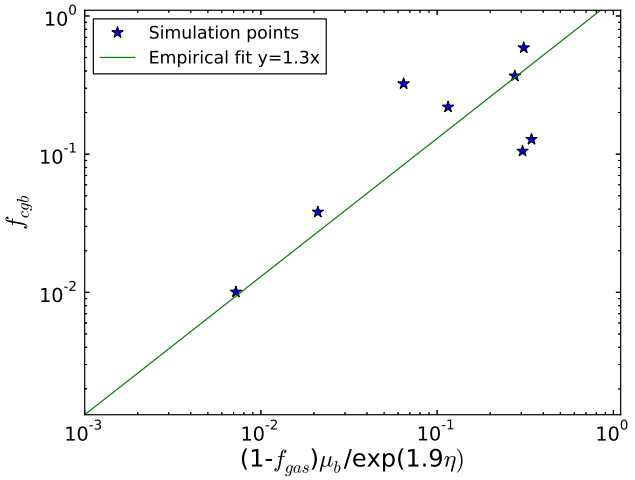

Figure 3.7 The fraction of gas central disc mass given to the central bulge. The blue points are simulation results and the green line is the empirical fit to the points.

with gas rich discs able to retain a larger amount of their own gas, however the value of the proportionality constant of ~ 1.3 is a bit higher than the value obtained by H09.
On the other hand we find quite a substantial difference with previous studies for what concerns the fate of the central stellar disc after a merger. SAMs assume that all the stellar mass of the central disc ends up in the central bulge after a major merger, while H09 found that this mass transfer is given by

$$f_{db} = \mu_h \tag{3.11}$$

where μ_h is defined as the total mass (DM+baryons) in the central regions of the galaxy. However in our simulations even for a $1:1$ merger on a radial orbit the amount of central stellar disc mass that ends up in the bulge is only about 50%, as show in Fig. 3.8. The empirical fit to simulation data points is given as

$$f_{db} = 0.50x \text{ where } x = \frac{\mu_b}{exp[1.9\eta]} \tag{3.12}$$

where f_{db} is the fraction of central stellar disc mass that ends up into the bulge.
This result is pretty surprising and questions the assumed efficiency of mergers in creating bulges. Now the question is: where does the rest of the disc end up? Major mergers are very violent events, a lot of energy (mainly orbital) is quickly transferred to the disc stars. As a consequence a substantial fraction of the central stellar disc is ejected into the stellar halo. In our simulations the stellar halo is defined as all the stellar content present outside three scale radii of the central disc and/or 5 kpc above or below it. Figure 3.9 shows the fraction of central disc stellar mass that is dispersed into the stellar halo of the galaxy as a function of the merger ratio and orbital parameter.

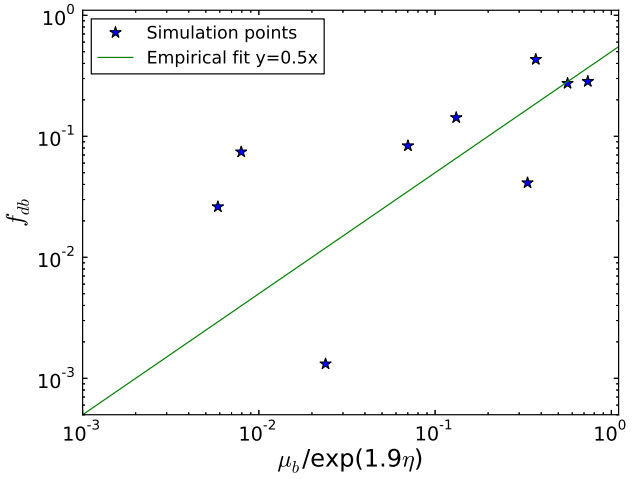

Figure 3.8 The fraction of the central stellar disc mass that ends up in the bulge of the galaxy as a function of merging parameters. The blue points are our simulation results and the green line is the fit to our result.

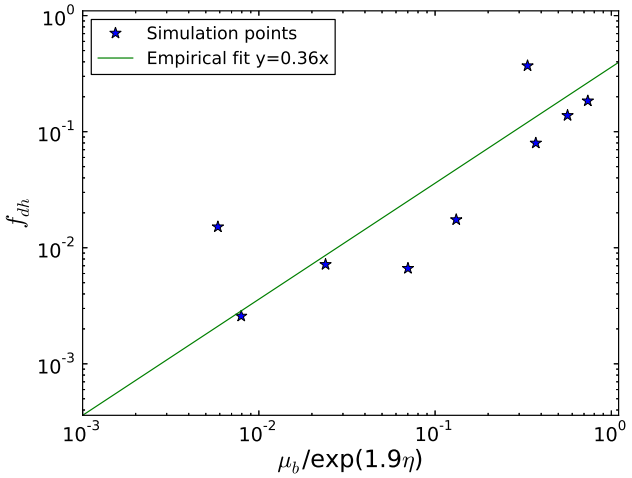

Figure 3.9 The fraction of the central disc mass transferred to the halo as a function of the merger ratio and orbital parameters. The green curve is out fit to the data. A significant fraction of the stars end up in the stellar halo of the central galaxy.

A disc destroyed during a major merger does not entirely end up in the newly formed bulge but a significant fraction of its mass, up to $\sim 35\%$, is ejected into the halo. If this mass transfer from the central disc to the halo is neglected then the bulge fraction of galaxies will be significantly overestimated. Empirically we find that the fraction of central disc mass dispersed in to the stellar halo during a merger (f_{dh})is given by

$$f_{dh} = 0.36x \text{ where } x = \frac{\mu_b}{exp[1.9\eta]}. \tag{3.13}$$

These results show a revised picture of the the fate of a central stellar disc during a

major merger. Half of it's mass looses angular momentum and is then transferred into the bulge. More than a third the initial mass gains enough energy to escape from the central region and is dispersed into the galactic halo. Finally a small part of the disc is able to survive the merger and form a smaller (thicker) disc structure around the newly formed bulge. These results show that mergers are not as effective as previously thought in creating galactic bulges.

3.2.4 Sites of star formation during a merger

Many people have looked at the efficiency of star bursts. (Cox et al. 2008; H09; Karman et. al. in prep.). H09 assume that all the disc gas mass that enters the bulge during a merger will be available for star formation and there is a particular efficiency for the conversion of this gas into stars. Cox et al. (2008) have looked at star burst efficiency of the entire galaxy, but they assume that star formation mainly takes place in the bulge of the galaxy.

Here we check if the above mentioned scenario is true by looking at enhancement of star formation in mergers and sites of these enhancements. The top panel of Fig 3.10 shows the fractional change in star formation rate, i.e., the star formation in merger simulation minus star formation in isolated galaxy divided by the star formation in isolated galaxy, as a function of the merger ratio for both bulge (red circles) and disc (blue stars) component. We see that in most cases the star formation is enhanced both in the bulge and the disc. For very minor mergers we see an increase in SF by about 10% in both the bulge and disc, whereas in major mergers the SF in the bulge can be enhanced as high as 80 times the original value. On the other hand there is relatively low enhancement (of about 20 times) in the SF in the disc during a major merger.

When can then turn the previous plot around and look at, for a particular enhancement in SF, what fraction of it takes place in the bulge and disc. The bottom panel of fig.3.10 shows the fraction of SF enhancement which takes place in the bulge and disc. As shown clearly, a large fraction of the SF occurs in the disc for minor mergers (disregarding massive outliers) as these low mass mergers mainly excite local instabilities and as we go to higher mass mergers, they tend to cause global instabilities funnelling most of the gas in to the centres of the galaxy causing most of the new stars to form in the bulge.

3.2.5 Hot halo

One of the novelty of this study with respect to previous ones, is that, for the first time, we directly include the hot halo gas component in our numerical simulations, in agreement with all models of galaxy formation as well as cosmological hydrodynamical simulations.

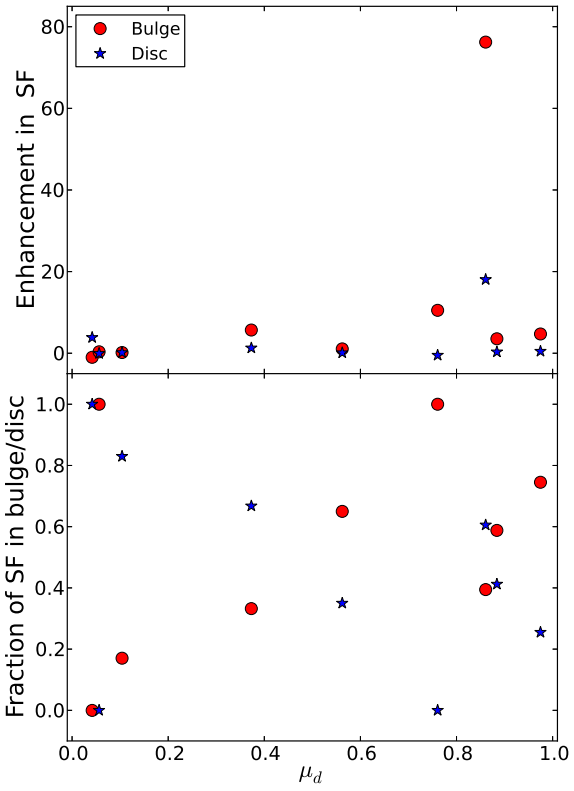

Figure 3.10 Top: The fractional change in star formation in the central bulge (red circles) and the central disc (blue stars). Bottom: The fractional distribution of new stars formed due to merger.

It is then interesting to check which of our results are mostly affected by the inclusion of this new component. In order to address this point we perform a new simulation for Tree 215240 (chosen for its conveniently large merger ratio 0.77) without including the hot halo (both in the models of the primary and the satellite galaxies), but keeping all other components the same (stars, cold gas and dark matter).

Figure 3.11 shows the comparison between the two runs for various properties as a function of time. Without a hot halo (green curves) the primary galaxy becomes completely bulge dominated after the merger, as shown in the upper left panel. The B/T ratio increases from a value of about ≈ 0.8 in the run with the hot halo (blue curves) to ≈ 1.0 when the hot gas reservoir is removed. This is due to the fact that the hot halo replenishes the disc of the galaxy, keeping it gas rich. This in turn helps the gas disc to survive the merger (eg. H09 and Eq. 3.10 of this work). We can also see that the stellar mass transfer to the bulge from the disc remains unaffected and does not depend on the gas fraction of the disc (bottom right panel). The hot halo also provides a continuous supply of cold gas for SF which allows for higher rate of disc regrowth after merger (De Lucia et al., 2011). All together it is clear that the inclusion of an hot halo has several

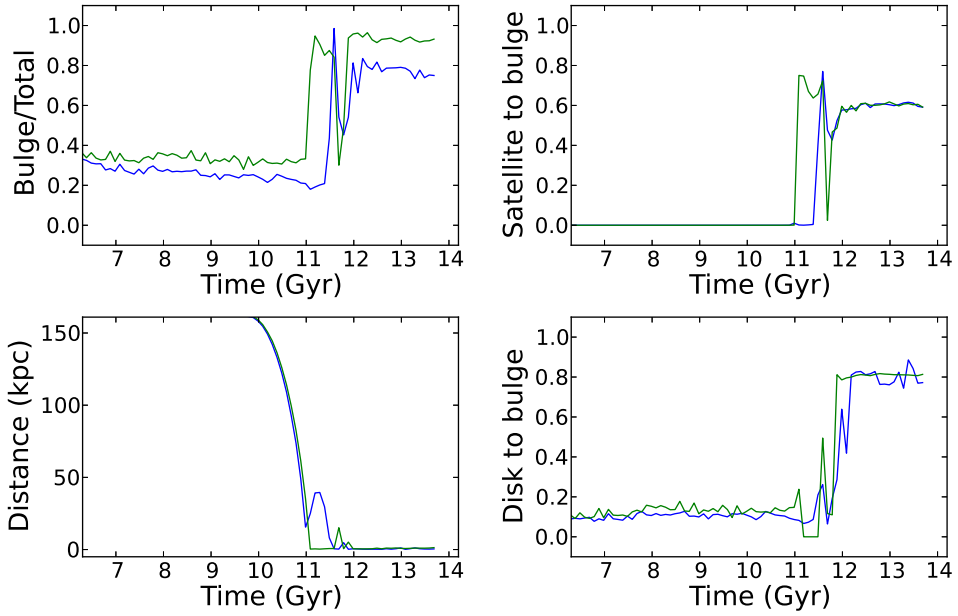

Figure 3.11 Effect of the hot halo on the B/T, fraction of satellite mass given to central bulge and fraction of central disc mass given to bulge. The blue curve indicates a simulation including a hot gaseous halo and the green curves are simulations without the hot halo.

effects on the the final bulge to total ratio, since this hot gas reservoir is crucial for disc regrowth after a merger, and hence must be taken into account in numerical studies of mergers of galaxies (see also Moster et al. 2012).

3.3 Discussion and conclusions

Theoretical models of galaxy formation and evolution usually assume that star formation in galaxies mainly occurs in a disc-like structure as a consequence of the conservation of angular momentum acquired by their host Dark Matter Haloes. In such a scenario spheroidal structures like bulges are created by dissipative mechanisms, like galaxy mergers and secular processes, which remove angular momentum from stars and gas, funnelling them towards the centre of galaxy. Most theoretical models, like SAMs, employ simplified formulae for dealing with these mass transfer processes, in the idealized approximation of a sequence of binary mergers.

In this paper, we analyse in full detail the physics of galaxy mergers, and how mergers change the morphology of galaxies, with particular emphasis on the mass transfer processes between the different components of the merging galaxies. Our approach (first presented and described in Moster et al. 2014) consists in using high resolution smoothed particle hydrodynamic simulations of galaxy mergers where the initial conditions are taken from a combination of cosmological realization of dark matter haloes

merger trees and semi-analytical models. The cosmological merger trees ensure that the orbits and merger timings of DM substructures are cosmologically consistent, while the SAM modelling provides a reasonable guess for the properties of galaxies living in these haloes.

One of the major improvements of this work, with respect to previous similar attempts, lies in the modelling of a hot gaseous halo component: the existence of such component (in addition to the cold phase present in the disc of the galaxy) is predicted by cosmological simulations (e.g. Sommer-Larsen 2006; Johansson et al. 2009; Rasmussen & Ponman 2009; Hansen et al. 2011; Stinson et al. 2012) and observations (e.g. Owen & Warwick 2009, Anderson et al. 2013). Although it does not effect many of the mass transfer channels, the hot gaseous halo does affect the final bulge to total ratio of the galaxy: in fact it is able to replenish the galaxy disc with fresh infalling cold gas, keeping it gas rich and fuelling disc star formation over longer time scales.

We run a series of simulations from $z = 1$ to $z = 0$, including both single and multiple mergers and we quantify the amount of morphological transformation in the model galaxies. We decompose the bulge and disc component of model galaxies using all the six dimensional phase space of position and velocity and considering the mass distribution as a function of the rotational support. This decomposition approach is very robust and allows us to track mass transfers from the satellite to the central bulge, from the initial central disc to the central bulge, the mass of the central disc dispersed into the stellar halo of the galaxy and the B/T evolution.

The main result of this paper is that the outcome of a binary galaxy merger depends both on the merger ratio (both DM - μ and baryonic -μ_b) of the two intervening galaxies and on the details of the relative orbit, and in particular on the ratio η between the orbital angular momentum of the satellite and the angular momentum of a circular orbit with the same energy as the satellite. These two quantities can be combined in the expression $(\mu; \mu_b)/exp(1.9\eta)$ (effective merger ratio), which can be conveniently linked to the relevant mass transfer during a merger.

Mass transfers from the satellite to the bulge. In major mergers and in mergers with low η most of the satellite's mass is deposited into the bulge of the central galaxy. On the other hand, a small satellite galaxy in a high angular momentum orbit deposit most of its baryonic mass into the halo (due to stellar stripping and ram pressure) before its final coalescence with the central object.

Mass transfers from the central disc to the central bulge. The interaction with the incoming satellite cause matter inflows from the central disc to the central bulge. We confirm the early finding of Hopkins et al. 2009 that a gas rich disc is more likely to survive a merger event (even major mergers), even though the strength of this effect changes when the merger orbit is taken into account. For radial satellite orbits, only 50% of the stellar central disc is given to the central bulge even for a 1 : 1 merger.

In addition we also find that a fraction of the central disc mass can also by expelled outwards due to close gravitational encounters, adding up to the diffuse stellar halo population. This mass transfer is usually not considered in SAMs.

Merger driven star formation. During a merger, enhanced star formation rates are expected, if a reservoir of cold gas is available. Our results confirm this picture and we then try to quantify the impact of mergers onto the star formation history of our model galaxies. In most cases, we find an excess of star formation in the central bulges with respect to the isolated runs, but we also find significant enhancement of star formation in the discs of central galaxies. As expected, larger starburst are attributed to major mergers, but the relative contribution of disc starburst to the overall star formation enhancement is larger for minor mergers or high angular momentum orbits due to the triggering of local instabilities in a minor merger event and global instabilities in a major merger event.

We thus propose a series of new fitting formulae able to capture the trends in the relations between the amplitude of mass transfers, the merger ratio and the orbital parameters (the latter two quantities combined into a more general definition of an effective merger ratio). We are well aware of the limitations of our analysis, i.e., the relatively small sample of simulated haloes we consider (mainly due to the computational expensive high resolution simulations needed). More work is of course needed to increase the simulation sample, including more merger trees at different mass scales and widening the range of orbital/merger parameter. This larger sample would then provide us with better constrains on both the mean relations and their scatter, as well as a testbed for extreme cases, such as multiple merger scenarios. Despite the small sample considered in this paper, our results are indicative of a potentially fundamental revision in our understanding of mass flows involved in a galaxy merger. In a forthcoming work (Fontanot et al., in preparation), we plan to include our fitting formulae in state-of-the-art SAMs, to study the implication of our findings on a cosmologically significant galaxy sample, in determining the fraction of bulge and disc dominated galaxies.

Overall our study shows that mergers are not as efficient as previously thought in creating bulge dominated galaxies, and this will possibly alleviate some of the tensions between the observed large fraction of disc galaxies and the hierarchical scenario for structure formation predicted by the Cold Dark Matter model.

Chapter 4

Simulating statistical properties of high redshift galaxies

In addition to mergers, baryonic processes such as gas cooling, star formation, feedback etc., play a major role in regulating the properties of galaxies. These processes are highly non-linear and modelling them accurately is the major challenge for galaxy formation theory. The complexity of these processes make modelling them highly heuristic and requires model adjustments through confrontation with observations.

Fortunately, there are now large catalogues of galactic data available from the local Universe to as far back as $z = 4$. They make it possible to compare galaxy formation models with observations, throughout their evolution. These catalogues include observations that present full spectral energy distributions of the galaxies from 1.4 Ghz radio continuum observations with the *VLA* (Karim et al., 2011), to infrared imaging with *Hubble/WFC3*, *Spitzer/MIPS* and *VLT/HAWK-I* (Kajisawa et al., 2010; Santini et al., 2012). These observations give a complete picture of star formation even when it is dust obscured.

From these observations, one can construct a cosmic star formation history to compare with models (Lilly et al., 1996; Madau et al., 1996; Hopkins, 2004; Wilkins et al., 2008; Bouwens et al., 2012). The shape of the cosmic star formation history has a steep rise from $z = 0$ to $z = 1$ before flattening off and then steadily decreasing from $z = 2$ to higher redshift.

It is also possible to compare the star formation rate (SFR) of individual galaxies with their stellar mass ($M_\star$) determined from infrared photometry. In observations, SFR and $M_\star$ show a tight correlation that is sometimes called the star forming main sequence (Brinchmann et al. 2004; Noeske et al. 2007; Wuyts et al. 2011). The slope of the

The work presented in this Chapter has been published in Kannan et al. (2014a).

relationship does not evolve significantly with redshift, but the normalization increases at higher redshifts (Whitaker et al. 2011; Kajisawa et al. 2010).
Dividing the SFR by $M_\star$ gives the specific star formation rate (sSFR), which provides a test of the star formation efficiency compared to prior star formation. Similar to the rise of the star forming main sequence, the sSFR rises with redshift (Karim et al. 2011; Kajisawa et al. 2010). Above $z = 2$, some observations show that the evolution of the sSFR flattens, though Stark et al. (2013) found that when corrected for nebular line emission, the sSFR continues increasing up to $z = 7$.

4.1 Methods for modelling the statistical properties of galaxies

The primary statistical constraint used for many models is the number density of galaxies as a function of their stellar mass, the galaxy stellar mass function (hereafter, GSMF). The GSMF is a Schecter type function characterized by a power law at low masses and an exponential cutoff. At $z = 0$, the exponential cutoff is at $M_\star \sim 5 \times 10^{10}$ $M_\odot$ (Li & White, 2009). The GSMF evolves as a function of redshift: Santini et al. (2012) find that the low mass slope increases with redshift while Peng et al. (2010) finds that the slope remains constant, but the normalization increases.
Three types of models are commonly used to understand how stars populate galaxies:

- Statistical models: compare statistics of simulations with observations
- Semi-analytic models: populate dark matter haloes with stars based on halo mass, merger history, and single zone physics
- Cosmological simulations: Model a volume of the Universe with hydrodynamics

4.1.1 Statistical Models

The statistical models are based on comparing the GSMF with the dark matter halo mass function and lead to an understanding of how efficiently stars form as a function of dark matter halo mass. A set of cosmological parameters makes explicit predictions about the mass function (Press & Schechter 1974; Sheth et al. 2001; Reed et al. 2005) of dark matter haloes and how those haloes are distributed throughout the Universe. The observed GSMF has a different shape than the dark matter halo mass function found in simulations. The GSMF low mass slope (α) is shallower than the low mass dark matter mass function slope. The $M_\star \sim 5 \times 10^{10}$ $M_\odot$ cutoff is at a lower mass than the dark matter mass function exponential cutoff.
Halo Occupation Models make the reasonable assumption that the distribution of galaxies in the Universe is similar to the distribution of dark matter haloes, modulo some bias

(Peacock & Smith 2000). Halo Occupation Models attempt to match the correlation function statistics of galaxies and dark matter haloes to determine the stellar mass of galaxies that are most likely to be present in a particular dark matter halo. Using Halo Occupation Modelling, one can construct a Conditional Luminosity Function that can be compared with the real luminosity function (Yang et al. 2003; van den Bosch et al. 2007).

Conroy et al. (2006) realized that if one used satellite masses at their time of accretion, then the clustering statistics of mass-ordered dark matter halo samples matches galaxies. This realization lead to the abundance matching technique in which galaxies are placed in dark matter haloes with the same stellar mass ranking as that of the dark matter halo mass rank (Conroy & Wechsler 2009; Moster et al. 2010b; Guo et al. 2010; Behroozi et al. 2010). Such a match leads to the *stellar mass–halo mass* ($M_\star - M_h$) relationship, the key constraint for our model. The $M_\star - M_h$ relation consists of two power laws with a steep slope at low masses and shallow slope at high masses. Stars form most efficiently at the break mass. The star formation efficiency drops quickly to both higher and lower masses. The characteristic mass of the break in the power law is $M_{halo} \sim 10^{12}\mathrm{M}_\odot$ at $z = 0$ (Moster et al., 2013).

The availability of luminosity functions at high redshifts means that we can trace the evolution of the $M_\star - M_h$ relation. Abundance matching indicates that the $M_\star - M_h$ relation evolves surprisingly little (Behroozi et al., 2013a). The star formation efficiency evolves most significantly to higher halo masses at higher redshift from $M_h \sim 10^{12}$ $\mathrm{M}_\odot$ at $z = 0$ to $M_h \sim 10^{12.5}$ $\mathrm{M}_\odot$ at $z = 3$ (Moster et al. 2013; Behroozi et al. 2013b).

The key finding of the abundance matching models is that the star formation peaks earliest in the highest mass galaxies whereas, in the lowest mass galaxies, the SFR increases monotonically with time. This is a reflection of galaxy downsizing (Fontanot et al., 2009). This represents a delay of star formation in low mass haloes and is the most important feature that must be reproduced in models in order to get the evolution of low mass galaxies right.

4.1.2 Semi-Analytic Models

Semi-Analytic Models (SAMs) try to match the GSMF at $z = 0$ using physical prescriptions based on the mass and merger history of dark matter haloes taken from simulations (Kauffmann et al. 1993). SAMs show that supernovae can limit star formation in low mass galaxies (White & Rees, 1978; White & Frenk, 1991; Somerville & Primack, 1999; Benson et al., 2003) and that active galactic nuclei (AGN) can limit star formation in high mass galaxies (e.g. De Lucia et al. 2006; Bower et al. 2006).

While SAMs do well matching the evolution of the high mass luminosity function, they do not match the evolution of low mass galaxies at high redshift (Guo et al. 2011).

Current SAMs include strong stellar feedback to reproduce the GSMF at $z = 0$ (e.g. Guo et al. 2011; Bower et al. 2012), but the low and intermediate mass galaxies build their stellar mass at early times ($z > 2$) following the assembly of the dark matter mass, because the feedback mechnism in these SAMs do not delay star formation in low mass haloes. That means that there is little evolution in the SAM luminosity functions after $z = 2$, in contrast with observations (e.g. Fontanot et al. 2009; Marchesini et al. 2009; Guo et al. 2011). The early star formation means the SAM galaxies have low specific star formation rates at $z < 2$ (e.g. Daddi et al. 2007; Damen et al. 2009) and high values at $z > 3$ (e.g. Bouché et al. 2010;Dutton et al. 2010; Weinmann et al. 2011) although this picture might change at high redshifts due to refinement in the observational estimates of sSFR (Stark et al. 2013). This discrepancy has been looked at in detail by Weinmann et al. (2012), who use the number density evolution of low mass ($9.27 < log(M_\star/\mathrm{M}_\odot) < 9.77$) galaxies as a diagnostic to find that the observed evolution of the number density is not reproduced in any SAMs or simulations. They argue that the simple supernova feedback mechanism used in these models that gets the present day GSMF correct does not decouple star formation from the parent DM halo growth.

4.1.3 Simulations

Hydrodynamical simulations differ from SAMs in that they include self-consistent interaction of dark matter and baryon evolution. Although the efficiency of computational calculations has increased, it is still not possible to resolve many important physical processes, so they must be modelled at the 'sub-grid' level. These processes include gas cooling, star formation and stellar feedback.

Since relatively little is known about star formation and feedback, the models include free parameters, which are constrained by observations. Star formation model parameters are constrained using local observations of the Kennicut-Schmidt gas density–star formation density relation (Springel & Hernquist, 2003; Stinson et al., 2006; Schaye & Dalla Vecchia, 2008). The energy feedback from stars is modelled either by adding velocity to gas, called *kinetic feedback*, or adding thermal energy as *thermal feedback*. These models have been constrained based on observations (Springel & Hernquist, 2003; Oppenheimer & Davé, 2006; Dalla Vecchia & Schaye, 2008; Crain et al., 2009; McCarthy et al., 2012). The model used in this work instead constrains stellar feedback to match the evolution of $M_\star - M_h$ relation.

There has been a lot of research on the optimal velocity for winds driven using kinetic feedback. The original models used a fixed wind velocity (Springel & Hernquist 2003; Crain et al. 2009; McCarthy et al. 2012), however, they had difficulties reproducing the GSMF at $z = 0$. Observations of metal absorption lines in outflows show that wind

velocities are not constant, but are correlated with star formation rate, $v_w \approx SFR^{0.35,}$ at $z = 0$ (Martin, 2005) and $v_w \approx SFR^{0.3}$ at $z \approx 1.4$ (Weiner et al., 2009). These observations motivated using momentum conserving wind models in which mass loading depends on the mass of the host galaxy such that $\dot{M}_{wind}/\dot{M}_\star \propto V_{circ}^{-1}$ (Oppenheimer & Davé 2006; Oppenheimer & Davé 2008; Davé et al. 2011a,b). Momentum conserving winds successfully reproduce the GSMF and many other observed galaxy properties at $z = 0$ (Oppenheimer et al. 2010;Davé et al. 2011a,b ; Puchwein & Springel 2013), but has similar shortcomings with the low mass end of the luminosity function as the SAMs at high redshift. Weinmann et al. (2012) conclude that the current models of stellar feedback (in both SAMs and simulations) are unlikely to decouple the galaxy and DM halo growth due to its fundamental dependence on host halo mass and accretion history. An alternative to the momentum driven wind model is the energy conserving approximation for driving outflows from galaxies in which the mass loading factor scales as $\dot{M}_{wind}/\dot{M}_\star \propto V_{circ}^{-2}$. Puchwein & Springel (2013) find that using this approximation of a stronger scaling of mass loading with galaxy size results in a shallower slope of the GSMF at $z = 0$. The energy driven wind model also suppresses star formation at high redshift, reducing the cosmic star formation rate density to observed levels and shifting its peak to $z \sim 2.5$. This model is also successful in reproducing the GSMF at $z = 1$ and $z = 2$ reasonably well.

In thermal stellar feedback, stars heat the surrounding gas particles adiabatically, which creates pressure that can push gas out of galaxies (Gerritsen & Icke 1997; Thacker & Couchman 2000; Kawata & Gibson 2003; Stinson et al. 2006). SNe energy can only efficiently drive outflows if the Sedov-Taylor phase of gas expansion is resolved. Such resolution is infeasible even with modern computer hardware, so two techniques have been employed to model this sub-grid phsyics. Stinson et al. (2006) delay cooling within the blast region that a supernova would create. Dalla Vecchia & Schaye (2012) integrate all the supernova energy that a stellar population creates and put it in a single gas particle. This raises the temperature to lengthen the cooling time enough so that the hot gas particle has a dynamical effect.

Simulations using thermal feedback have so far focused on disc structure using high resolution zoom in simulations (Governato et al. 2010; Brook et al. 2011; Sawala et al. 2011; Guedes et al. 2011; Agertz et al. 2011). Some recent simulations of a handful of galaxies have indicated that adiabatic feedback produces galaxies that follow $M_\star - M_h$ below $M_{\rm halo} < 10^{12}{\rm M}_\odot$ (Brook et al. 2012; Munshi et al. 2013).

In most models of stellar feedback, only feedback from supernovae is considered, but Murray et al. (2010) recognized the amount stars can disrupt molecular clouds before any stars explode as supernovae. Hopkins et al. (2011) and Agertz et al. (2013) implemented early stellar feedback schemes that rely on IR radiation pressure and tested them on isolated galaxy simulations. Lopez et al. (2011) and Pellegrini et al. (2011) found that

when they mapped the pressure in different phases of the gas in the 30 Doradus region of the LMC, UV photoheating provides more pressure than IR radiation pressure.

Stinson et al. (2013b) assume that photo-heating from massive stars is thermalised by the time it reaches the spatial scales resolved in cosmological simulations. So, they inject thermal energy equal to the fraction of the bolometric luminosity emitted in the UV in the time between the formation of the star and the first supernova explosion. This early stellar feedback limits star formation to the amount prescribed by the $M_\star - M_h$ relationship and delays star formation in an $L_\star$ galaxy, so that the galaxy follows the evolution of the $M_\star$ - M_h relationship. This is a major improvement over previous galaxy formation models, as the delayed star formation means that star formation is decoupled from DM halo mass growth. Some side-effects of using early stellar feedback include transforming DM cusps to cores in galaxies up to $L_\star$ masses (Macciò et al., 2012) and populating the circum-galactic medium with hot metal enriched gas, matching OVI observations (Stinson et al., 2013b).

In this work we explore how the early stellar feedback model (ESF), described in Stinson et al. (2013b), affects the global properties of galaxies on a large scale. To study this we simulate a large volume of the Universe, 114 Mpc on a side, as part of the Making Galaxies in a Cosmological Context (MaGICC) project. This simulation tests the effectiveness of the model at low resolution across a wide range of galaxy masses, environments and merger histories. We compare the properties of the galaxies in our simulations with observed statistical properties of high redshift galaxies like the GSMF, stellar to halo mass relationship, star formation rate, and the number density evolution of low mass galaxies through cosmic time. In §4.2 we briefly outline the star formation and stellar feedback mechanisms used in our simulations, in §4.3 we present our results and compare them to the current observational estimates. In §4.4 we test the convergence of our numerical code and also discuss the roles of ESF in getting the properties of high redshift galaxies right. In §4.5 we summarize our results and discuss future challenges.

4.2 Simulation Method

We simulate a cosmological volume, 114 Mpc on a side, from $z = 99$ to $z = 2$. It is created using WMAP7 initial conditions with (h, $\Omega_{\rm M}$, Ω_Λ, $\Omega_{\rm b}$, σ_8) = (0.702, 0.2748, 0.7252, 0.0458, 0.816) (Larson et al., 2011; Komatsu et al., 2011). The simulation includes 512^3 dark matter and 512^3 gas particles. The dark matter particle has mass of $3.4 \times 10^8 {\rm M}_\odot$ and a softening length of ~ 3.7 kpc. The initial gas particle mass is $6.9 \times 10^7 {\rm M}_\odot$ and the initial star particle mass is $1.3 \times 10^7 {\rm M}_\odot$. Gas and star particles have a softening length of ~ 2.17 kpc. §4.4 describes lower resolution simulations that were used to test the resolution dependence of our model.

All the simulations use the smoothed particle hydrodynamics (SPH) code GASOLINE (described in Wadsley et al. 2004; also see Chapter 1). The smoothing length is calculated using 32 nearest neighbours. Details of the physics used in the MaGICC project are detailed in Stinson et al. (2013b). Briefly, stars are formed from gas cooler than $T = 10^4$ K, and denser than 8.7 cm^{-3} according to the Kennicutt Schmidt Law as described in Stinson et al. (2013b) with the star formation efficiency parameter $c_\star$=0.1. The cooling used in this work is described in detail in Shen et al. (2010) (see Chapter 5 for a thorough description of the cooling calculation). It was calculated using CLOUDY (version 07.02; Ferland et al. 1998) including photoionization and heating from the Haardt & Madau (unpublished) ultraviolet (UV) background, Compton cooling, and hydrogen, helium and metal cooling from 10 to 10^9 K.

The star particles are massive enough to represent an entire stellar population consisting of stars with masses given by the Chabrier (2003) initial mass function. 20% of these have masses greater than 8 M$_\odot$ and explode as Type II supernovae from 4 until 35 Myr after the stellar population forms according to the Padova stellar lifetimes (Alongi et al., 1993; Bressan et al., 1993). Each supernova ejects $E_{SN} = 10^{51}$ ergs of purely thermal energy into the surrounding gas ($\sim$ 1 kpc at the resolution of our simulations). The supernova energy would be radiated away before it had any dynamical impact because of two reasons, the high density of the star forming gas and feedback energy spread over larger gas mass sue to resolution limits. Thus, the supernova feedback relies on delaying the cooling based on the sub-grid approximation of a blast wave as described in Stinson et al. (2006).

The supernovae feedback does not start until 3.5 Myr after the first massive star forms. However, nearby molecular clouds show evidence of being blown apart *before* any SNII exploded (Murray et al., 2011). Lopez et al. (2011) and Pellegrini et al. (2011) found that UV photoheating is the dominant feedback mechanism in early phases of star formation by mapping out the pressure in different phases of the gas. In simulations in the MaGICC project, like those here, 10% the UV luminosity of the stars is injected into the surrounding gas over this 3.5 Myr period without disabling the cooling, at the rate of 4.45×10^{48} erg/Myr/M$_\odot$. Stinson et al. (2013b) showed that this energy limits star formation to the amount prescribed by the $M_\star - M_h$ relationship at all redshifts. The current work is our attempt explore how this star formation and feedback prescription works at lower resolutions over a wide range of galaxy masses.

4.2.1 Halo identification

For each snapshot, we find all the virialised haloes within the high resolution region using a Spherical Overdensity (SO) algorithm. Candidate groups with a minimum of $N_f = 100$ particles are selected using a FoF algorithm with linking length $\phi = 0.2d \approx$

22 kpc (d is the mean inter-particle separation). We then: (i) find the point C where the gravitational potential is a minimum; (ii) determine the radius $\bar{r}$ of a sphere centred on C, where the density contrast is $\Delta_{\rm vir}$, with respect to the critical density of the Universe. Using all particles in the corresponding sphere of radius $\bar{r}$, we iterate the above procedure until we converge onto a stable particle set. This stable particle set is then defined as a 'halo'. A galaxy is all stars within the particle set defined as a 'halo'. This does not affect the definition of stellar mass in low mass galaxies, the focus of this work, because their substructures contain very little amount of stars. We use a constant virial density contrast $\Delta_{\rm vir} = 200$, in order to be consistent with Moster et al. (2013). We include in the halo catalogue all the haloes with more than 100 particles (see Macciò et al. 2007, 2008 for further details on our halo finding procedure).

4.3 Results

We compare the simulated galaxy population in a 114^3 Mpc^3 volume with a set of basic properties derived from the most recent observational estimates. These include the galaxy stellar mass function (GSMF), stellar mass–halo mass ($M_\star - M_h$) relationship, cosmic star formation history (SFH), star forming main sequence, and specific star formation rates (sSFRs). Individual galaxies have been shown to match observations well (Brook et al., 2012; Stinson et al., 2013b), so the volume provides an opportunity to test the accuracy and effectiveness of this feedback model at low resolution and high redshift. All the observational estimates of stellar masses and SFRs, that our results have been matched to, have been corrected to a Chabrier (2003) IMF. The results presented in this work have all been presented in co-moving units where ever applicable.

4.3.1 Stellar - halo mass ($M_\star - M_h$) relation

Figure 4.1 shows the $M_\star - M_h$ relation for all the galaxies in the simulated volume (black points) that contain a minimum of 20 star particles, or a stellar mass of $\sim 3\times10^8$M$_\odot$. The galaxies trace (red solid line) the slope of the $M_\star - M_h$ (green line) up to $M_{halo} = 10^{12}$M$_\odot$ at all redshifts where it has been examined. The scatter of the simulated galaxies, quantified by the 10 and 90 percentile limits of the distribution (red dotted lines), also matches the variation in the relation as obtained by Moster et al. (2013) (grey shaded area). The agreement points to the fact that the stellar feedback effectively regulates star formation to produce the right amount of stellar mass in a given halo mass at all times.

Above a halo mass of 10^{12} M$_\odot$, abundance matching (green dotted line) shows a decrease in star formation efficiency (SFE). This is not reproduced in the simulation. The star formation efficiency actually increases at $M_{halo} \sim 4\times10^{12}M_\odot$, before decreasing slightly as represented by the slightly shallower slope of the simulation points. The reduced

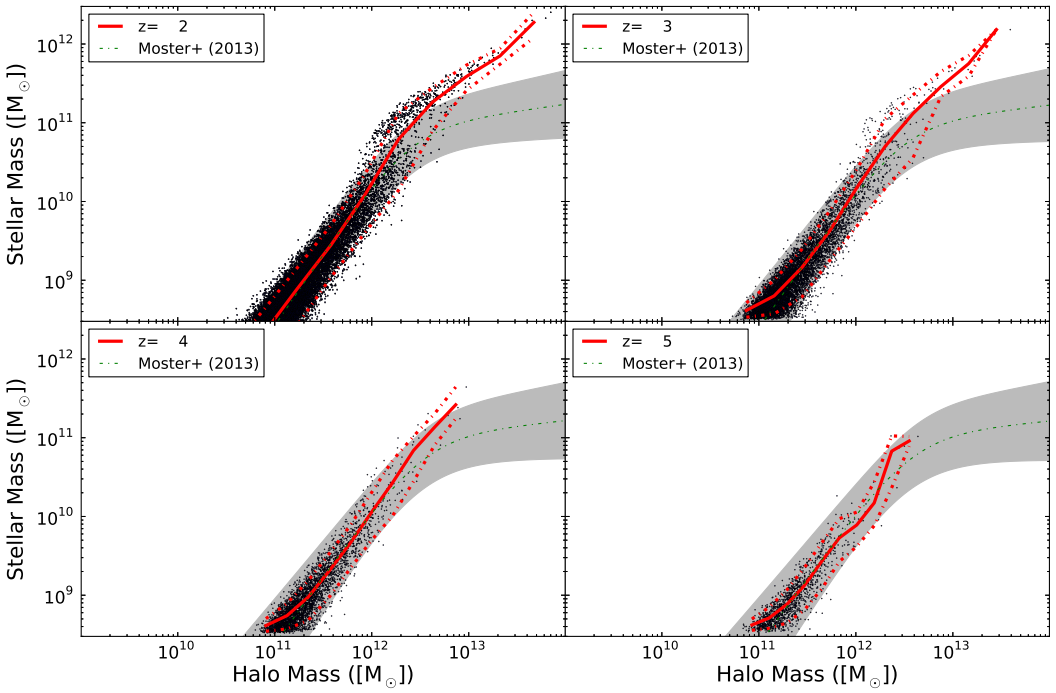

Figure 4.1 $M_\star - M_h$ relation at different redshifts. The black points are simulated galaxies, with the red solid line tracing the mean of the distribution and the red dotted lines indicate the 10 and 90 percentile limits of the distribution. The green dotted line is the Moster et al. (2013) relation derived from abundance matching techniques and the grey shaded area is the scatter derived for the relation. Our simulated galaxies match the relation below $M_{halo} < 10^{12}\mathrm{M}_\odot$, but star formation is too efficient in high mass haloes.

SFE is due to the reduced gas accretion because of the high virial gas temperature of the halo. However, this slight decrease in SFE does not reduce the star formation in these high mass haloes to the extent observed. The implemented stellar feedback model is insufficient in these high mass haloes. Some other quenching mechanism is required such as feedback from a central super-massive black hole (AGN feedback, e.g. Fanidakis et al. 2011; Springel et al. 2005a).

4.3.2 The galaxy stellar mass function (GSMF)

The GSMF measures the number of galaxies of a certain stellar mass in a given volume of the Universe. The era of deep, high redshift surveys has provided detailed GSMFs out to $z = 3$. We compare our simulation results to Santini et al. (2012), who use deep *WFC3* near-IR data complemented by deep *Hawk-I* K_S band data to derive accurate stellar massees in a ~ 33 arcmin^2 area located in the GOODS-South field, to study the low-mass end of the GSMF. The observed GSMFs are presented for various redshift ranges.

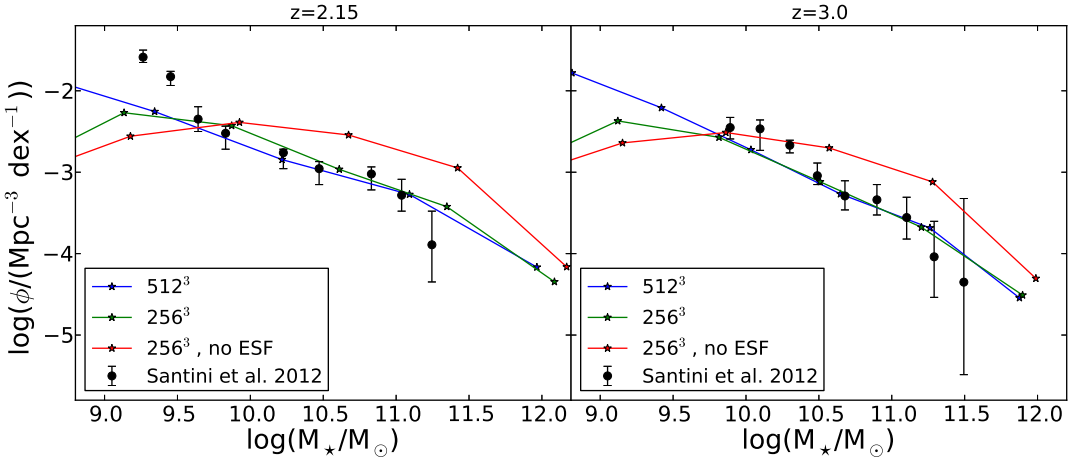

Figure 4.2 Galaxy stellar mass function at $z \sim 2$ and $z = 3$ compared to observational data taken from Santini et al. (2012) for three different simulations. The fiducial simulation with 512^3 particles is shown in blue, the corresponding low resolution run (256^3) is shown in green, while the low resolution simulation without ESF is coloured red.

To compare with them, we use the simulated GSMF from the middle of the observed redshift range. Figure 4.2 shows that the simulated galaxies from the fiducial run (blue line) trace the intermediate mass ($10^{9.5} < \mathrm{M}_\star/\mathrm{M}_\odot < 10^{11}$) slope of the observed GSMF (red points) very well. There is a slight discrepancy at $\mathrm{M}_\star < 10^{9.5}\mathrm{M}_\odot$ at $z = 2.15$. This discrepancy might arise due to the the difficulty in determining the properties of low mass galaxies at such large distances or due to cosmic variance, as their data set has a small sky coverage. The feedback model makes the slope of the GSMF as shallow as the observed value, which is non-trivial and is a major improvement over previous attempts to match the GSMF at high redshift (e.g. Guo et al. 2011). A small discrepancy remains, as the simulated number density of high mass galaxies continues to decrease at the same rate, whereas the observations show an exponential cutoff. This again indicates that stellar feedback is insufficient to limit star formation in these high mass haloes. The green and red curves are control test runs, which will be discussed in §4.4.

4.3.3 Number density evolution of low mass galaxies

Weinmann et al. (2012) used the number density evolution of low mass ($9.27 < \log(M_\star/\mathrm{M}_\odot) < 9.77$) galaxies to show that semi-analytic models or cosmological hydrodynamic simulations do not correctly model low mass galaxies. They argue that the simple supernova feedback mechanism changes the stellar mass at $z = 0$, but renormalizes the star formation history and thus does not decouple star formation from DM accretion. Stinson et al. (2013b) showed for a single high resolution L* simulation that early stellar feedback can break the coupling of star formation to dark matter accretion. Figure 4.3 shows the number density evolution of low mass galaxies at high redshifts in our simulation

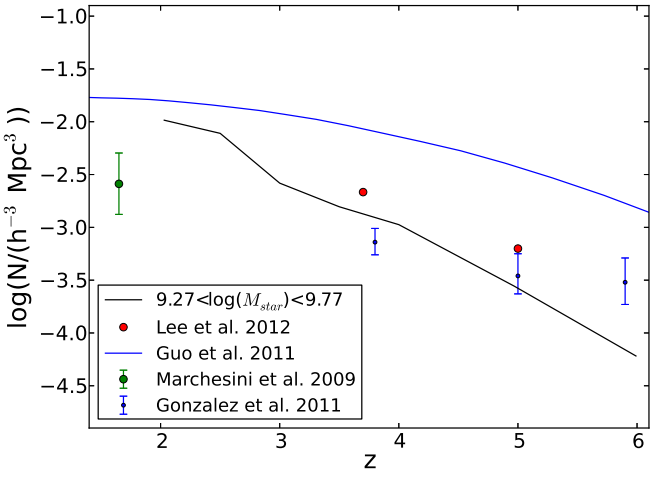

Figure 4.3 Number density of low mass galaxies as a function of redshift (black line) compared to various observational estimates (points) and a semi analytic model (blue line) as described in Guo et al. (2011). Our simulation results have a steeper slope and are a better fit to the observational data.

volume compared to observations taken from Figure 1 of Weinmann et al. (2012), as well with the SAM described in Guo et al. (2011). The simulation matches the observational results much better and lies well below the values obtained by the SAM. The difference between the observations of González et al. 2010 (blue points) and Lee et al. 2012 (red points) is larger than the González et al. 2010 error bars. The simulated curve falls in the middle of these observations in contrast with the SAM that lies an order of magnitude above the observations. We note that the slope obtained from our model is still slightly steeper than observed, indicating that the simulation is building low mass galaxies faster than observed.

4.3.4 Star formation History

We can also compare our simulation with the total number of stars formed in the Universe as a function of time. Figure 4.4 shows how the cosmic star formation rate evolves as a function of redshift ('Lilly-Madau plot') in our simulated volume. The observed points used for comparison are taken from Moster et al. (2013) and include star formation estimates derived from rest frame UV (Salim et al. 2007; van der Burg et al. 2010; Robotham & Driver 2011; Bouwens et al. 2011; Cucciati et al. 2012), Hα (Ly et al. 2011), combined UV and IR (Zheng et al. 2007; Kajisawa et al. 2010), FIR (Rujopakarn et al. 2010) and radio observations (Smolčić et al. 2009; Dunne et al. 2009; Karim et al. 2011). The total SFR density (black line) passes through the observations from $z = 2 - 5$.
The total SFH can be divided into separate lines based on the stellar mass of the halo at $z = 2$ in which the stars are formed. The lowest mass galaxies ($9.5 < \log(M_\star/\mathrm{M}_\odot) <$

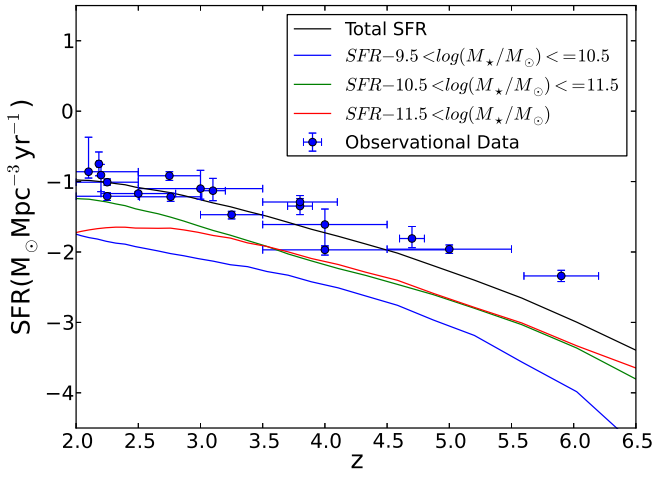

Figure 4.4 The evolution of the star formation rate density. The blue points are a compilation of star formation rate density estimates taken from Moster et al. (2013). The black solid line is our result for all galaxies in our volume. The coloured curves show the star formation histories of galaxies in a certain mass range. The mass of galaxies quoted is calculated at $z = 2$. The blue line is the SFR density for low mass galaxies ($9.5 < \log(M_\star/\mathrm{M}_\odot) < 10.5$), the green for intermediate ($10.5 < \log(M_\star/\mathrm{M}_\odot) < 11.5$) mass galaxies and the red line for high mass ($\log(M_\star/\mathrm{M}_\odot) > 11.5$) galaxies. There is a clear trend of decreasing star formation at $z \leq 3.5$ in the highest mass galaxies.

10.5) contribute little to the overall SFR density, while the the intermediate ($10.5 < \log(M_\star/\mathrm{M}_\odot) < 11.5$) and high mass ($\log(M_\star/\mathrm{M}_\odot) > 11.5$) contribute equally up to $z = 3$. Below this redshift, the SFR flattens out in the highest mass galaxies. This flattening is not sufficient to explain the quenching of high mass galaxies as shown by the failure of the simulated $M_\star - M_h$ and GSMF relations at the high mass end. We note that our match of the star formation history is not greatly affected by the excess star formation in galaxies with ($\log(M_\star/\mathrm{M}_\odot) > 11.5$) because even though the galaxies in that mass range form too many stars at $z \leq 3.5$, they are not the dominant population of galaxies at those redshifts.

4.3.5 Star forming main sequence

Observations show that star-forming galaxies have a tight correlation between their SFR and $M_\star$ (e.g., Elbaz et al. 2007; Pannella et al. 2009; Wuyts et al. 2011; Whitaker et al. 2012). This correlation has been called the "star forming main sequence."

We compare the SFRs of our simulated galaxies with observational estimates by Kajisawa et al. (2010) and Whitaker et al. (2012). Kajisawa et al. (2010) studied SFR as a function of $M_\star$ for galaxies at $0.5 < z < 3.5$ in the GOODS-North field, using the K-selected sample from *Subaru*-MOIRCS. They determined SFRs from rest-frame,

dust-corrected UV luminosity and the *Spitzer*-MIPS 24 μm flux. The depth of their data allowed them to constrain the slope of the SFR-M$_\star$ relation down to $M_\star = 10^{9.5}$M$_\odot$ at $z \sim 3$. The median SFR as a function of stellar mass (green curve) from their sample of galaxies is plotted in top panels Fig. 4.5 at $z = 2$ & 3. The slope of their relation is close to unity for low mass galaxies at these high redshifts. Our simulated galaxies match these observations well at $z = 3$, but have nearly two times less star formation at $z = 2$. This discrepancy at $z = 2$ presents a challenge for all hydrodynamic simulations and SAMs (Weinmann et al., 2011). Davé (2008) suggested that an evolving stellar IMF is required to reduce the discrepancy in this relation out to $z = 2$.

Whitaker et al. (2012) measure star formation rates using the NEWFIRM Medium-Band Survey from MIPS 24 μm fluxes. At $z > 2$ their detection limit is $\log(M_\star/\mathrm{M}_\odot) > 10.7$. For these galaxies, they find a shallower, sub-linear, slope for their star forming main sequence, $SFR \propto M^{0.44}$, with a constant scatter of 0.34 dex. Above their detection limit, our simulated galaxies (black points) lie below the observations (red line) as seen in the top left panel of Fig. 4.5.

Galaxies above a stellar mass of 10^{11}M$_\star$ show a slight reduction in star formation rate from the trend at lower masses. This reduction is likely the result of the high temperatures of the gas haloes surrounding these galaxies, which has a long cooling time, so gas accretion onto the disc is slightly reduced. However, observations of such galaxies show a much more dramatic decrease in star formation that is not captured in these simulations.

4.3.6 Specific star formation rate evolution

Another common way to compare star formation rates with galaxy stellar masses is the specific star formation rate (sSFR), which gives the amount of star formation in haloes per unit stellar mass of material. As one would expect from the star forming main sequence, the bottom panels of Fig. 4.5 show that the simulated galaxies (black points) match the Kajisawa et al. (2010) (green curve) observed sSFRs at $z = 3$ but have ~ 2 times lower sSFR at $z = 2$. We also compare our simulated results with 1.4 GHz radio continuum observations from Karim et al. (2011) of star formation in galaxies in the 2 deg^2 COSMOS field. The simulated galaxies in our volume (black points) are in good agreement above $\log(M_\star/\mathrm{M}_\odot) > 10.7$, but are $2-3$ times lower below this mass range at both $z = 2$ & 3.

Karim et al. (2011), like other authors before them (Stark et al., 2009; González et al., 2010), found that sSFR increases for galaxies in a given stellar mass range from $z = 0$ to $z \sim 2$, but then does not evolve much from $z = 2$ to $z \sim 7$. Weinmann et al. (2011) shows that such observations are contradictory with most models in which higher gas accretion rates at higher redshift and lower galaxy stellar masses translate into larger sSFR in galaxies within a fixed stellar mass range.

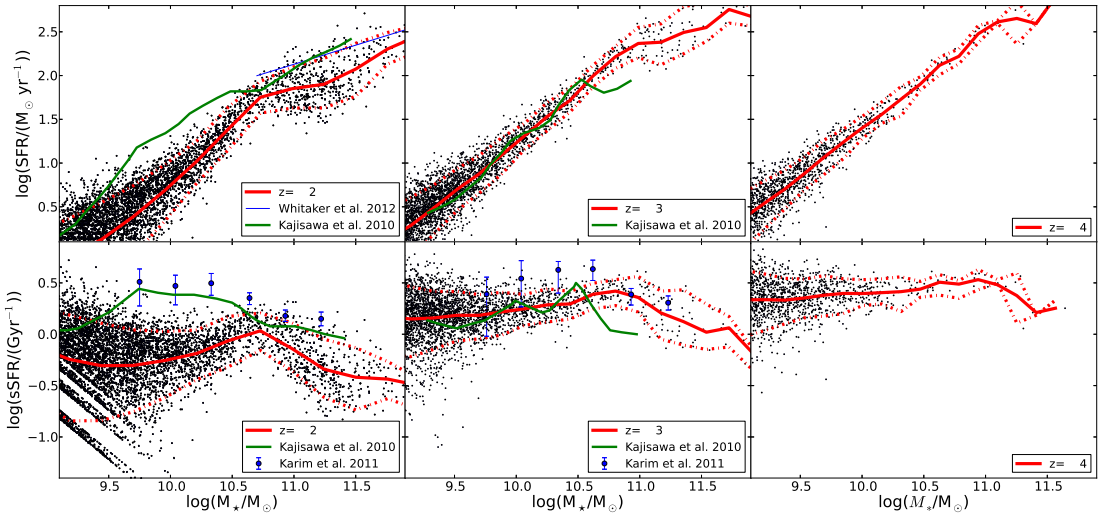

Figure 4.5 Top panels: The star forming main sequence (black points) at different redshifts. The $z = 2$ result for galaxies with $\log(M_\star/\mathrm{M}_\odot) > 10.7$ is matched to the observational results of Whitaker et al. (2012) (Red line). The slope of the main sequence is much steeper at lower masses. This matches well with the observational estimates derived by Kajisawa et al. (2010) at $z = 2\&3$ (green curve). Bottom panels: The simulated sSFR (black points) matched to observational results matched from Karim et al. (2011) (Red points) andKajisawa et al. (2010) (green curve). The simulated sSFR lies below the observed values for low mass galaxies at $z = 2$ by a factor of ~ 2, but matches very well at $z = 3$.

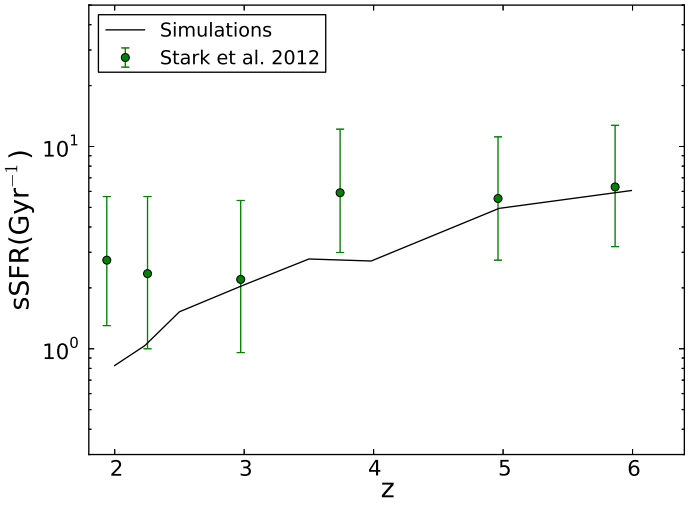

Figure 4.6 The evolution of the specific star formation rate for sample galaxies which have stellar masses within a narrow range around $\sim 5 \times 10^9 \mathrm{M}_\odot$ (blackline). We compare the simulations with the observational estimates of Stark et al. (2013). The evolution of sSFR matches well at $z \leq 3$, but is below the observed value at lower redshifts.

Stark et al. (2013) re-examined their data and found that their *Spitzer*-IRAC photometry was contaminated by nebular emission. They use the photometric excesses in the contaminated [3.6] filter to estimate the equivalent width distribution of Hα emission at $3.8 < z < 5.0$. The corrected sSFRs increase from $z = 4$ to $z = 7$ by a factor of ~ 5 similar to model predictions. Figure 4.6 shows the evolution of the sSFR in simulated galaxies (black line) within a narrow stellar mass range around $\sim 5 \times 10^9 \mathrm{M}_\odot$. The simulation values are consistent with the corrected Stark et al. (2013) values (green points) for $z > 3$. However at $z < 3$ our simulation results are below the observed relation.
Many other authors find also find lower than observed sSFRs in their models at $z < 3$ (Davé 2008; Weinmann et al. 2012). The higher observed sSFRs again indicates delayed star formation in low mass galaxies. Although our model does a better job of delaying the star formation at early times than most SAMs and hydrodynamic simulations, below $z = 3$ the simulated haloes may still be forming too few stars. This suggests the importance of some other physical mechanism, not modelled in our simulation, like the dependence of the star formation on gas metallicity (Krumholz et al., 2011; Krumholz & Dekel, 2012), that could further delay star formation at earlier times and increase the sSFR of these galaxies at $z = 2$.

4.3.7 Results at $z = 0$

Galaxies in the local Universe are the easiest to observe and compare with our model. Unfortunately, it is too computationally demanding to simulate the full cosmological volume to $z = 0$. So, we select a 16 h^{-1} Mpc sub-volume from the fiducial simulation at $z = 2$. The region was selected to limit the number of high mass haloes present in the region. The lack of massive haloes reduces the computational cost but also reduces the density of the region by $\sim 10\%$ compared to the mean density for full volume. This kind of volume selection also impairs our ability to compare the volume weighted properties of galaxies like the GSMF. On the other hand, the individual properties of galaxies like the stellar mass compared to the halo mass of the galaxy ($M_\star - M_h$ relation) and the star formation rate compared to their stellar mass (star formation main sequence) are expected to remain similar irrespective of the surrounding density field. Sheth & Tormen (2004) showed that halo formation weakly depends on the surrounding density field. So, only the $M_\star - M_h$ relation and the star formation main sequence obtained from the selected region are shown at $z = 0$ in Figs. 4.7 and 4.8.
We include gas particles only inside the 16 h^{-1} Mpc sub-volume. Outside this region the particles are re-binned to a lower resolution in order to save computing time. The simulation was then restarted from $z = 2$ and allowed to continue to $z = 0$, with all the other parameters unchanged from the fiducial run. This region contained enough galaxies for us to make a statistical comparison at $z = 0$ with observations.

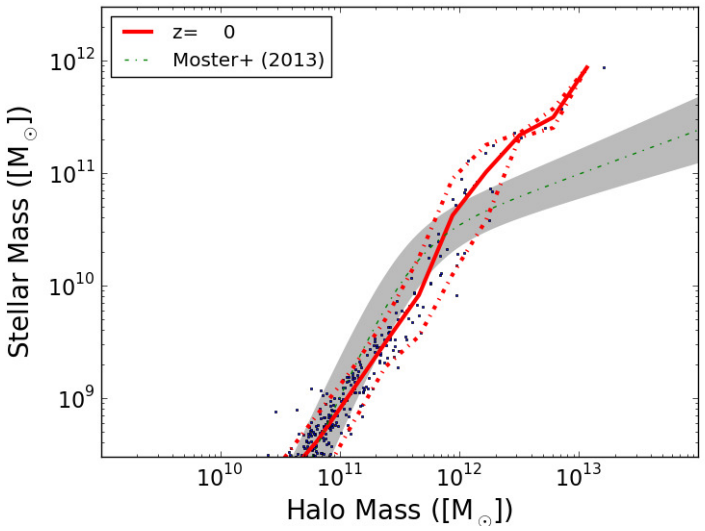

Figure 4.7 The stellar-halo mass relation for galaxies in a 16 h^{-1} Mpc at $z = 0$. Galaxies around $M_{halo} = 10^{11} M_{\odot}$ have about half the expected stellar mass. Galaxies with $M_{halo} > 10^{12} M_{\odot}$ continue to exhibit the overcooling problem like they did at high redshift. The solid red line is the median of the simulation points, while the dotted lies show the 10 and 90 percentile limits for those bins.

Fig. 4.7 shows the $(M_\star - M_h)$ relation for the galaxies in the selected cube at $z = 0$. The black points are simulated galaxies, the red solid line traces the mean of the distribution and the red dotted lines indicate the 10 and 90 percent confidence intervals of the distribution. The green dotted line is the Moster et al. (2013) relation derived from abundance matching techniques and the grey shaded area is the scatter derived for the relation. The simulation still provides a fair match to the observations at $M_h \sim 10^{11} M_{\odot}$, though the galaxies at $z = 0$ have half the stellar mass of the observed galaxies. The over-cooling problem also remains in higher mass galaxies ($M_h > 10^{12} M_{\odot}$).

As mentioned in §4.1.3, previous studies using momentum driven winds SNe feedback recipes (e.g Oppenheimer et al. 2010, Crain et al. 2009) also tend to overproduce the stellar mass of massive galaxies and slightly under predict the stellar mass at the knee of the stellar mass function. Energy driven variable wind models seem to be capable of reproducing the low-z GSMF (for e.g. see Puchwein & Springel 2013). Our model is more successful in reproducing the galaxy stellar mass function at high redshift ($z > 2$) in the low mass galaxy regime, while the previous studies largely overpredict the number of low mass galaxies at these high redshifts (as shown in Fig. 1 of Weinmann et al. 2012) and the differences between observations and our model at $z = 0$ is pretty small and comparable to previous works.

Observations of the star forming main sequence are also more complete at $z = 0$. Fig. 4.8 shows how the simulated galaxies compare to those observations (grey contours from

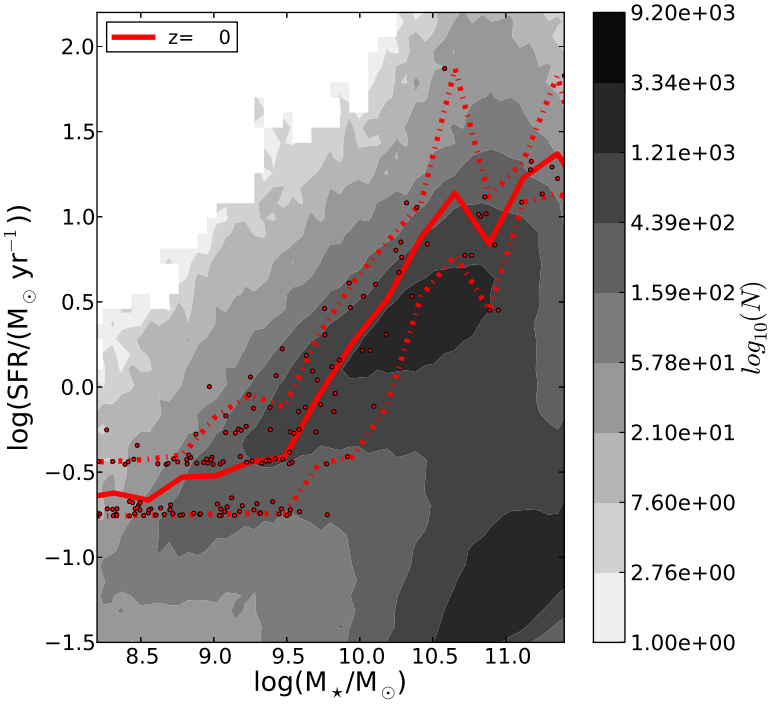

Figure 4.8 The simulated star forming main sequence at $z = 0$. Individual galaxies are the red points while the solid red line represents the median of those galaxies. The dot-dashed lines represent the 10 and 90 percentile limits of the galaxy distribution. The simulations are compared with 894k galaxies from SDSS as in Brinchmann et al. (2004) plotted as the grey contours.

Brinchmann et al. 2004). The median star formation rates of the simulated galaxies are ~ 0.5 dex higher than the locus of the observed star forming main sequence, but are still within the observed range of star formation rates. This is a change from high redshift where the simulated galaxies had systematically lower star formation rates than observations.

No simulated galaxies populate the quiescent–high stellar mass corner of the plot. Even at $z = 0$, the simulation cannot produce red, dead galaxies most likely due to the lack of AGN feedback.

While the simulations have trouble at high masses, this sample of galaxies at $z = 0$ suggests that the simulations model the statistical properties of low mass galaxies well throughout the history of the Universe.

4.4 Effect of resolution and early stellar feedback

To test the effect of resolution and early stellar feedback, we simulated the fiducial volume at a lower resolution containing 256^3 2.76×10^9 $M_\odot$ dark matter and 256^3

5.5×10^8 M$_\odot$ gas particles. Star particles form with masses of 1.83×10^8 M$_\odot$. The dark matter particles use a softening length of ~ 3.7 kpc, while the gas and star particles use a softening length of ~ 2.17 kpc. All the other simulation parameters are the same as used in the fiducial run. The low resolution simulation was performed with two different feedback models, one with SNe feedback only, and the other adding early stellar feedback to the SNe feedback.

Fig. 4.2 shows the GSMF's for these simulations (green and red lines) in addition to the fiducial run (blue curve). The low resolution volume with the same physics as the fiducial run (green curve) matches the fiducial run and observations for M$_\star > 10^{9.5}$M$_\odot$. The simulation without early stellar feedback has too many galaxies with M$_\star > 10^{10}$M$_\odot$. The decrease in the number of M$_\star > 10^{9.5}$M$_\odot$ in the low resolution simulations is caused by the resolution limit. These galaxies consist of only a couple star particles, so star formation is not well sampled and the results cannot be trusted. Fig. 4.2 shows that our model is fairly well converged as well as the need for early stellar feedback to produce realistic galaxies.

4.5 Discussion and Conclusions

We examine the effect of early stellar feedback used in the Making Galaxies in a Cosmological Context (MaGICC) project on a broad sample of galaxies in a cosmological volume of 114^3 Mpc^3. The stellar feedback used is exactly the same as that used for a high resolution $L_\star$ galaxy (Stinson et al., 2013b). We compare the simulated galaxies with the observed $M_\star - M_h$ relation, the galaxy stellar mass function, the cosmic star formation history, the star forming main sequence and the specific star formation rate. The simulated galaxies do a good job matching each observation to $z = 2$, the time when previous models have most deviated from observations. Our use of early stellar feedback is the key difference between our simulation and ones run previously. The way that it delays star formation in $M_h < 10^{12}$M$_\odot$ galaxies allows the simulations to match many observed statistical properties of high redshift galaxies.

At $z \geq 2$, the simulated galaxies not only follow the $M_\star - M_h$ for $M_h < 10^{12}$M$_\odot$ at all the redshifts examined but also match the scatter in the relation. Correspondingly, the simulated galaxies match the shallow slope at the low mass end of the galaxy stellar mass function. The slope of the GSMF relationship was not a constraint for the simulation, but is a natural by product of the stellar feedback recipe used. It is a major improvement over previous attempts to match the GSMF at high redshift. The early stellar feedback decouples the growth of stellar mass from DM mass by effectively blowing the gas away from the disc either into the circum-galactic medium or entirely out of the halo. This helps regulate the number density of low mass galaxies to the observed values by delaying star formation in these haloes.

The simulated star formation history of the Universe also matches a variety of different observations. The model predicts that the lowest mass galaxies ($9.5 < \log(M_\star/\mathrm{M}_\odot) < 10.5$) contribute little to the overall SFR density, while the intermediate ($10.5 < \log(M_\star/\mathrm{M}_\odot) < 11.5$) and high mass ($\log(M_\star/\mathrm{M}_\odot) > 11.5$) galaxies contribute equally up to $z = 3$. After $z = 3$, the star formation slows in the highest mass galaxies.

At $M_h > 10^{12}\mathrm{M}_\odot$, too many stars form, which is shown by the presence of galaxies above the abundance matching $M_\star - M_h$ relation and the lack of an exponential cutoff in the GSMF. These indicate that the thermal stellar feedback is unable to quench star formation in massive galaxies.

Comparing SFR with stellar mass, the simulated galaxies lie along a tightly correlated "star forming main sequence." The simulated galaxies match observations by Kajisawa et al. (2010) at $z \geq 3$, but there is a slight discrepancy at $z = 2$ between simulations and observations. At a given stellar mass, the simulated SFRs and correspondingly, the sSFRs, are ~ 2 times lower than the observed values at $9.5 < \log(M_\star/\mathrm{M}_\odot) < 10.5$. The high sSFRs in low mass haloes at $z = 2$ suggests that there needs to be a significant amount of cold gas still present in these galaxies at $z = 2$. Although our model does a better job of delaying the star formation at early times than most SAMs and hydrodynamic simulations, after $z = 3$ the simulated galaxies are forming too few stars.

Davé (2008) showed that the higher observed SFRs at $z \leq 2$ can be explained by an evolving stellar IMF, which becomes increasingly bottom-light at high redshift. However, Marchesini et al. (2009) showed that when such a bottom light IMF was used to model observations, the resulting observed high-redshift GSMF contained less galaxies, making the discrepancy with model GSMFs worse.

Regarding the evolution of sSFRs at $z > 3$, our simulation results are consistent with the revised Stark et al. (2013) observations for a sample of galaxies with stellar masses centred around $5 \times 10^9\mathrm{M}_\odot$. The increasing sSFR at $z \geq 4$ is consistent with increasing baryon accretion rates at larger redshift translating into larger sSFR in galaxies of fixed stellar mass. However, our simulated galaxies have lower sSFR values than observed at $z = 2$. Weinmann et al. (2012) argued that the correct sSFR evolution should follow naturally from the correct evolution of the GSMF. We see a slight deviation from the observed sSFR relation even though we match the GSMF. It must be noted that Weinmann et al. (2012) performed their analysis at $z < 2$, while our simulation has only reached at $z = 2$, where the observational estimates are less robust and and might show some internal inconsistency among different galaxy properties (e.g. sSFR and GSMF).

There may also be another physical mechanism delaying star formation. Krumholz et al. (2011) and Krumholz & Dekel (2012) argue that star formation depends sensitively on a metallicity threshold. Until gas reaches this threshold, which coincidentally also delays the formation of H_2, star formation is delayed in low mass galaxies at $z > 3$, which

leaves sufficient cold gas at $z = 2$ to increase the sSFR of these galaxies to the observed values.

To compare the model with observations of the local Universe, the inner 16 h^{-1} Mpc of the fiducial run was simulated with gas to $z = 0$. The $M_\star - M_h$ relation is reproduced at low masses ($\mathrm{M_h} = 10^{11}\mathrm{M_\odot}$) and an over cooling problem still exists at high masses ($\mathrm{M_h} = 10^{12}\mathrm{M_\odot}$). In the intermediate mass regime, we are below the relation by a factor of two. We also match the observed star forming main sequence quite well, although we are a bit above the relation throughout the entire mass range. These results indicate that our model does not fare so well at $z = 0$ as at high redshifts but the errors are low when compared to many semi-analytic models and simulations (Guo et al. 2011; Davé 2008).

Two low resolution (2×256^3 particles) realisations of the fiducial volume were simulated to test the effect of resolution and importance of ESF. Both volumes used the same the same physics as the fiducial volume, but one had ESF turned off. The low resolution volume fiducial simulation compares well with the high resolution fiducial run and observations for galaxies with $\mathrm{M_\star} > 10^{9.5}\mathrm{M_\odot}$ (20 star particles). However, the re-simulation without ESF has too many galaxies with $\mathrm{M_\star} > 10^{10}\mathrm{M_\odot}$.

Altogether, our results suggest that stellar feedback is one of the most important factors regulating star formation in $M_{halo} < 10^{12}\mathrm{M_\odot}$ galaxies. What is most important is *when* the feedback occurs rather than simply the amount of feedback energy. Simply increasing and decreasing the feedback energy will only set the normalisation i.e., the total stellar mass of present at $z = 0$, but the key is delaying star formation in low mass galaxies. When we include stellar feedback immediately after a star forms until supernovae stop exploding after 30 Myr, star formation is significantly delayed in low mass galaxies. In this way, we account for the downsizing in galaxy populations by delaying the star formation in low mass galaxies with our stellar feedback model and thus reconcile a couple key aspects of a ΛCDM cosmology with observations.

Chapter 5

Galaxy formation with local photoionization feedback

As discussed in the previous Chapter early stellar feedback (ESF) is very effective in reproducing the statistical properties of $L_\star$ and sub $L_\star$ galaxies. ESF works by dumping 10% of the bolometric luminosity of massive stars as thermal energy into nearby gas particles. The problem with this approach is that, such high feedback energies though, successful in producing the right amount of stars through cosmic time, does not get some of the morphological properties of the disc right. Roškar et al. (2013) find that although strong feedback appears to be a viable mechanism to regulate the stellar mass fraction in $L_\star$ galaxies, it also prevents the formation of discs with reasonable morphologies. In models with strong stellar feedback, stellar discs are too thick while the gas disc morphology is completely destroyed. They conclude that it is impossible to preserve spiral disc morphology while at the same time expelling enough baryons to satisfy the abundance matching constraints. Stinson et al. (2013a), find that their galaxy simulations which match the stellar-halo mass ratios forms do reproduce spiral structures but also form a substantial thick disc, not observed in galaxies. Is there a way to solve this problem? All feedback models place emphasis on blowing out the gas from the disc in order to regulate star formation, but are they calculating the gas inflow into the disc correctly. If the gas inflow rate can be reduced, then very strong feedback mechanisms might not be necessary.

Radiative cooling controls the infall of gas onto the disc, making it one of the most important processes of galaxy formation. A number of factors slow the infall of gas including thermal pressure (Rees & Ostriker, 1977; Binney, 1977) and the incident radiation field (Rees, 1986; Efstathiou, 1992; Cantalupo, 2010; Gnedin & Hollon, 2012).

The work presented in this Chapter has been published in Kannan et al. (2014b).

Accurately modelling the cooling rate of halo gas is critical to determining how much fuel is available to form stars in the galaxy.

Gas cooling (Λ) depends most strongly on gas density ($\Lambda \sim n^2$), metallicity and the ionization state. The local gas hydrodynamics determines the gas densities while chemical enrichment from stellar evolution determines the metallicity. The gas ionization state depends on the temperature of the gas and on the incident radiation field from stars, Active Galactic Nuclei (AGN) and other radiation sources. In most galaxy formation models (including numerical hydrodynamical simulations), a uniform background is used to represent this radiation field. This background evolves with redshift according to the cosmic star formation and quasar luminosity histories (Haardt & Madau, 2012).

Rees (1986) and Efstathiou (1992) showed that photoionization can prevent gas from cooling into low mass haloes. Wiersma et al. (2009) presented more detailed results that measured the effect of a uniform photoionization background on individual ion species. Gnat & Ferland (2012) extended this analysis to include a variety of radiation fields that could vary due to proximity to galaxies. Oppenheimer & Schaye (2013a,b) explored the problem with a full chemical network including all the ionization states of 30 elements in typical parcels of gas in the intergalactic medium (IGM) and found that the time it takes for gas to reach ionization equilibrium can lead to significant changes in the state of gas in the IGM.

Cantalupo (2010) explored analytically the effect of local sources of radiation on the cooling of halo gas including the soft X-ray emission produced by star formation events, a component that is absent within typical stellar population synthesis models such as Starburst99 (Leitherer et al., 1999) (SB99) that only considers the blackbody radiation from young massive stars. Such low energy photons do not affect the cooling rate of high metallicity gas. However, massive stars are also strong X-ray sources due to their stellar winds, supernova remnants and binary interactions. When the high energy radiation from these sources is included in gas cooling models, their radiation can ionize the metals and can decrease the cooling rate of high metallicity gas considerably. Gnedin & Hollon (2012) created a general model for cooling in the presence of a radiation field near a galaxy (including both stars and AGNs). They showed that for a sufficiently general variation in the spectral shape and intensity of the incident radiation field, the cooling and heating functions can be approximated based only the photoionization rates of a few important coolants.

In this work, we follow the lead of Cantalupo (2010) and Gnedin & Hollon (2012) in an attempt to self consistently include local ionization sources, in addition to the uniform background of Haardt & Madau (2012), in cosmological simulations of galaxy formation. One of the great challenges for including the effect of photoionization in simulations is the need to trace the radiation as it propagates through the simulated volume. The radiation field at any given point is dependent on the brightness and distance to the source as well

as the frequency dependent optical depth of the material between the source and sink. This makes the problem more expensive than the $\mathcal{O}(N^2)$ direct calculation of gravity. Various solutions have been implemented for this complex computational problem. Gnedin (2008) used the local Sobolev approximation that calculates the column density from the density of a resolution element divided by the size of that element. Altay et al. (2008) (SPHRAY) and Pawlik & Schaye (2008) (TRAPHIC) both implemented sophisticated ray-tracing schemes in smoothed particle hydrodynamics (SPH) simulations. Altay & Theuns (2013) presented a recent update to SPHRAY. Petkova & Springel (2011) traced radiation through AREPO, a code that solves hydrodynamics on a moving mesh. For a review of how the different schemes perform in a variety of common test cases, see Iliev et al. (2009). While such radiative transfer schemes are useful tools for studying reionization, these methods are so computationally demanding that it is impossible to evolve a cosmological simulation of galaxy formation much past $z = 4$.

Such models have been used in galaxies simulated to $z = 0$ in post-process. Fumagalli et al. (2011) solved radiative transfer on a high resolution grid to find that local radiation ionize moderate column density gas and thus reduces the number of Lyman limit and damped Lyman α systems. Rahmati et al. (2013) used TRAPHIC post-process and found similar results. However, these studies do not yet explore the impact of the radiation field on the galaxy evolution.

Since it is as yet unclear what the effect of including local ionization sources on galaxy evolution, we have decided to take a simple approach to the calculation of the radiative transfer, where possible. Our aim is to find a compromise between simulating a galaxy in a cosmological context from high redshift down to $z = 0$ and the precision of an on-the-fly radiative transfer calculation.

This Chapter describes how we calculate the cooling rates using a radiative transfer method based on the gravity tree algorithm and presents a preliminary simulation based on them. The Chapter is organized as follows: §5.1 presents the details of the cooling calculation. §5.2 describes the photoionization sources we explicitly consider in our calculation. §5.3 outlines the approximations used in our radiative transfer approach while §5.4 describes the construction of the cooling table. Finally, in section §5.5 and §5.6 we present the results of our implementation of the local photoionization feedback on a test gas particle and on a fully cosmological simulation of galaxy formation. Our conclusions are presented in §5.7.

5.1 Gas Cooling

A number of processes determine the internal heating (H) and cooling (Λ) rates in the hydrodynamic energy equation:

$$\frac{D\epsilon}{Dt} = -\frac{P}{\rho}\vec{\nabla}.\vec{u} - \frac{1}{\rho}\vec{\nabla}.\vec{F} + \frac{1}{\rho}\Psi + \frac{\mathrm{H}-\Lambda}{\rho} \tag{5.1}$$

where ϵ represents the specific internal energy of a parcel of gas, $P\vec{\nabla}\cdot\vec{u}$ represents the adiabatic work done on the gas, $\vec{F}$ represents the flux of heat that is conducted out of the parcel, and Ψ represents the viscous dissipation rate.

Both the heating and cooling rates are a function of the density, n_i, of each ion species present in the gas parcel, as well as the parcel's temperature, T, and incident radiation field, J_ν:

$$\frac{H-\Lambda}{\rho} = f(n_i, T, J_\nu) \tag{5.2}$$

The density of each ion species is subject to a number of creation and destruction processes, which in turn also depend on n_j, T and J_ν:

$$n_i = f(n_i, T, J_\nu) \tag{5.3}$$

The densities of the ion species can be obtained using networks of differential equations that account for all the electrons that are made available when atoms are ionized. Such networks can become arbitrarily complicated depending upon how many elements are included (Ferland et al. 1998; Gnat & Ferland 2012; Oppenheimer & Schaye 2013a). In simulations, it is possible to carry the ionization state of every species from timestep to timestep to keep the non-equilibrium ionization state of each element rather than making the assumption of ionization equilibrium (eg. Oppenheimer & Schaye 2013b).

5.1.1 Primordial Cooling: non-equilibrium

Since these differential equations need to be solved for each particle during every timestep in a simulation, it becomes necessary to limit the calculation of non-equilibrium ionization states to hydrogen and helium. We use the implementation of Shen et al. 2010 (see also Vogelsberger et al. 2013). Hydrogen and helium are the most abundant elements in the Universe, so their temperature and ionization state are important in determining the dynamics and cooling of gas in simulations.

Primordial gas contains various ionization states of hydrogen and helium:
$(\mathrm{HI}, \mathrm{HII}, \mathrm{HeI}, \mathrm{HeII}, \mathrm{HeIII}, \mathrm{e}^-)$. The rate of change of densities of these species are obtained by solving the following set of differential equations:

$$\frac{dn_{\mathrm{HI}}}{dt} = \alpha_{\mathrm{HII}} n_{\mathrm{HII}} n_e - \Gamma_{e\mathrm{HI}} n_e n_{\mathrm{HI}} - \Gamma_{\gamma\mathrm{HI}} n_{\mathrm{HI}} \tag{5.4}$$

$$\begin{aligned} \frac{dn_{\rm HeI}}{dt} &= (\alpha_{\rm HeII} + \alpha_d) n_{\rm HeII} n_e \\ &\quad -\Gamma_{e\rm HeI} n_e n_{\rm HeI} - \Gamma_{\gamma\rm HeI} n_{\rm HeI} \end{aligned} \tag{5.5}$$

$$\begin{aligned} \frac{dn_{\rm HeII}}{dt} &= \alpha_{\rm HeIII} n_{\rm HeIII} n_e + \Gamma_{e\rm HeI} n_e n_{\rm HeI} \\ &\quad +\Gamma_{\gamma\rm HeI} n_{\rm HeI} - (\alpha_{\rm HeII} + \alpha_d) n_{\rm HeII} n_e \\ &\quad -\Gamma_{e\rm HeII} n_e n_{\rm HeII} - \Gamma_{\gamma\rm HeII} n_{\rm HeII} \end{aligned} \tag{5.6}$$

where α_i is the *radiative* recombination coefficient for ion species i, α_d is the *dielectric* recombination coefficient, which only applies to HeII, Γ_{ei} is the *collisional* ionization rate for each species, while $\Gamma_{\gamma i}$ is the photoionization rate, defined as

$$\Gamma_{\gamma i} = \int_{\nu_{Ti}}^{\infty} \frac{4\pi J_\nu}{h\nu} \sigma_{\nu i} \, d\nu \tag{5.7}$$

where $\sigma_{\nu i}$ is the frequency dependent photoionization cross section of the species 'i'. These equations are closed when combined with the following set of conservation equations:

$$n_{\rm HI} + n_{\rm HII} = n_{\rm H} \tag{5.8}$$

$$n_{\rm HII} + n_{\rm HeII} + 2n_{\rm HeIII} = n_e \tag{5.9}$$

The cosmic production of helium was constrained by Jimenez et al. (2003) using K dwarfs from Hipparcos catalog with spectroscopic metallicities and found that the amount of Helium produced compared to heavier elements in stars follows the relation: $\Delta Y/\Delta Z = 2.1 \pm 0.4$. In accordance with this result we compute the helium abundance in the following manner:

$$Y_{\rm He} = \begin{cases} (0.236 + 2.1{\rm Z})/4.0 & \text{if Z} \leq 0.1 \\ (-0.446(Z - 0.1)/0.9 + 0.446)/4.0 & \text{if Z} > 0.1 \end{cases}, \tag{5.10}$$

with the density of hydrogen being

$$Y_{\rm H} = 1.0 - 4Y_{\rm He} - {\rm Z}, \tag{5.11}$$

where

$$Y_i = \frac{n_i M_{\rm H}}{\rho} \tag{5.12}$$

where M_H is the mass of the hydrogen atom and ρ is the total density of the gas. Most of the radiative processes discussed above along with collisional excitation that causes the gas to cool, and the coefficients and the cooling rates are enumerated in Anninos et al. (1997).

In addition to determining the ionization state of gas, the incident radiation field also injects energy into the gas when a high energy ($h\nu > h\nu_T$) photon, transfers the rest of its energy to the electron it frees from the atom. The photo heating rate is thus given by

$$\mathrm{H} = n_{\mathrm{HI}}\epsilon_{\mathrm{HI}} + n_{\mathrm{HeI}}\epsilon_{\mathrm{HeI}} + n_{\mathrm{HeII}}\epsilon_{\mathrm{HeII}}, \tag{5.13}$$

where

$$\epsilon_i = \int_{\nu_T}^{\infty} \frac{4\pi J_\nu}{h\nu}\sigma_{\nu i}(h\nu - h\nu_T)\, d\nu \tag{5.14}$$

5.1.2 Metal cooling: equilibrium

A significant amount of cooling also occurs via elements heavier than hydrogen and helium. For these elements, we refrain from solving the entire non-equilibrium ionization network due to its computational complexity. Instead, we assume equilibrium conditions hold and interpolate values in a look-up table as implemented in Shen et al. (2010).[1] The table consists of heating and cooling rates as a function of total gas density, temperature, redshift, and the radiation fields from local sources, described in §5.2. Metallicity does not need to be a dimension in our table, since the cooling rate scales linearly with metallicity and can thus be easily calculated from the cooling rate of solar metallicity gas (see also Shen et al. 2010 and Vogelsberger et al. 2013).

Thus, our total cooling calculation is the summation of three components: i) non-equlibrium primoridal - calculated on the fly in the code; ii) equilibrium metals - values tabulated from Cloudy (v10.00, last described in Ferland et al. 1998) ; and iii) Compton scattering of CMB photons,

$$\Lambda_{tot} = \Lambda_{\mathrm{H,He}} + \frac{\mathrm{Z}}{\mathrm{Z}_\odot}\Lambda_{\mathrm{Z}_\odot} + \Lambda_c. \tag{5.15}$$

This division neglects some sources of free electrons in the cooling calculation. Cloudy calculates the cooling rates of metals using the free electrons created in ionization equilibrium primordial cooling. This number of free electrons may be different from the non-equilibrium primoridal cooling in our code. Additionally, our non-equilibrium primordial cooling calculation assumes that the number of free electrons released from metals is negligible. Thus, our cooling calculation is a first approximation that can be improved by tracking non-equilibrium metal cooling in addition to H & He. It is worth noting that this assumption is used in practically all current numerical implementations of metal dependent gas cooling (Shen et al. 2010; Vogelsberger et al. 2013).

[1] Refer to Appendix A for a discussion on the difference between the non-equilibrium and equilibrium cooling calculations.

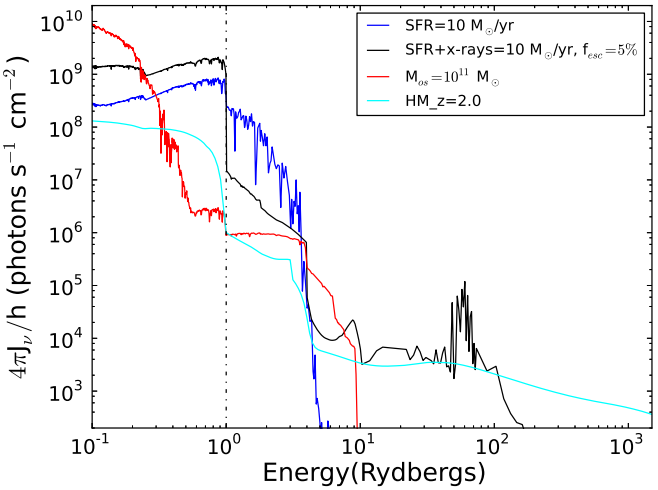

Figure 5.1 The incident photon flux from the photoionization sources considered in our simulations. These fluxes are reported at 10 kpc from the source. The blue curve shows the photon flux as a function of energy from a population of young stars forming at the rate of 10 $M_\odot$ yr^{-1}. The young stars have the highest photon flux at the hydrogen edge but decreases quickly at higher energy. The black curve shows the spectrum of young stars including the x-ray luminous cooling of shock-heated gas after a SNe event. The Spectral Energy Distribution (SED) of a 10^{11} $M_\odot$, old (>200 Myr) stellar population is shown in red. Old stars emit fewer photons than young stars at the hydrogen edge, but has higher flux at higher energies ($h\nu > 4$ Rydberg). The cyan curve shows the UV background at $z = 2$. Compared to the plotted ionization fields, this background flux is lower than local sources at low energies($h\nu < 100$Rydberg), but dominates at higher energies due to the hard photons emitted by AGN.

5.2 Ionizing stellar radiation sources

There are many radiation sources which produce high energy photons and ionize gas in the galaxy. In the following sections we outline the sources that we consider in our photoionization model. One source of radiation not included in our model is quasars, since we do not follow the formation or gas accretion onto super massive black holes in our cosmological simulations. However, Vogelsberger et al. (2013) showed that the low frequency duty cycle of radiation from AGNs result in a minimal impact on the large scale gas dynamics in galaxies.

5.2.1 UV Background

Nearly all simulations include the effect of photoionization from a uniform background. This UV background accounts for the UV radiation that all stars and AGN emit throughout the evolution of the Universe attenuated by the Lyman-α forest (Haardt & Madau, 2012). Our refined method is an attempt to account for more local ionizing radiation. The Spectral Energy Distribution (SED) from Haardt & Madau (2012) (henceforth, HM)

is shown as the cyan curve in Fig. 5.1. Since the HM SED incorporates the emission from AGNs, it contains photons up to x-ray energies, but the photon flux can be lower than local sources at low energies. We consider the HM SED as the minimum ionizing flux seen by the gas particles in our simulations, for $z < 9$.

5.2.2 Young Stars

Our initial spectral energy distribution (SED) for young stars comes from STARBURST99 (Leitherer et al., 1999) using an SED taken 10 Myr after stars start forming at a constant rate of 1 $M_\odot$ yr^{-1} using the "present day" (Eq. 6) IMF from Kroupa (2001) (blue curve in Fig. 5.1). The SED has a relatively high photon flux at the hydrogen edge (13.6 eV) but the flux drops precipitously to higher energies, with almost no flux above the helium edge (4 Rydbergs = 54.4 eV).

Fig. 5.2, shows how the cooling (solid curves) and heating (dashed curves) rates change in the presence of various levels of the radiation field (SFR=1 $M_\odot$ yr^{-1}, blue curve ; SFR=100 $M_\odot$ yr^{-1}, black curve) from young stars compared to the cooling and heating rates in the presence of the peak HM radiation field (red) at $z = 2$. The gas used to make these cooling curves has a density of $n_H = 0.01 cm^{-3}$, a metallicity of $Z = 0.01 Z_\odot$ and is at a distance 10 kpc from the star forming region. The cooling curve is calculated using the assumption that the gas in between the source and the gas test particle is optically thin. Thus, the flux is inversely proportional to distance squared. All test cooling curves presented in this section were calculated using the code CLOUDY, which assumes photoionization equilibrium for all elements.

The STARBURST99 young star SED suppresses hydrogen cooling and low temperature metal cooling that dominates in T $< 10^4$ K gas. The spectrum also partially ionizes some helium in strong radiation fields. It also slightly changes the equilibrium temperature of the gas. The equilibrium temperature is defined as the temperature where cooling transitions to heating because of the incident radiation file. Practically, it corresponds to the temperature at which the heating and cooling rates are equal. At temperatures above equilibrium, the gas cools, while at lower temperatures, it heats up. So, the equilibrium temperature depends on the shape of the heating and cooling curves.

Radiation fields change the heating and cooling curve depending on the energy of photons they possess. HM has the most high energy photons, whose extra energy results in heating, so it has the highest heating rates, but is has a low flux at low energies ($1 - 10$ Rydbergs) causing minimal impact on the cooling of low metallicity gas. The young star blackbody spectrum includes mostly photons around the hydrogen ionization edge, so it results in minimal heating, but a large reduction in the cooling rate. The net result is that the radiation from new stars, for typical values of radiation field in the galaxy, is more effective at raising the equilibrium temperature of the gas than the background HM UV spectrum.

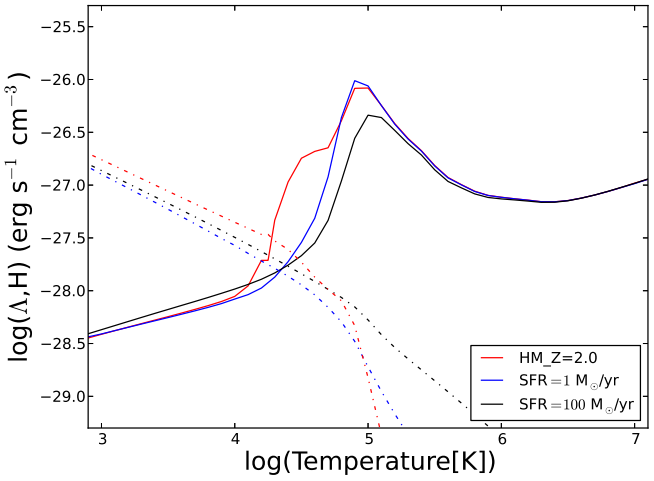

Figure 5.2 The cooling (solid) and heating (dashed) rate curves of gas in the blackbody radiation field of young stars (STARBURST99) at two star formation rates compared to the cooling and heating in presence of the HM UV background spectra. The cooling rates are shown for gas with a density, $n_H = 0.01$ cm^{-3}, metallicity, $Z = 0.01 Z_\odot$, and a radiation source 10 kpc distant.

Fig. 5.3 shows the effect of metallicity on the cooling function at a fixed star formation rate of 10 M$_\odot$ yr^{-1}. While this radiation field eliminates hydrogen and low temperature metal cooling at solar metallicity (note the lack of a peak around 10^4 K in the red curve), high temperature metal cooling is not suppressed and hence the cooling rates are more than an order of magnitude higher than in the low metallicity gas (blue) at high temperatures. The higher cooling rates mean that the equilibrium temperature of the gas is also an order of magnitude lower in solar metallicity (red curve) gas because the heating rate does not change. Fig. 5.3 shows that cooling is most easily suppressed in low metallicity gas irradiated with a soft UV spectrum from young stars.

5.2.3 X-rays from Young Stars

Cantalupo (2010) considered the radiation from young stellar populations, including both the blackbody radiation from hot young stars and the X-rays that supernovae remnants emit. Using analytic calculations, Cantalupo (2010) showed that while stellar photons ionize hydrogen and low ionization metal states while soft X-rays ionize other significant metal coolants. The x-ray photoionization increased the equilibrium temperature, which consequently slowed the accretion of gas onto the disc.

X-rays are produced in a number of ways. Rapidly outflowing gas from stellar winds or supernova explosions shocks against the interstellar medium (ISM) and thermalises (Heckman et al. 1995; Strickland et al. 2004). Non-thermal processes associated with

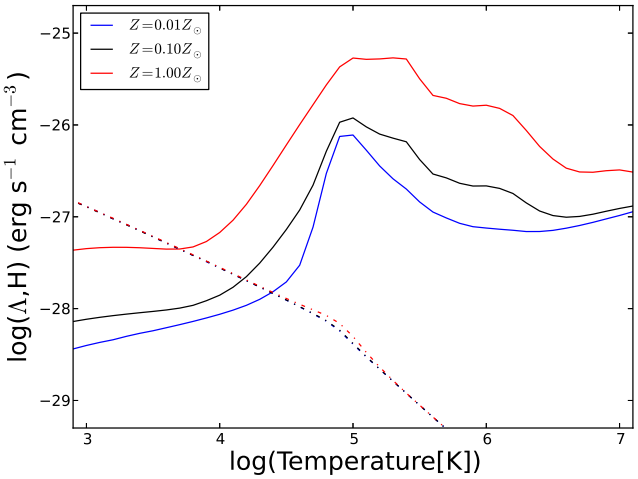

Figure 5.3 Cooling function as in Fig. 5.2 of gas at a variety of metallicities in a radiation field 10 kpc away from a stellar population forming stars at 10 $M_\odot$ yr^{-1}. This young population only emits radiation to the helium edge (4 Rydberg), so only the hydrogen cooling at $T < 10^5$ K is reduced. The increase in cooling in higher metallicity gas in the range $10^4 < T < 10^5$ is due to an increasing presence of heavy metal coolants such as O, Ne and Fe. The heating rate remains constant because the radiation field is the same for all three curves.

supernovae explosions and high mass X-ray binaries also emit x-ray radiation (Grimm et al. 2003; Persic et al. 2004).

We use the SED for a 5 Myr old stellar population (Fig. 5.1, black curve) from Cerviño et al. (2002). The Cerviño et al. (2002) SEDs are derived from models of young O and B stars and the X-rays that their stellar winds and supernova explosions produce. Their models are calibrated to match the observed relationship between SFR and soft X-rays (for eg. see Heckman et al. 1995). In their models, the X-ray emission peaks when the stellar population is $\sim$ 5 Myr old and continues for $\sim$ 100 Myr. To simplify our calculation, we use the SED of a 5 Myr old stellar population for all stars younger than 10 Myr, so we pick the maximum emission SED, but only use it for one-tenth of the time that x-rays are emitted. Following Cantalupo (2010), we assume that 5% of the mechanical energy from the SNe is emitted as X-rays.

The Cerviño et al. (2002) models assume a Salpeter IMF, but our simulations use a Chabrier (2003) IMF that has more stars with $M_\star > 8$ $M_\odot$. So, we renormalise the Cerviño et al. (2002) SED to make the flux from O & B stars and the number of subsequent SNe events consistent with the Chabrier IMF.

There is significant absorption of Lyman continuum photons in the galaxy due to the abundance of hydrogen. To include this effect we assume an escape fraction of 5% around Lyman-limit frequencies to mimic the highly absorptive nature of their birth molecular

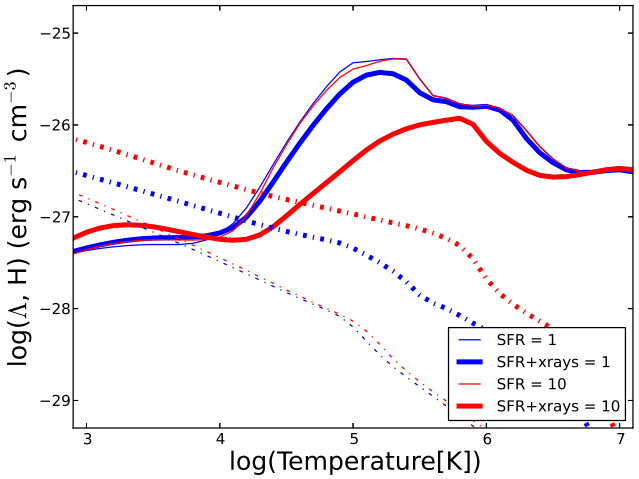

Figure 5.4 The cooling function as in Fig. 5.2, but now includes the effect of x-rays from young stellar populations (Cerviño et al. 2002). While blackbody radiation from young stars only quenches hydrogen cooling, the addition of x-rays stops cooling from many metal ion species and increase the heating rate considerably (see Cantalupo 2010).

clouds (e.g. Bergvall et al. (2006), see section 5.3.1 for a more thorough discussion on the escape fraction).

Fig. 5.4 shows how including X-rays in the young star SED affects the cooling curve in $Z = Z_{\odot}$ gas at 10^{-2} cm^{-3} density at 1 kpc from the star formation site. At high metallicity, the young star SED without X-rays (thin curves) only eliminates hydrogen and low temperature metal cooling, independent of the star formation rate of the galaxy. The harder x-ray spectrum (thick curves) fully ionizes heavier elements thereby reducing the gas cooling rate at higher temperatures and also raises the heating rate of the gas. These effects combine to increase the equilibrium temperature by an order of magnitude. X-rays thus remain an important ionization source at low redshifts, where the halo gas has been metal enriched by continuous bursts of star formation. For this reason, we use, in our simulations, an SED that combines the black body emission of young stars with the x-ray emission that massive stars produce in supernova explosions in our simulations. Henceforth, flux from young stars includes x-rays along with their black body spectrum.

5.2.4 Old Stars

Naively, old stellar populations seem like they should not be sources of ionizing photons. Since all the hot young stars have exploded as supernovae, all that are left are cool, old stars. However, a UV upturn was observed coming from the old stellar population at the center of M31 (Code, 1969), and was determined to be light from extreme horizontal branch stars. Subsequently, UV radiation has been detected from many quiescent, early

type galaxies (Kaviraj et al., 2007). What fraction of this radiation is from young stars, forming at low rates, compared to how much is from old stars is still a question waiting to be answered with better observations. Additionally, recent UV telescopes like GALEX have only been able to detect relatively soft UV radiation sources. However stellar population synthesis models predict that stars that have shed their outermost envelopes, so called "post-AGB" stars, should emit a hard UV spectrum.

Bruzual & Charlot (2003) include such stars in the spectral energy distribution of a simple stellar population (SSP). The SED of SSPs older than 200 Myr is harder, though much fainter (at the hydrogen edge), than the UV SED for a young SSP. In the model, the photon flux increases near the helium edge, due to the accumulation of post AGB stars. The shape of the SED remains fairly constant from 200 Myr to 13 Gyr because low mass stars evolve within a narrow temperature range all the way from the main sequence to the AGB phase. This implies that a constant SED can be used for old stars irrespective of their age (Fig. 5.1, red curve). We choose the 2 Gyr SED since it is near the mean of the SEDs.

Fig. 5.5 shows the effect of the old star SED on the cooling function of gas as a function of intensity of the incident radiation field. The gas has the same conditions as that studied in §5.2.2 ($n_H = 0.01$ cm^{-3}, $Z = 0.01 Z_\odot$, d=10 kpc). The radiation with energies higher than the helium edge can eliminate helium cooling in the gas. A galaxy with M$_\star = 10^{10}$ M$_\odot$ has less effect on the cooling function than the peak HM UV background ($z = 2$) because its ionizing flux is so low. 10^{11} M$_\odot$ stars produce a strong enough radiation field to reduce cooling below the HM level. Thus, radiation from old stars starts to play a role in massive galaxies, where the radiation field is strong, and at lower redshifts, once the HM background has decreased from its peak. Thus, they might help limit star formation in massive elliptical galaxies.

The consequences of photoionization that are most critical for galaxy formation are the decrease in the cooling rate of the gas and the increase in the equilibrium temperature, which is the minimum temperature to which gas can cool. Moreover, the equilibrium temperature sets the minimum pressure a gas parcell can reach. More intense and harder radiation fields shift the equilibrium temperature higher, while higher densities and metallicities shift the equilibrium temperature lower.

5.3 Calculating the Radiation Field

In the previous section, the different sources of local ionizing radiation were enumerated and shown to be important in the calculation of gas cooling in galaxies. However, propagating the radiation from the sources to the gas particles can become computationally expensive (e.g. Altay et al. 2008). This necessitates the use of some simplifying, albeit

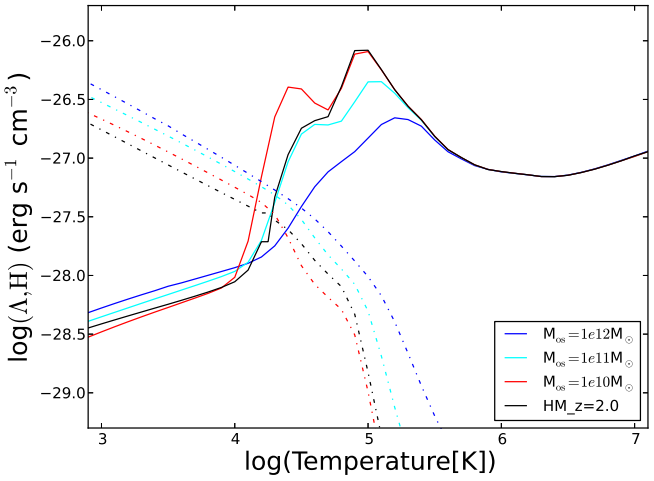

Figure 5.5 The heating and cooling functions for gas as in Fig. 5.2 irradiated by various masses of old (t>200 Myr) stars. The SED is taken from Bruzual & Charlot (2003).

physically motivated, assumptions. We plan to relax these assumptions in future work in order to present a more complete implementation of radiative transfer.

5.3.1 Escape Fractions

Our strongest assumption is that the gas is optically thin to photons so that the optical depth is determined simply by the escape fraction of ionizing photons from the interstellar medium (ISM). Given the abundance of neutral hydrogen in the Universe, Lyman continuum photons with around 1 Rydberg of energy will generally see high optical depths and thus have short travel distances and low escape fractions. In future work, we will try to improve our model to make more physical calculations for the optical depth. For now, we assume that since young stars form embedded in molecular clouds, the photoionizing escape fraction, f_{esc}, is low ($f_{esc} \sim 5\%$). This number is an upper limit, motivated by a number of observations (Bergvall et al. 2006; Grimes et al. 2009; Steidel et al. 2001; Shapley et al. 2006; Siana et al. 2007; Nestor et al. 2013). The escape fraction we use is frequency dependent (f_{esc}^{ν}), similar to Cantalupo (2010),

$$f_{esc}^{\nu} = [f_{esc}^{LL} + (1 - f_{esc}^{LL})e^{-\tau_{\nu}}] \tag{5.16}$$

where f_{esc}^{LL} is the absolute escape fraction at the Lyman Limit, $\tau_{\nu} = \sigma_{\nu} N(H^0)$ is the neutral hydrogen optical depth and σ_{ν} the corresponding cross-section. Our 5% escape fraction means that we fix $f_{esc}^{LL} = 0.05$. The value of N(H^0) determines the hardening of the spectrum around the Lyman Limit. We anticipate that this parameter has a little effect on our results and we fix N(H^0) = 10^{20} cm^{-2} . Escape fractions are a strong

function of the distance from the source. $f_{esc} = 5\%$ represents the mean escape fraction at our spatial resolution $\sim$ 300 pc. For old stars, we assume that they have left their dense birth locations and that the escape fraction of their ionizing photons is 100%.

5.3.2 Combining Sources

Each parcel of gas will receive a ionizing flux from *all* the radiation sources (stars in our case) with an intensity proportional to the inverse of the distance square. In order to reduce the computational cost of the distance calculation, we exploit the tree algorithm used to compute the gravitational force , which already groups sources according to the their distance from the gas particle. Our grouping scheme is a first rough attempt at calculating radiative transfer. Our initial attempt takes little account of absorption except for the constant escape fraction used for young stars described above.
Combining sources of the same kind is an algebraic operation, since the SEDs do not evolve with time, so the summation of SEDs only affects their normalisation. In this manner, the radiation field incident on a gas particle is calculated using two separate components, one from young stars ($\phi_{\rm SFR}$) and one from old stars ($\phi_{\rm os}$) Young stars in our scheme are all those with an age < 10 Myr, while old stars have an age > 200 Myr.[2] For each gas particle, the effective flux, ϕ, is the sum of the sources normalized by the distance from the gas particle squared, as follows:

$$\phi_{\rm SFR} = \frac{1}{10^7 \text{ yr}} \sum_{i=1}^{N} \frac{M_i(t < 10\text{Myr})}{(r_i \text{ kpc})^2} \tag{5.17}$$

$$\phi_{\rm os} = \sum_{i=1}^{N} \frac{M_i(t > 200\text{Myr})}{(r_i \text{ kpc})^2} \tag{5.18}$$

with the total photoionization and heating rates, for each species 'i', given by

$$\Gamma_{\gamma i} = \phi_{\rm SFR}\Gamma_{\gamma i,\rm SFR} + \phi_{\rm os}\Gamma_{\gamma i,\rm os} + \Gamma_{\gamma i,\rm HM} \tag{5.19}$$

$$\epsilon_i = \phi_{\rm SFR}\epsilon_{i,\rm SFR} + \phi_{\rm os}\epsilon_{i,\rm os} + \epsilon_{i,\rm HM}. \tag{5.20}$$

Here, $\Gamma_{\gamma i,\rm SFR}$ and $\epsilon_{i,\rm SFR}$ are normalised to a radiation field 1 kpc away from a population forming stars at a rate of 1 $M_\odot$ yr^{-1}. These quantities are calculated using Eqs. 5.7 and 5.14, with the SED of these stars taken from Cerviño et al. (2002) (see §5.2.3). Similarly, $\Gamma_{\gamma i,\rm os}$ and $\epsilon_{i,\rm os}$ are normalised based on a radiation field 1 kpc away from a > 200 Myr stellar population with a mass of 1 $M_\odot$. For the old stars the SED is taken from Bruzual & Charlot (2003) as mentioned in §5.2.4. $\Gamma_{\gamma i,\rm HM}$ and $\epsilon_{i,\rm HM}$ are the

[2] No flux from stars in between these two ages is considered, in agreement with results from Bruzual & Charlot (2003)

UV background photionizing and photo heating rates, which are redshift dependent and taken from Haardt & Madau (2012). The cooling table uses separate values for $\phi_{\rm SFR}$, $\phi_{\rm os}$, and redshift in addition to temperature and density to determine the cooling rate for the gas.

Therefore, the photoionization rate, Γ, and the heating rate, ϵ, for each species (i), used in the non-equilibrium calculation can simply be summed as shown in Eq. 5.19 & 5.20. For a short description about how the distance (r_i) is calculated see §5.6.

5.4 Cooling table creation

As shown in Eq. 5.15, the total gas cooling is divided into primordial, metal and Compton cooling. The primordial and Compton cooling is calculated on-the-fly as described in §5.1.1. However, to reduce the complexity of the cooling calculation as the simulation runs, the metals are assumed to be in ionization equilibrium and their heating and cooling rates are tabulated across a range of physical conditions using Cloudy. This look up table is used in the simulations.

The table has four dimensions at $z > 9$ and five dimensions thereafter. The four common dimensions are density, temperature, $\phi_{\rm SFR}$ and $\phi_{\rm os}$. After $z = 9$, the UV background turns on so a redshift dimension is added to track how the HM SED shape changes. We make the division at $z = 9$, even though Haardt & Madau (2012) tabulate the UV background to $z = 15$, in order to limit the size of the cooling table. The mean free path of photons at high redshift is low because the Universe is not yet reionized, so the flux of the background UV field is relatively low. There is never a metallicity dimension in the table as cooling is assumed to scale linearly with metallicity as discussed in §5.1.2.

In both parts of the cooling table, the density ranges from 10^{-9} cm^{-3} to 10^{4} cm^{-3} with a spacing of 0.5 dex in log space. The temperature ranges from 10^2 K to 10^9 K with a resolution of 0.1 dex. At $z > 9$, $\phi_{\rm SFR}$ ranges from 10^{-11} to 10^2 $\rm M_\odot$ $\rm yr^{-1}$ $\rm kpc^{-2}$ with a resolution of 0.5 dex, and $\phi_{\rm os}$ ranges from 10 to 10^{10} $\rm M_\odot$ $\rm kpc^{-2}$ also with a resolution of 0.5 dex. These minimum values correspond to the CIE cooling rates, while the maximum values correspond to the maximum star formation rate and mass of high redshift galaxies. For $z \leq 9$, $\phi_{\rm SFR}$ covers a smaller range, 10^{-5} to 10^3 $\rm M_\odot$ $\rm yr^{-1}$ $\rm kpc^{-2}$ with a resolution of 0.5 dex. $\phi_{\rm os}$ ranges from 10^6 to 10^{12} $\rm M_\odot$ $\rm kpc^{-2}$ with 0.5 dex spacings. The minimum values are higher at $z \leq 9$ because the HM UV background sets the minimum rather than collisional ionization equilibrium. The maximum SFR and mass are increased to reflect observations. The redshift dimension that accounts for the UV background ranges from 9.0 to 0.0 with a resolution of 0.5. The resolutions were motivated by Gnedin & Hollon (2012).

To create the table, cooling and heating rates are calculated at every point for solar and primordial metallicity gas using Cloudy. The difference between the solar and

primordial metallicity values is stored as the heating and cooling rates due to the metals only. The values are stored as natural logarithms with single point precision, which provides accurate values, and limits the size of the table to 78 MB, a size well within the memory capacity of modern computer hardware.

5.5 Test Particle Evolution

The methods described in the previous sections are implemented in the smoothed particle hydrodynamics (SPH) code GASOLINE first described in Wadsley et al. (2004) (also see Chapter 1). As a first test of the cooling implementation, we calculate the evolution of the temperature and ionization state of a single isolated particle over the course of 350 Myr. The particle stays at a constant density and metallicity since it is not part of a fully dynamic simulation. The effects of dynamics are explored in a full simulation in §5.6.

Fig. 5.6 shows the evolution of a gas particle with a density $n_H = 0.001$ cm^{-3} in a young star radiation field that includes x-rays as described in §5.2.3. Unlike for the cooling curves in §5.2 that showed the effect of the stellar fields and HM separately, now their fields are combined as described in §5.3.2. The effect of the background UV field alone is shown as the blue curve. The distance from the source to the test gas particle is 10 kpc. The left column shows how the particle cools when its metallicity is 0.01 $Z_\odot$, similar to unenriched gas falling for the first time into a galactic halo (Brook et al., 2013). The right column shows the particle cooling time when its metallicity is 0.1 $Z_\odot$, similar to gas that has cooled into the disc and has been ejected into the halo (Brook et al., 2013). A comparison of the top two panels shows that cooling times are longer and the equilibrium temperatures are higher in low metallicity gas. Compared to the HM line, the top right panel shows that X-rays also prolong cooling at $0.1Z_\odot$, though to a lesser extent than at $0.01Z_\odot$. The lower four panels show that the young star radiation fields keep hydrogen and helium ionized even after the gas cools. What is not shown in the ionization plots is that they can also ionize other potential metal coolants.

For each metallicity, stronger radiation fields reduce the neutral hydrogen and HeII fractions (middle and bottom panels). In the 0.01 $Z_\odot$ case, the lack of metals means that the delayed cooling is primarily due to the ionization of hydrogen and helium. While the fractions of neutral hydrogen and HeII are similar between the 0.01 $Z_\odot$ and 0.1 $Z_\odot$ with the same ionization field, the cooling rate in 0.1 $Z_\odot$ is higher. The faster cooling is due to metal coolants more prevalent in the 0.1 $Z_\odot$ gas. Since metal cooling is computed using equilibrium gas in CLOUDY, it is impossible to show the ionization state of the metal coolants in our current test particle runs (but see Oppenheimer & Schaye, 2013a).

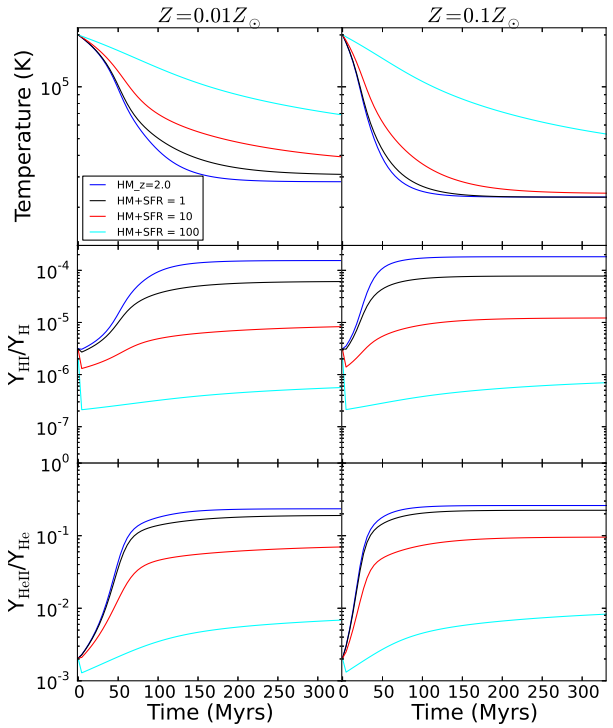

Figure 5.6 The effect of various star formation radiation fields on a parcel of gas with $n_H = 0.001$ cm^{-3} density. The gas cooling time and equilibrium temperatures increase significantly even for a high metallicity gas due to the presence of high energy x-ray photons.

Fig. 5.7 shows the evolution of the same particles in the old star radiation field. Old stars have a smaller effect than young stars that include X-rays, especially in high metallicity gas. The HeII fractions (bottom panels) are systematically lower in the old star radiation field (Fig. 5.7) than in the young star field (Fig. 5.6) because the flux at energies just above the helium ionizing edge is higher. While old stars ionize helium, they do not fully ionize metals, so the gas cools faster at high metallicities than it does in young star radiation field.

5.6 Cosmological simulation using local photoionization feedback

We want to study the effect of local ionizing radiation on the whole process of galaxy formation in a cosmological context. For this purpose, we implement local photoionization feedback in GASOLINE (Wadsley et al. 2004, see also Chapter 1).

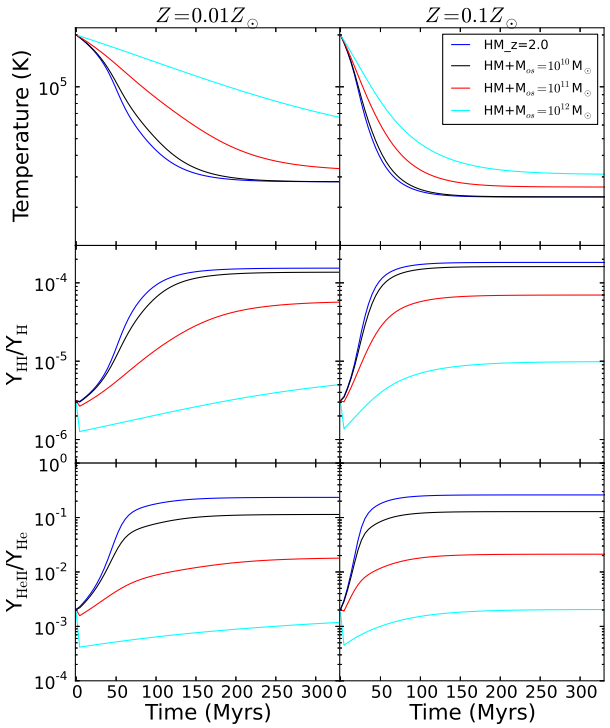

Figure 5.7 Same as Fig. 5.6, but in the radiation field created by old (>200 Myr) stellar populations of 3 different masses. The cooling time and the equilibrium temperature increases in the presence of a local radiation field from old stars, although not to such as extent as in radiation field from star formation.

5.6.1 Simulation physics

We select a galaxy from the McMaster Unbiased Galaxy Simulations (MUGS, Stinson et al. 2010) that has a halo mass of 6.4×10^{11} M$_\odot$. With the feedback prescription used in Stinson et al. (2013b) (see §4.2 for more details), the star formation rate of the galaxy increases steadily to 12 M$_\odot$ yr^{-1} at $z = 0$. This galaxy was chosen to show the maximium effect of the local photoionization field. The galaxy has a gas mass resolution of 2×10^5 M$_\odot$ with a gravitational force softening of 310 pc.

The star formation and feedback model is the same as the fiducial simulation from the Stinson et al. (2013b) parameter study. The star formation efficiency, $c^\star$, is 0.1, and the density threshold is 9.3 cm^{-3}. The star formation and SNe feedback recipes are the same as described in §4.2. We then add our local photoionization feedback to simulation physics. As outlined in §5.3.2, the contribution from stars are summed based on their distance from the gas particle for which we want to compute the incoming radiation. Close sources (stars) are treated as individual sources, while distant one are grouped based on the gravity tree.

We emphasize that the simulations presented here are preliminary. One concern is that we include the radiation energy from young stars twice, both as a photoionization source

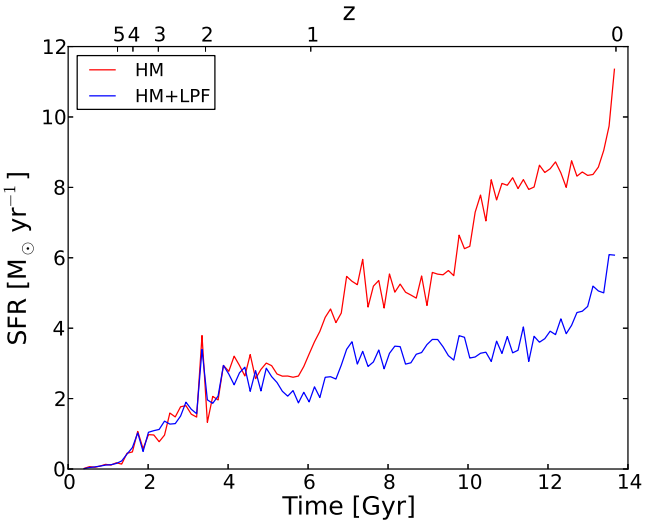

Figure 5.8 A comparison of the star formation histories for the two simulations. The star formation rates are similar until $z \sim 1.5$ and then they begin to diverge.

and as a source of thermal energy for the early stellar feedback. Though the details of the pre-supernova thermal energy input would change, the energy could also be the hot gas created by stellar winds. In future models, we hope to present a more consistent picture. For now, we leave our model as similar as possible to our previous simulations so that the effect of including local photoionizing radiation on the formation of the disc is apparent.

A second concern is that the effect of low energy photons in our simulations may be overestimated because the outer regions of high density gas clouds will shield the inner regions from the radiation field. This 'self-shielding' is important in gas with a density higher than 0.1 cm^{-3} (Ceverino et al., 2013). However, we have shown that the x-ray photons have the largest effect on cooling and these photons have a very small interaction cross section. So, ignoring self-shielding effects may be a reasonable first approximation.

5.6.2 Simulation results

We perform two simulations of the galaxy, one including the HM UV background only (hereafter, HM), and one adding local photoionization feedback (LPF) to the UV background (HM+LPF).

Fig. 5.8 shows the star formation history of the two simulations. The star formation histories are nearly identical until $z \sim 1.5$, after which the they diverge. The star formation rate in the HM run (red curve) steadily increases to 12 M$_\odot$ yr^{-1} at $z = 0$. The HM+LPF simulation (blue curve) maintains a steady star formation rate of $\sim$ 4 M$_\odot$ yr^{-1} from $z = 1.5$ until $z = 0$. The reduced star formation results in $\sim$ 40% less stellar mass than in HM at $z = 0$.

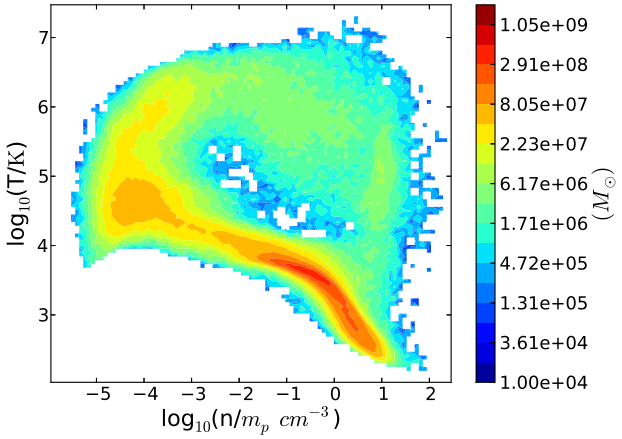

(a) HM

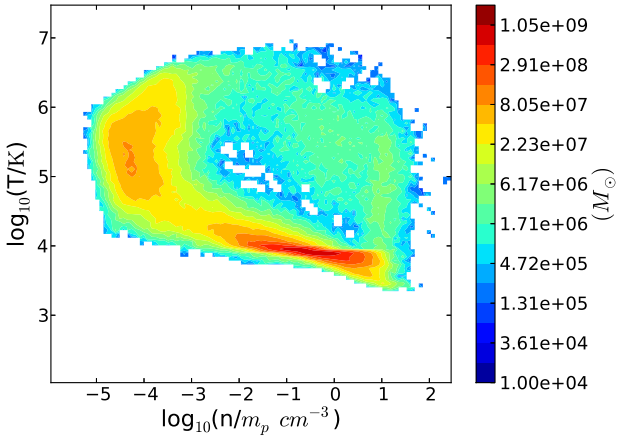

(b) HM+LPF

Figure 5.9 Temperature–density phase space diagrams present in a phase bin, 0.1 dex in temperature by 0.1 dex in density at $z = 0$. Three effects of local photoionization are visible: (i) High density, low temperature gas is absent in the presence of the local radiation field, (ii) The mass of gas accreting from the halo to the disc is reduced (gas channel from top left to bottom right) and (iii) the temperature of the hot halo gas around the galaxy is significantly higher.

To understand the physics behind the lower star formation rate in HM+LPF, Fig. 5.9 shows a comparison of the distribution of the gas in temperature–density phase space of the two simulations at $z = 0$. Three differences are apparent between the simulations: the mean temperature of low density halo gas, the amount of gas cooling out of the halo onto the disc, and the absence of very low temperature gas in the disc of the galaxy. The difference between the hot, diffuse halo gas in the region bounded by 10^5 <T(K)< 10^6 and $log(n/m_p cm^{-3}) < -3.5$ is striking. With local photoionizing feedback (LPF), most of the low density gas mass is between 10^5 and 10^6 K. Without LPF, a large fraction of the halo gas has cooled to a phase that is intermediate between the cool,

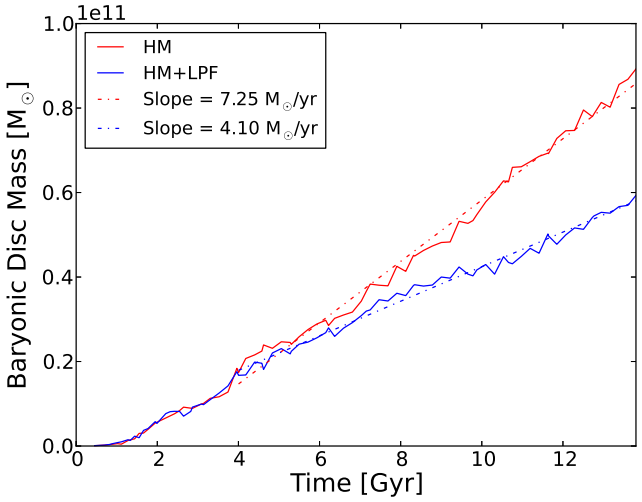

Figure 5.10 The evolution of the baryonic disc mass of the galaxy as a function of time, for the simulations with (blue curve) and without (red curve) local photoionization.

dense disc and the hot, diffuse halo and the gas temperature lies between 10^4 and 10^5 K. Even a small amount of ionizing radiation from the local sources has a big effect on the gas cooling rate, so that gas stays hot longer. The high temperature of the hot halo gas provides pressure support against the galaxy's gravitational potential and hence reduces the gas accretion rate onto the disc. Thus, there is less gas in the region between the hot, low dense halo gas and the cold dense disc in HM+LPF than in HM.

Another factor that causes more cooling in HM is the positive feedback that the metal enrichment from the higher star formation rate in HM causes. HM starts with a marginally higher accretion rate than HM+LPF, which ejects more metals into the hot halo, which cause the gas to cool faster further enhancing the accretion rate, and consequently makes more stars. The higher halo gas temperature indicates the global nature of LPF and underlines the importance of propagating the radiation field from the local sources throughout the entire volume of the simulation box.

Fig. 5.10 shows the reduction in gas accretion rate onto the disc more explicitly. The baryonic disc mass evolves similarly in the two simulations until $\sim$ 4 Gyr when they diverge as HM adds mass at a faster rate, leaving the disc of HM+LPF lighter than HM. The slope of the baryonic disc mass evolution gives a rough gas accretion rate onto the disc (modulo outflows and stellar accretion). The dot-dash line represents a best linear fit of the gas accretion rate after $\sim$ 4 Gyr. For the HM simulation the slope of this line is 7.25 $M_\odot yr^{-1}$, while the HM+LPF simulation has a slope of 4.10 $M_\odot yr^{-1}$.

The increased cooling rate and equilibrium temperature of the halo gas due to LPF affects star formation by reducing the gas accretion onto the disc. This is different from feedback mechanisms local to star forming events that rely on blowing gas out of

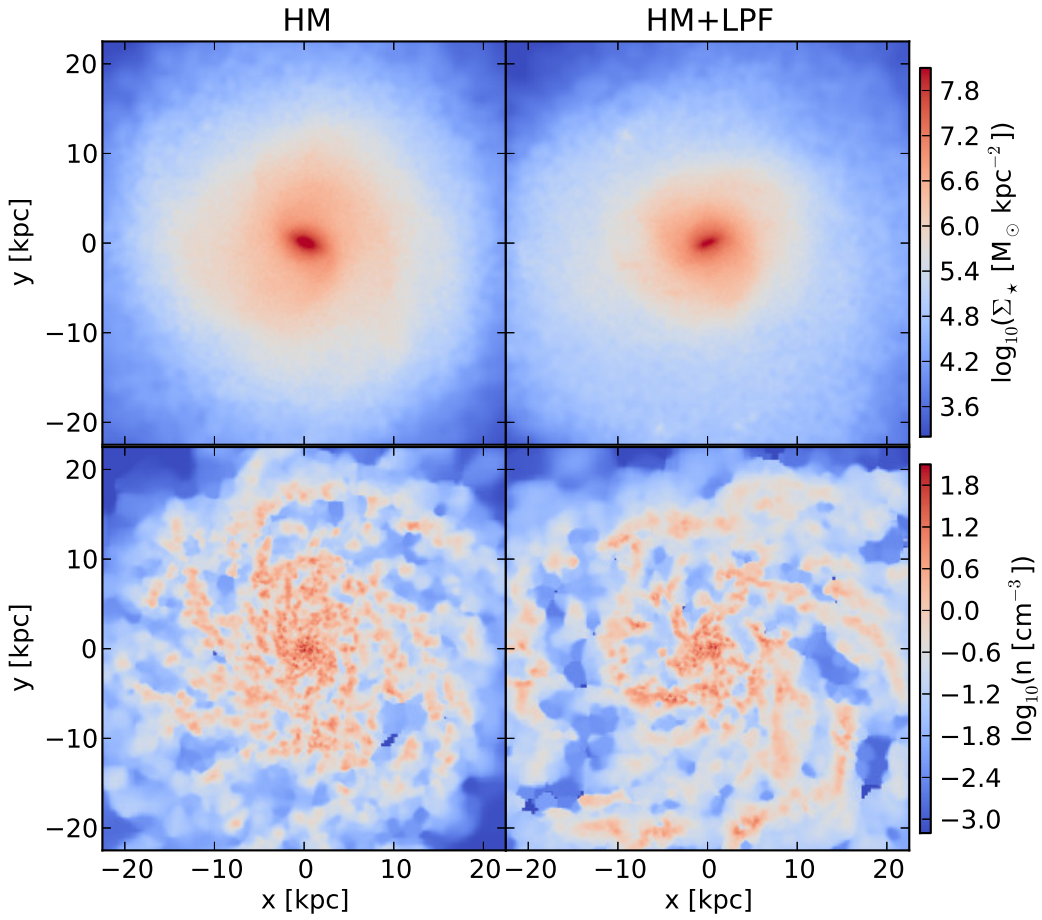

Figure 5.11 The face on projection view of the stellar (top panels) and gaseous (bottom panels) of the MW like galaxy simulations with the HM (left panels) and HM+LPF (right panels) models.

the disc. LPF is rather a *preventive* feedback mechanism which reduces the need for artificially high levels of feedback that can destroy the galaxy disc (Agertz et al. 2011; Roškar et al. 2013). LPF also provides a natural and non-violent mechanism to keep the disc lighter and prevent disc instabilities from driving gas to the center.

Fig. 5.11 shows face-on images of the stellar and gaseous components of the simulated galaxies. The top panels show the stellar distribution and the bottom panels the gas distribution for the HM (left panels) and HM+LPF (right panels) simulations. The HM simulation shows a large stellar bulge and a high concentration of gas in the center. The HM+LPF simulation has a smaller stellar bulge with generally less mass in stars in the disc. The gas distribution in the HM+LPF simulation is more extended and less concentrated than in the HM simulation.

The central concentration of stars and gas in the HM simulation is reflected in the 300 $\mathrm{km\,s^{-1}}$ central peak of the galaxy rotation curve shown in Fig. 5.12. The HM+LPF simulation creates a slowly rising rotation curve that has a rotation velocity of 200

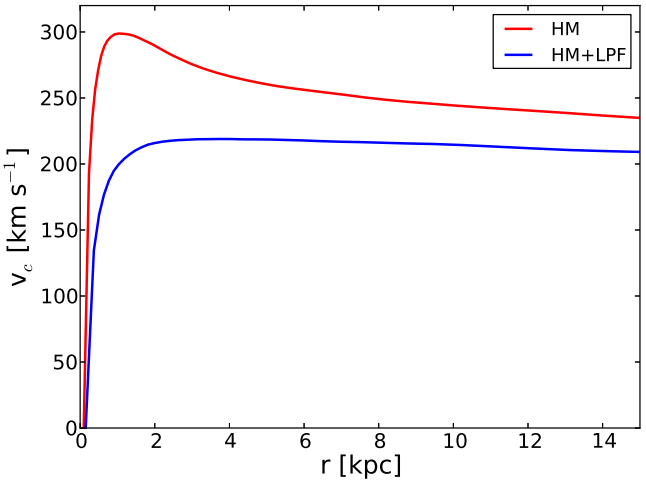

Figure 5.12 The rotation curves of the galaxy in the HM (red) and HM+LPF (blue) runs at $z = 0$.

km s^{-1} from near the center to the edge of the disc, clearly showing that it is much lighter than the HM disc.

The difference in stellar and gaseous distributions and subsequently in the rotation curves can be explained in part due to the reduced gas accretion onto the disc, but also with the reduction in amount of cold gas in the HM+LPF. The HM simulation has a tail of gas at low temperatures (< 1000 K) and high densities ($n > 1$ cm^{-3}). This tail is absent from the HM+LPF run since the additional radiation fields raise the equilibrium temperature of the dense gas. Thus, the average temperature of the disc gas is higher and has higher pressure that stops the disc from fragmenting and forming stars. However, we reiterate that the effect of low energy photons might be overestimated, because we do not impose any criterion for self-shielding in high density gas present in the disc.

5.7 Conclusions

We tested a novel method for including the effects of local photoionizing radiation fields in galaxy formation simulations. Previously, the expense of including detailed radiative transfer meant that simulations that tried to include the effect of photoionization could only be evolved until $z \sim 4$. While such simulations are extremely useful to study the early evolution of the Universe and the reionization epoch they are not able to address the effect of a local radiation field on galaxy evolution. The local radiation field should have a significant importance in regulating how much gas cools onto discs and fuels star formation. Currently, in many simulations, the only radiation field considered is the UV background against which the galaxy might otherwise be self-shielded (Pontzen

et al. 2007; Faucher-Giguère et al. 2009). The local field might be very different from the uniform background and must be included in realistic cosmological simulations of galaxy formation.

Our method uses the existing optimizations that quickly solve gravity to include the r^{-2} attenuation effect. Our current treatment uses the optically thin limit, which provides an upper limit on the effect of radiation. The optically thin approximation is valid for the x-ray photons that we include in our model of the young star radiation field. X-ray photons are not strongly absorbed in typical ISM conditions. However, we will relax the optical thin approximation in future work.

The radiation fields we consider in this work includes the black body emission from young stars, along with the x-rays that massive stars produce in their winds and supernova explosions, as well as UV flux from post-AGB stars in old stellar populations. Our simple treatment of absorption assumes that 5% of the flux around the Lyman limit escapes from clusters of young stars, while old stars have an escape fraction of unity since they likely moved out of their birth cocoons into an optically thinner environment. Otherwise, the radiation field is only attenuated as an inverse square of distance. These physically motivated assumptions allow us to study the effect of a local ionizing radiation field on cooling rates of gas within the galaxy, throughout cosmic time.

As a test of the cooling and to develop physical intuition about how photoionization affects the cooling rate, we provide simple examples of the evolution of a single gas parcel embedded in the radiation field. We show that a radiation field from young stars that includes soft x-rays can increase the equilibrium temperature of the gas significantly and prolong cooling times (Cantalupo, 2010).

We then use our local photoionization scheme in the SPH code GASOLINE to investigate the effect of local ionizing radiation fields in full cosmological simulations of a Milky Way-like galaxy. We simulate the galaxy with and without the local radiation field. We find that the radiation field reduces star formation after $z \sim 1.5$, and results in $\sim$ 40% less stellar mass. The reduced star formation is due to a combination of factors. The hot, diffuse halo gas surrounding the disc has a higher temperature when the local photionizing field is considered because a small amount of ionizing radiation from local sources has a big effect of the gas cooling and heating rates at low densities, which in turn raises the equilibrium temperature of the gas. This increased temperature of the hot halo gas provides pressure support to the halo gas against the gravitational potential of the galaxy and hence reduces the gas accretion rate onto the disc. This coupling of the local radiation field to the gas cooling in the host galaxy provides a *preventive* feedback mechanism that reduces the gas accretion to the central regions of the galaxy, regulating star formation.

The local ionizing radiation field also eliminates high density-low temperature gas by raising the equilibrium temperature of dense gas in the disc. The higher average temperature of the disc gas provides pressure support to the gaseous disc that stops the disc from fragmenting and forming stars. All these effects on the gas distribution by the local radiation field causes the HM+LPF run to form a light and more stable stellar disc, which has a slowly rising rotation curve which peaks at 200 $\mathrm{km\,s^{-1}}$, consistent with observations of Milky Way-like galaxies.

We plan to extend this initial study to a broader galaxy mass range (from dwarfs to massive ellipticals) and to improve the parametrization of our radiative transfer scheme in forthcoming work(s). While this result is still preliminary and based on a single simulation, it shows the importance of self-consistently including local photoionization feedback in simulations aimed at reproducing realistic galaxies.

Chapter 6

Summary and Conclusions

Hydrodynamic simulations are a very powerful tool to study various baryonic processes associated with galaxy formation. In this thesis we have used them to study the various aspects of galaxy formation such as the effect of merger events on the morphology of primary galaxies and the effect of SNe and early stellar feedback on statistical properties of galaxies. We also describe a novel method to include the effect of local ionizing radiation fields on gas cooling calculations in hydrodynamic simulations.

Mergers form an integral part of the paradigm of hierarchical galaxy formation theory. These merger events have the ability to change the morphology of galaxies and also induce star formation. In this thesis we first look at the most minor of merger events (merger ratio of 1:1000). These correspond to interaction between DM sub-haloes and the galactic disc of the primary halo. At such low merger ratios, we do not expect a major change in the morphology of the galaxies, however we entertain the idea that such interactions can trigger the observed holes in the extended HI distributions of nearby galaxies. We create a pre-formed galaxy, with properties matching IC 2574 (our poster-child galaxy), in isolation. Then DM sub-haloes with 1000 times less mass than the primary halo are placed at 5 kpc above the plane of the galactic disc and given a velocity of 150 $\mathrm{km\,s^{-1}}$ pointing vertically downwards. This system is then evolved using the hydrodynamic code GADGET-2 and the effect of the interaction is studied. We find that a pure DM sub-halo (without gas) does not produce holes in the gas distribution of galaxies. As DM particles interact only through gravity, the sub-halo can only focus the gas in a stream behind its path. This leads to the formation of a high density wake in the disc with lasts for about $80 - 90$ Myr.

However when we repeat the same experiment with a very small amount of gas ($\sim 3\%$) added to the sub-halo, the interaction produces a kpc sized low density region in the gas distribution of the galaxy. In addition, these voids are surrounded by an expanding high density shock wave which triggers star formation at the edges of the holes. There is also an increase in velocity of disc particles perpendicular to the disc. The properties

of the holes are dependent on the impact parameters such as the impact velocity, mass of DM sub-halo and amount of gas in the sub-halo. Therefore, we conclude that a small amount of gas seems to be necessary to produce holes. We then tested this scenario in a cosmological setup. The properties and orbits of satellites are extracted form a high resolution cosmological N-body simulation, and then these satellites are given a small amount of gas and allowed to interact with the galactic disc. Over a period of 1 Gyr, the interactions produce about $3-4$ kpc sized holes. This number is significantly lower than the observed number of holes in IC 2574. We therefore conclude that although DM sub-halo, with a small amount of gas, interacting with the disc of the primary galaxy can in principle produce kpc sized holes, this mechanism is not the primary channel through which these holes are formed.

We then looked at the affect of higher merger ratio events from about $1:50$ to $1:1$. These high merger ratio events are thought to impact the morphology of the galaxies. While minor mergers are capable of heating the disc and triggering disc instabilities, major mergers can totally destroy the disc and lead to the formation of elliptical galaxies. We investigate these merger events again using the hydrodynamic simulations code GADGET-2. The initial conditions for simulations such as the properties of interacting galaxies, time of merger and the merger orbits are taken from a Semi-Analytic Model (following the method introduced by Moster et al. 2014). This gives a cosmological framework to the merger events. A library of merger events with different galaxy properties and orbits are simulated using this method from $z = 1$ to $z = 0$. The most important mass transfer channels during the merger , like the amount of satellite mass transferred to the central bulge, the amount of central stellar disc mass given the central bulge, the amount of central gaseous disc mass given to the central bulge and the amount of the central disc mass dispersed out into the stellar halo is tracked throughout the merger event. A robust method which uses the six dimensional phase space of position and velocity is used to decompose the bulge and disc component of the simulated galaxy.

The main result arising from this exercise is that the outcome of a binary galaxy merger depends both on the merger ratio (both DM - μ and baryonic -μ_b) of the two interacting galaxies and on the relative orbit, in particular on the ratio (η) between the orbital angular momentum of the satellite and the angular momentum of a circular orbit with the same energy as the satellite. This two quantities can be combined in the expression (μ; μ_b)/exp(1.9η) (effective merger ratio), which can be conveniently linked to the relevant mass transfer during a merger.

It is seen that in major mergers and in mergers with low η most of the satellite's mass is deposited to the bulge of the central galaxy. Whereas a small satellite in a high angular momentum orbit deposits most of its baryonic mass into the halo before its final coalescence with the central object. The interaction with the incoming satellite will also

cause matter inflows from the central disc to the central bulge. Our results confirm earlier findings that a gas rich disc is more likely to survive a merger event even though the strength of this effect changes when the merger orbit is taken into account. For highly radial satellite orbits, only 50% of the stellar central disc is given to the central bulge even for a $1:1$ merger. A certain fraction (as much as $\sim 35\%$) of the central disc mass is expelled outwards due to close gravitational encounters, thereby increasing the diffuse stellar halo population. This mass transfer is usually not considered in SAMs. We also see an enhanced star formation during a merger event, with most of the excess star formation happening in the central bulges, but a significant enhancement of star formation in the discs of central galaxies is also seen. Larger starbursts are attributed to major mergers. The relative contribution of disc starburst to the overall star formation enhancement is larger for minor mergers or high angular momentum orbits due to the triggering of local instabilities in a minor merger event and global instabilities in a major merger event. Despite the limited sample considered in this paper, our results are indicative of a potentially fundamental revision in our understanding of mass flows involved in a galaxy merger. In a forthcoming work (Fontanot et al., in preparation), we plan to include our fitting formulae in state-of-the-art SAMs, to study the implication of our findings on a cosmologically significant galaxy sample and determine the fraction of bulge versus disc dominated galaxies.

We then shifted the focus of our investigation to the effect of different feedback mechanisms on the properties of galaxies. Particularly we investigated the role of photoheating from massive stars in regulating star formation at high redshifts. It has been shown that this model for photoheating from massive stars (also called Early Stellar Feedback; ESF) works very well for a high resolution $L_\star$ type galaxy (Stinson et al., 2013b). In order to test the effectiveness of ESF across a wide range of galaxy masses, environments and merger histories, a cosmological hydrodynamic simulation of a representative volume of the Universe is performed. The properties of the simulated galaxies are then compared with observed statistical properties of high redshift galaxies like the galaxy stellar mass function, stellar to halo mass relationship, star formation rate, and the number density evolution of low mass galaxies through cosmic time. The use of early stellar feedback is the key difference between our simulation and ones run previously. ESF delays star formation in low mass galaxies and this reproduces many observed statistical properties of high redshift galaxies. At $z \geq 2$, the simulated galaxies match the stellar - halo mass relation and the scatter in the relation is also similar to the observed scatter. The simulated galaxy stellar mass function matches the observed shallow slope at the low mass end, which is a natural by-product of the stellar feedback recipe. However, this feedback is inefficient at the high mass end, seen by the presence of galaxies above the abundance matching stellar-halo mass relation and the lack of an exponential cutoff in the galaxy stellar mass function. The simulated star formation history of the also

matches a variety of different observations. The model predicts that the lowest mass galaxies ($9.5 < log(\mathrm{M}_\star/\mathrm{M}_\odot \leq 10.5$) contribute little to the overall SFR density, while the intermediate ($10.5 < log(\mathrm{M}_\star/\mathrm{M}_\odot \leq 11.5$) and high mass ($log(\mathrm{M}_\star/\mathrm{M}_\odot > 11.5$) galaxies contribute equally up to $z = 3$. After that, the star formation slows down in the highest mass galaxies. The simulated star formation rates lie along a tightly correlated star forming main sequence, and they match observations at $z = 3$ but at $z = 2$, they are below the observed relation. The high specific star formation rates (sSFRs) in low mass haloes at z = 2 suggests that there needs to be a significant amount of cold gas still present in these galaxies at z = 2. Although our model does a better job of delaying the star formation at early times than most Semi-Analytic Models (SAMs) and hydrodynamic simulations, after z = 3 the simulated galaxies are forming too few stars. Previous works have invoked a evolving initial mass function to expalin this discrepancy particularly at $z = 2$. In order to compare the model with observations of the local Universe, a smaller volume of the fiducial run was simulated down to $z = 0$. The stellar-halo mass relation is reproduced at low masses but the over cooling problem still exists at high masses, while in the intermediate mass regime, we are below the relation by a factor of two. We also match the observed star forming main sequence quite well, although we are a bit above the relation throughout the entire mass range. These results indicate that our model does not fare so well at $z = 0$ as at high redshifts but the errors are low when compared to many semi-analytic models and simulations.

The success of our model is due to the early stellar feedback implementation, which decouples the growth of stellar mass from DM mass by effectively blowing the gas away from the disc. This helps regulate the number density of low mass galaxies to the observed values by delaying star formation in these haloes. Our results suggest that stellar feedback is one of the most important factors regulating star formation in low mass galaxies. The most important factor that makes this model successful is the timing of the ESF, because simply increasing and decreasing the feedback energy will only set the normalisation i.e., the total stellar mass of present at z = 0 but does not decouple DM and galaxy mass growth.

Although early stellar feedback is very successful in correctly modelling the star formation of $L_\star$ and sub-$L_\star$ galaxies, the high amount of energy deposited during this form of feedback produces a very thick disc not observed in galaxies. Strong feedback models increases the disc thickness considerably compared to a low feedback models and features like the spiral arms are strongly suppressed. This puts us in a *Catch 22* situation, if the feedback energy is increased then we form the right amount of stars but the disc structure is not reproduced, whereas a model with low feedback energy is able to reproduce the disc structure but forms too many stars. This situation only arises because all feedback models focus on blowing the gas out of the disc or even the galaxy in an

attempt to regulate star formation. However, are these models calculating the amount of gas inflow into the disc correctly?

Radiative cooling controls the infall of gas onto the disc, making it one of the most important processes of galaxy formation. Accurately modeling the cooling rate of halo gas is critical to determining the amount of fuel available for star formation in a galaxy. In addition to gas density and metallicity, the gas cooling rate depends strongly on the ionization state of its component species. The gas ionization state depends on the temperature of the gas and on the incident radiation field from stars, Active Galactic Nuclei (AGN) and other radiation sources. In most galaxy formation models (including numerical hydrodynamical simulations), only a uniform background is used to represent this radiation field. However, within a galaxy, local sources dominate the radiation field. Recently attempts have been made to model photo-heating from massive stars in galaxy formation simulations, but as described in Chapter 4, they have mainly focused on short range photo-heating and creation of ionized HII regions around star formation sites. However, local radiation can effect the cooling rate of halo gas onto the disc and hence, propagating the radiation field out to the halo of the galaxy is important. Previously, the expense of including detailed radiative transfer meant that simulations that tried to include the effect of photoionization could only be evolved until $z \sim 4$. While such simulations are extremely useful to study the early evolution of the Universe and the reionization epoch they are not able to address the dynamical effect of a local radiation field on galaxy evolution.

To this effect we have developed a novel method to include the effects of local radiation field from both young and old stars in hydrodynamical simulations, called local photoionization feedback (LPF), and implemented it in the hydrodynamics code GASOLINE. The local radiation fields considered includes the black body emission from young stars, along with the X-rays from shock heated gas from SNe, as well as UV flux from post-AGB stars. A massive star has high radiation flux at the hydrogen edge but very little above the helium edge. Therefore this kind of spectra can ionize hydrogen, low ionization states on many metals and to a very small extent helium, thereby reducing cooling in low temperature gas ($T < 15000\ K$). The radiation from post-AGB stars has a relatively low flux at the hydrogen edge but the spectra is harder and has significant amount of flux between $4 - 10$ Rydbergs. This spectra in addition to supressing low temperature metal cooling, is also effective is suppressing helium cooling and other low metal ionization ions. However, the maximum suppression in cooling is seen when we include the X-rays from shock heated SNe gas. This spectra has non-negligible flux all the way upto 1500 Ryd. This suppresses cooling in high ionization metal ions and in extreme cases can totally suppress metal line cooling.

In order to keep the calculation computationally efficient, a simple treatment for absorption is assumed in which 5% of the flux around the Lyman limit escapes from clusters of

young stars, while old stars have an escape fraction of unity since they likely moved out of their birth cocoons into an optically thinner environment. Otherwise, the radiation field is only attenuated as an inverse square of distance, and this r^{-2} attenuation is calculated by tagging on to the gravity tree algorithm which efficiently calculates the inverse square gravity forces. These physically motivated assumptions allow us to study the effect of a local ionizing radiation field on cooling rates of gas within the galaxy, throughout cosmic time. Gas cooling is then calculated as a sum of non-equilibrium primordial cooling, calculated on the fly in GASOLINE, plus a equilibrium metal cooling part which is computed using a cooling table which stores equilibrium metal cooling values under different physical gas conditions. Test runs using this method show that local radiation fields can indeed reduce the cooling rate and increase the equilibrium temperature of the gas significantly.

We then tested the effect of local radiation field on the dynamics of galaxy formation by performing two cosmological simulations of a Milky Way like galaxy, one with the gas cooling calculated only in the presence of a spatially constant UV background and another with the background + the local photoionization feedback turned on. We find that the radiation field reduces star formation after $z \sim 1.5$, and results in $\sim 40\%$ lower stellar mass. This is because the radiation field prevents disc instabilities and collapse by increasing the temperature of the gas in the disc, thereby providing additional pressure support. However, the more important effect which directly regulates star formation rate in the galaxy, is the increase in temperature of the hot halo gas. This increased temperature of the hot halo gas provides pressure support against the gravitational potential of the galaxy and hence reduces the gas accretion rate onto the disc. Coupling the local radiation field to gas cooling from the halo provides a preventive feedback mechanism which keeps the central disc light and produces slowly rising rotation curves without resorting to extreme feedback mechanisms. This preliminary result indicates that the effect of local photoionizing sources is significant and should not be ignored in models of galaxy formation.

This state of the art gas cooling implementation in a hydrodynamical galaxy formation code gives us an unique advantage to study the many outstanding problems in astrophysics, like understanding how massive elliptical galaxies exhibit limited star formation over the past 10 Gyr. Current models invoke feedback from AGN to suppress star formation in massive haloes. The theory behind how AGN feedback energy couples to the gas in and around galaxies is still uncertain, so modeling efforts have so far been necessarily crude. Cosmological numerical simulations have cited AGN jets as a form of feedback that is able to heat the entire gas halo to high enough temperatures that prevents gas from cooling onto the disc and forming stars. Quasar absorption line studies probing the gaseous haloes of early-type galaxies find a significant quantity of cool, metal-enriched gas, which seems to contradict the radio-mode model (Thom et al., 2012). Perhaps less

surprising is the fact that galaxies that host quasars have high covering fractions of cool gas in such gaseous haloes including neutral hydrogen (Prochaska et al., 2013; Hennawi & Prochaska, 2013). After all, there must be enough cool gas to fuel the quasars. Thus, with unsatisfying solutions to the problem of how galaxies that are quenched remain quiescent, we plan to use our new method to study the possibility that local radiation sources themselves can quench further star formation through photoionization.

In addition to affecting the dynamics of galaxy formation, the observational diagnostics of gas in galaxies can also be affected by the local radiation field. There have been a variety of circumgalactic halo metal enrichment measurements in recent years. Thom et al. (2012), in their observations of circumgalactic gas in the haloes of early-type galaxies (ETGs) obtained by the COS-halos Survey with the Cosmic Origins Spectrograph on board the Hubble Space Telescope, find that detections of HI surrounding ETGs are typically as common and strong as around star-forming galaxies. However, Tumlinson et al. (2011a) detect ubiquitous, large (150 kiloparsec) haloes of ionized oxygen surrounding star-forming galaxies, but find much less ionized oxygen around galaxies with little or no star formation. These measurements provide an important yardstick, for models of galaxy formation to match. In addition to affecting the dynamics of galaxy formation, the ionization states of the different species present in the gas will be affected by the local radiation field. Hence simulations with LPF is a self consistent way to calculate and predict the abundance and ionization states of elements present in haloes around galaxies.

There is a lot of room for improving the LPF model. The local radiation fields considered in not an exhaustive list. Additional sources which can be considered are X-ray binaries, the cooling radiation from the hot halo of the galaxy and the radiation from AGN. All these sources are observed to have a hard spectra and will be useful in quenching cooling in metal enriched gas. In addition we would also like to improve on the optically thin approximation. Although this is a good initial first guess for hard X-ray photons, a self consistent calculation of the amount of flux absorbed by the intervening gas column needs to developed, preferentially by making use of the already existing tree algorithm. Currently, the optically thin approximation makes the cooling calculation sufficiently simple. However, if we include the frequency dependent absorption, the cooling calculation can get very complex and will become unfeasible to implement. This might mean using the approximations outlined in Gnedin & Hollon (2012). They base their calculations on the assumption of equilibrium cooling. However, as pointed out by Oppenheimer & Schaye (2013a) non-equilibrium metal cooling effects will become important once we start including hard X-ray sources. So extending the non-equilibrium calculation to include dominant metal coolants will become essential.

Appendix A

Equilibrium vs. Non-equilibrium cooling

In many cosmological systems the gas cooling timescale is significantly shorter than the dynamical timescale of the system, therefore one can assume that creation and destruction rates will be balanced for each species, resulting in ionization equilibrium (IE). In IE, the rate of change of the ion species defined in equations 5.4,5.5 and 5.6 is assumed to be zero. This assumption is used to derive the density of each species as described in Katz et al. (1996). The equilibrium assumption decouples the heat equation (Eq. 5.1) from the rate equations (Eqs. 5.4,5.5,5.6) of the individual species, while in reality these equations should be solved together, with the rate equations taking the ionization state of the gas from previous timestep into account.

To illustrate the difference that occurs when we assume equilibrium conditions, we show the temperature evolution of mostly neutral, primordial parcel of gas with a temperature of 8000 K exposed to a constant external heating source of 0.1 erg gm^{-1} s^{-1}, which mimics a sequence of supernovae explosions. Figure A.1 shows the temperature (top panel) and neutral hydrogen fraction evolution (bottom panel) of this gas particle. The example is idealized as this single gas particle remains at a constant density, $n_H = 10^{-3}\mathrm{cm}^{-3}$. Under the assumption of equilibrium cooling (red dot-dashed), the gas ionizes rapidly (< 50 Myr) and quickly increases its temperature. Subsequently, the temperature rises more slowly as the heating is balanced by free-free emission. In the case of non-equilibrium cooling (blue), the primordial gas initially rises to a temperature of $\sim 30,000$ K and the gas remains largely neutral. It maintains this temperature for ~ 200 Myr as the heat source ionizes the gas. Only once the gas is mostly (90%) ionized can it rapidly heat. This isothermal phase seen in non-equilibrium calculations represents a striking difference in the thermal evolution of gas. Using the equilibrium assumption artificially boosts the effect of feedback by underestimating the time it takes for an external heat source to heat the gas.

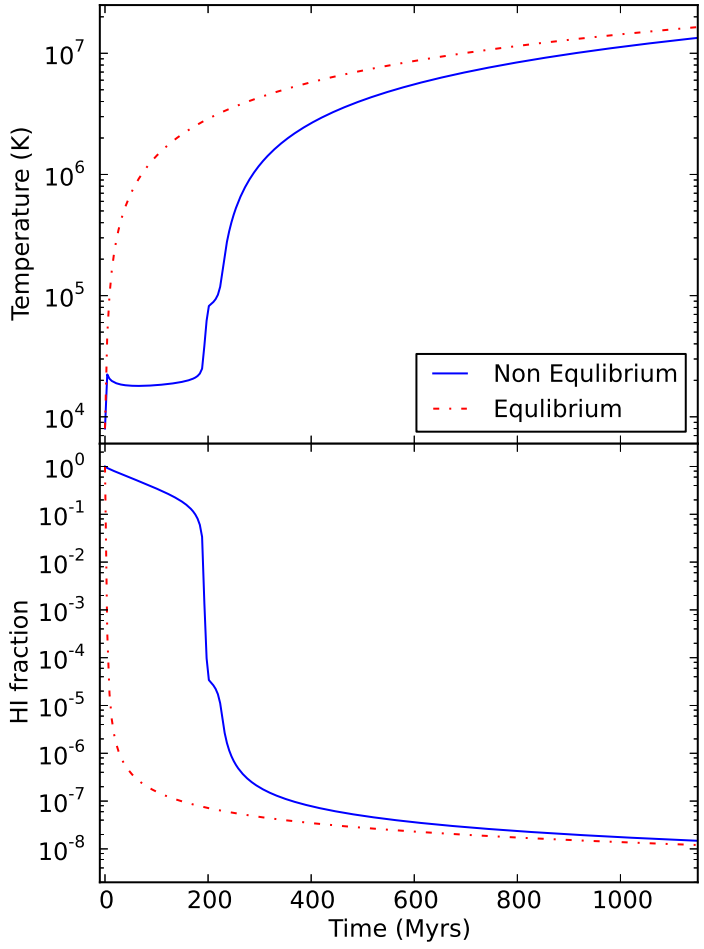

Figure A.1 The evolution of temperature (top panel) and the neutral hydrogen fraction (bottom panel) with time of a parcel of gas ($n_H = 0.001\text{cm}^{-3}$), assuming equilibrium (red dot-dashed curve) and non-equilibrium (blue curve). The single gas particle starts at 8000 K and is constantly heated at the rate of 0.1 erg gm^{-1} s^{-1}.

Bibliography

Agertz O., Kravtsov A. V., Leitner S. N., Gnedin N. Y., 2013, ApJ, 770, 25

Agertz O., Teyssier R., Moore B., 2011, MNRAS, 410, 1391

Ahn C. P. et al., 2014, ApJS, 211, 17

Alongi M., Bertelli G., Bressan A., Chiosi C., Fagotto F., Greggio L., Nasi E., 1993, A&AS, 97, 851

Alpher R. A., Bethe H., Gamow G., 1948, Physical Review, 73, 803

Alpher R. A., Herman R. C., 1948, Physical Review, 74, 1737

Altay G., Croft R. A. C., Pelupessy I., 2008, MNRAS, 386, 1931

Altay G., Theuns T., 2013, MNRAS, 434, 748

Anderson M. E., Bregman J. N., Dai X., 2013, ApJ, 762, 106

Anninos P., Zhang Y., Abel T., Norman M. L., 1997, New Astronomy, 2, 209

Appel A. W., 1985, SIAM Journal on Scientific and Statistical Computing, vol. 6, no. 1, January 1985, p. 85-103., 6, 85

Barnes J., Efstathiou G., 1987, ApJ, 319, 575

Barnes J., Hut P., 1986, Nature, 324, 446

Bate M. R., Burkert A., 1997, MNRAS, 288, 1060

Behroozi P. S., Conroy C., Wechsler R. H., 2010, ApJ, 717, 379

Behroozi P. S., Wechsler R. H., Conroy C., 2013a, ApJL, 762, L31

Behroozi P. S., Wechsler R. H., Conroy C., 2013b, ApJ, 770, 57

Bekki K., Chiba M., 2006, ApJL, 637, L97

Benson A. J., Bower R. G., Frenk C. S., Lacey C. G., Baugh C. M., Cole S., 2003, ApJ, 599, 38

Bergvall N., Zackrisson E., Andersson B.-G., Arnberg D., Masegosa J., Östlin G., 2006, A&A, 448, 513

Bertschinger E., Gelb J. M., 1991, Computers in Physics, 5, 164

Binney J., 1977, ApJ, 215, 483

Blandford R. D., Znajek R. L., 1977, MNRAS, 179, 433

Bondi H., 1952, MNRAS, 112, 195

Bondi H., Hoyle F., 1944, MNRAS, 104, 273

Borissova J., Kurtev R., Georgiev L., Rosado M., 2004, A&A, 413, 889

Bouché N. et al., 2010, ApJ, 718, 1001

Bouwens R. et al., 2012, arXiv:1211.2230

Bouwens R. J. et al., 2011, ApJ, 737, 90

Bower R. G., Benson A. J., Crain R. A., 2012, MNRAS, 422, 2816

Bower R. G., Benson A. J., Malbon R., Helly J. C., Frenk C. S., Baugh C. M., Cole S., Lacey C. G., 2006, MNRAS, 370, 645

Boylan-Kolchin M., Ma C.-P., Quataert E., 2008, MNRAS, 383, 93

Brandt A., Lubrecht A. A., 1990, Journal of Computational Physics, 90, 348

Bressan A., Fagotto F., Bertelli G., Chiosi C., 1993, A&AS, 100, 647

Brinchmann J., Charlot S., White S. D. M., Tremonti C., Kauffmann G., Heckman T., Brinkmann J., 2004, MNRAS, 351, 1151

Brinks E., 1981, A&A, 95, L1

Brinks E., Bajaja E., 1986, A&A, 169, 14

Brook C. B. et al., 2011, MNRAS, 415, 1051

Brook C. B., Stinson G., Gibson B. K., Shen S., Macciò A. V., Wadsley J., Quinn T., 2013, ArXiv e-prints

Brook C. B., Stinson G., Gibson B. K., Wadsley J., Quinn T., 2012, MNRAS, 424, 1275

Bruzual G., Charlot S., 2003, MNRAS, 344, 1000

Cannon J. M. et al., 2011, ApJ, 735, 36

Cantalupo S., 2010, MNRAS, 403, L16

Cavaliere A., Fusco-Femiano R., 1976, A&A, 49, 137

Cen R., 1992, ApJS, 78, 341

Cerviño M., Mas-Hesse J. M., Kunth D., 2002, A&A, 392, 19

Ceverino D., Klypin A., Klimek E., Trujillo-Gomez S., Churchill C. W., Primack J., Dekel A., 2013, ArXiv e-prints

Chabrier G., 2003, PASP, 115, 763

Chakrabarti S., Blitz L., 2009, MNRAS, 399, L118

Chakrabarti S., Blitz L., 2011, ApJ, 731, 40

Chang J., Macciò A. V., Kang X., 2013, MNRAS

Chang P., Chakrabarti S., 2011, ArXiv e-prints

Code A. D., 1969, PASP, 81, 475

Conroy C., Wechsler R. H., 2009, ApJ, 696, 620

Conroy C., Wechsler R. H., Kravtsov A. V., 2006, ApJ, 647, 201

Couchman H. M. P., 1991, ApJL, 368, L23

Cox T. J., Dutta S. N., Di Matteo T., Hernquist L., Hopkins P. F., Robertson B., Springel V., 2006a, ApJ, 650, 791

Cox T. J., Jonsson P., Primack J. R., Somerville R. S., 2006b, MNRAS, 373, 1013

Cox T. J., Jonsson P., Somerville R. S., Primack J. R., Dekel A., 2008, MNRAS, 384, 386

Crain R. A. et al., 2009, MNRAS, 399, 1773

Croton D. J. et al., 2006, MNRAS, 365, 11

Cucciati O. et al., 2012, A&A, 539, A31

Curtis H. D., 1920, JRASC, 14, 317

Daddi E. et al., 2007, ApJ, 670, 156

Dalla Vecchia C., Schaye J., 2008, MNRAS, 387, 1431

Dalla Vecchia C., Schaye J., 2012, MNRAS, 426, 140

Damen M., Förster Schreiber N. M., Franx M., Labbé I., Toft S., van Dokkum P. G., Wuyts S., 2009, ApJ, 705, 617

Davé R., 2008, MNRAS, 385, 147

Davé R., Finlator K., Oppenheimer B. D., 2011a, MNRAS, 416, 1354

Davé R., Oppenheimer B. D., Finlator K., 2011b, MNRAS, 415, 11

Davies R. L., Illingworth G., 1983, ApJ, 266, 516

De Lucia G., Boylan-Kolchin M., Benson A. J., Fontanot F., Monaco P., 2010, MNRAS, 406, 1533

De Lucia G., Fontanot F., Wilman D., Monaco P., 2011, MNRAS, 414, 1439

De Lucia G., Springel V., White S. D. M., Croton D., Kauffmann G., 2006, MNRAS, 366, 499

de Vaucouleurs G., 1948, Annales d'Astrophysique, 11, 247

Dekel A., Silk J., 1986, ApJ, 303, 39

Deul E. R., den Hartog R. H., 1990, A&A, 229, 362

Di Matteo T., Springel V., Hernquist L., 2005, Nature, 433, 604

Diemand J., Kuhlen M., Madau P., 2007, ApJ, 667, 859

Dodelson S., 2003, Modern cosmology

Duffell P. C., MacFadyen A. I., 2011, ApJS, 197, 15

Dunne L. et al., 2009, MNRAS, 394, 3

Dutton A. A. et al., 2013, MNRAS, 428, 3183

Dutton A. A., van den Bosch F. C., Dekel A., 2010, MNRAS, 405, 1690

Edgar R., 2004, New Astronomy Reviews, 48, 843

Efremov Y. N., Elmegreen B. G., Hodge P. W., 1998, ApJL, 501, L163+

Efstathiou G., 1992, MNRAS, 256, 43P

Einstein A., 1917, Sitzungsberichte der Königlich Preußischen Akademie der Wissenschaften (Berlin), Seite 142-152., 142

Einstein A., de Sitter W., 1932, Proceedings of the National Academy of Science, 18, 213

Eke V. R., Navarro J. F., Frenk C. S., 1998, ApJ, 503, 569

Elbaz D. et al., 2007, A&A, 468, 33

Fall S. M., Efstathiou G., 1980, MNRAS, 193, 189

Fanidakis N., Baugh C. M., Benson A. J., Bower R. G., Cole S., Done C., Frenk C. S., 2011, MNRAS, 410, 53

Faucher-Giguère C.-A., Lidz A., Zaldarriaga M., Hernquist L., 2009, ApJ, 703, 1416

Ferland G. J., Korista K. T., Verner D. A., Ferguson J. W., Kingdon J. B., Verner E. M., 1998, Publ. Astron. Soc. Pac., 110, 761

Folkes S. et al., 1999, MNRAS, 308, 459

Font A. S. et al., 2011, MNRAS, 417, 1260

Fontanot F., De Lucia G., Monaco P., Somerville R. S., Santini P., 2009, MNRAS, 397, 1776

Fontanot F., De Lucia G., Wilman D., Monaco P., 2011, MNRAS, 416, 409

Freeman K. C., 1970, ApJ, 160, 811

Fumagalli M., Prochaska J. X., Kasen D., Dekel A., Ceverino D., Primack J. R., 2011, MNRAS, 418, 1796

Gadotti D. A., 2009, MNRAS, 393, 1531

Geller M. J., Huchra J. P., 1989, Science, 246, 897

Gerritsen J., Icke V., 1997, in Revista Mexicana de Astronomia y Astrofisica Conference Series, Vol. 6, Revista Mexicana de Astronomia y Astrofisica Conference Series, Franco J., Terlevich R., Serrano A., eds., p. 261

Gingold R. A., Monaghan J. J., 1977, MNRAS, 181, 375

Gnat O., Ferland G. J., 2012, ApJS, 199, 20

Gnedin N. Y., 2008, ApJL, 673, L1

Gnedin N. Y., Hollon N., 2012, ApJS, 202, 13

González V., Labbé I., Bouwens R. J., Illingworth G., Franx M., Kriek M., Brammer G. B., 2010, ApJ, 713, 115

Gould H., Tobochnik J., 1988, An introduction to computer simulation methods

Governato F. et al., 2010, Nature, 463, 203

Grimes J. P. et al., 2009, ApJS, 181, 272

Grimm H.-J., Gilfanov M., Sunyaev R., 2003, MNRAS, 339, 793

Guedes J., Callegari S., Madau P., Mayer L., 2011, ApJ, 742, 76

Guo Q. et al., 2011, MNRAS, 413, 101

Guo Q., White S., Li C., Boylan-Kolchin M., 2010, MNRAS, 404, 1111

Haardt F., Madau P., 1996, ApJ, 461, 20

Haardt F., Madau P., 2012, ApJ, 746, 125

Hansen S. H., Macció A. V., Romano-Diaz E., Hoffman Y., Brüggen M., Scannapieco E., Stinson G. S., 2011, ApJ, 734, 62

Hatzidimitriou D., Stanimirovic S., Maragoudaki F., Staveley-Smith L., Dapergolas A., Bratsolis E., 2005, MNRAS, 360, 1171

Heckman T. M., Dahlem M., Lehnert M. D., Fabbiano G., Gilmore D., Waller W. H., 1995, ApJ, 448, 98

Heiles C., 1979, PASP, 91, 611

Heiles C., 1984, ApJS, 55, 585

Hennawi J. F., Prochaska J. X., 2013, APJ, 766, 58

Hernquist L., 1990, ApJ, 356, 359

Hernquist L., Katz N., 1989, ApJS, 70, 419

Hopkins A. M., 2004, ApJ, 615, 209

Hopkins P. F., Cox T. J., Younger J. D., Hernquist L., 2009a, ApJ, 691, 1168

Hopkins P. F., Quataert E., Murray N., 2011, MNRAS, 417, 950

Hopkins P. F. et al., 2009b, MNRAS, 397, 802

Hubble E., 1929a, Proceedings of the National Academy of Science, 15, 168

Hubble E. P., 1925, Popular Astronomy, 33, 252

Hubble E. P., 1926, ApJ, 64, 321

Hubble E. P., 1929b, ApJ, 69, 103

Iliev I. T. et al., 2009, MNRAS, 400, 1283

Jimenez R., Flynn C., MacDonald J., Gibson B. K., 2003, Science, 299, 1552

Johansson P. H., Naab T., Ostriker J. P., 2009, ApJL, 697, L38

Jones C., Forman W., 1984, ApJ, 276, 38

Kajisawa M., Ichikawa T., Yamada T., Uchimoto Y. K., Yoshikawa T., Akiyama M., Onodera M., 2010, ApJ, 723, 129

Kamphuis J., Sancisi R., van der Hulst T., 1991, A&A, 244, L29

Kamphuis J. J., 1993, Neutral hydrogen in nearby spiral galaxies, holes and high velocity clouds

Kannan R., Macciò A. V., Pasquali A., Moster B. P., Walter F., 2012, ApJ, 746, 10

Kannan R., Stinson G. S., Macciò A. V., Brook C., Weinmann S. M., Wadsley J., Couchman H. M. P., 2014a, MNRAS, 437, 3529

Kannan R. et al., 2014b, MNRAS, 437, 2882

Karim A. et al., 2011, ApJ, 730, 61

Katz N., 1992, ApJ, 391, 502

Katz N., Gunn J. E., 1991, ApJ, 377, 365

Katz N., Weinberg D. H., Hernquist L., 1996, ApJS, 105, 19

Katz N., White S. D. M., 1993, ApJ, 412, 455

Kauffmann G., White S. D. M., Guiderdoni B., 1993, MNRAS, 264, 201

Kaviraj S. et al., 2007, ApJS, 173, 619

Kawata D., Gibson B. K., 2003, MNRAS, 340, 908

Kazantzidis S., Bullock J. S., Zentner A. R., Kravtsov A. V., Moustakas L. A., 2008, ApJ, 688, 254

Kennicutt, Jr. R. C., 1998, ApJ, 498, 541

Kim S., Dopita M. A., Staveley-Smith L., Bessell M. S., 1999, AJ, 118, 2797

Kim S., Staveley-Smith L., Dopita M. A., Freeman K. C., Sault R. J., Kesteven M. J., McConnell D., 1998, ApJ, 503, 674

Komatsu E. et al., 2011, ApJS, 192, 18

Kormendy J., Drory N., Bender R., Cornell M. E., 2010, ApJ, 723, 54

Kroupa P., 2001, MNRAS, 322, 231

Krumholz M. R., Dekel A., 2012, ApJ, 753, 16

Krumholz M. R., Leroy A. K., McKee C. F., 2011, ApJ, 731, 25

Lacey C., Cole S., 1993, MNRAS, 262, 627

Larson D. et al., 2011, ApJS, 192, 16

Larson R. B., 1974, MNRAS, 169, 229

Leavitt H. S., 1908, Annals of Harvard College Observatory, 60, 87

Lee K.-S. et al., 2012, ApJ, 752, 66

Leitherer C. et al., 1999, ApJS, 123, 3

Leroy A. K., Walter F., Brinks E., Bigiel F., de Blok W. J. G., Madore B., Thornley M. D., 2008, AJ, 136, 2782

Li C., White S. D. M., 2009, MNRAS, 398, 2177

Li Y. et al., 2007, ApJ, 665, 187

Lilly S. J., Le Fevre O., Hammer F., Crampton D., 1996, ApJL, 460, L1

Loeb A., Perna R., 1998, ApJL, 503, L35+

Lopez L. A., Krumholz M. R., Bolatto A. D., Prochaska J. X., Ramirez-Ruiz E., 2011, ApJ, 731, 91

Lucy L. B., 1977, AJ, 82, 1013

Ly C., Lee J. C., Dale D. A., Momcheva I., Salim S., Staudaher S., Moore C. A., Finn R., 2011, ApJ, 726, 109

Macciò A. V., Dutton A. A., van den Bosch F. C., 2008, MNRAS, 391, 1940

Macciò A. V., Dutton A. A., van den Bosch F. C., Moore B., Potter D., Stadel J., 2007, MNRAS, 378, 55

Macciò A. V., Kang X., Fontanot F., Somerville R. S., Koposov S., Monaco P., 2010, MNRAS, 402, 1995

Macciò A. V., Stinson G., Brook C. B., Wadsley J., Couchman H. M. P., Shen S., Gibson B. K., Quinn T., 2012, ApJL, 744, L9

Madau P., Ferguson H. C., Dickinson M. E., Giavalisco M., Steidel C. C., Fruchter A., 1996, MNRAS, 283, 1388

Makino N., Sasaki S., Suto Y., 1998, ApJ, 497, 555

Marchesini D., van Dokkum P. G., Förster Schreiber N. M., Franx M., Labbé I., Wuyts S., 2009, ApJ, 701, 1765

Marinacci F., Pakmor R., Springel V., 2014, MNRAS, 437, 1750

Martin C. L., 2005, ApJ, 621, 227

McCarthy I. G., Schaye J., Font A. S., Theuns T., Frenk C. S., Crain R. A., Dalla Vecchia C., 2012, MNRAS, 427, 379

Mihos J. C., Hernquist L., 1996, ApJ, 464, 641

Mo H. J., Mao S., White S. D. M., 1998, MNRAS, 295, 319

Monaco P., Fontanot F., Taffoni G., 2007, MNRAS, 375, 1189

Monaco P., Theuns T., Taffoni G., 2002, MNRAS, 331, 587

Monaghan J. J., 1992, ARAA, 30, 543

Moster B. P., Macciò A. V., Somerville R. S., 2014, MNRAS, 437, 1027

Moster B. P., Macciò A. V., Somerville R. S., Johansson P. H., Naab T., 2010a, MNRAS, 403, 1009

Moster B. P., Macciò A. V., Somerville R. S., Naab T., Cox T. J., 2011, MNRAS, 415, 3750

Moster B. P., Macciò A. V., Somerville R. S., Naab T., Cox T. J., 2012, MNRAS, 423, 2045

Moster B. P., Naab T., White S. D. M., 2013, MNRAS, 428, 3121

Moster B. P., Somerville R. S., Maulbetsch C., van den Bosch F. C., Macciò A. V., Naab T., Oser L., 2010b, ApJ, 710, 903

Munshi F. et al., 2013, ApJ, 766, 56

Murray N., Ménard B., Thompson T. A., 2011, ApJ, 735, 66

Murray N., Quataert E., Thompson T. A., 2010, ApJ, 709, 191

Navarro J. F., Benz W., 1991, ApJ, 380, 320

Navarro J. F., Frenk C. S., White S. D. M., 1995, MNRAS, 275, 56

Navarro J. F., Frenk C. S., White S. D. M., 1997, ApJ, 490, 493

Navarro J. F., Steinmetz M., 1997, ApJ, 478, 13

Neistein E., Macciò A. V., Dekel A., 2010, MNRAS, 403, 984

Nestor D. B., Shapley A. E., Kornei K. A., Steidel C. C., Siana B., 2013, ApJ, 765, 47

Noeske K. G. et al., 2007, ApJL, 660, L43

Oey M. S., Clarke C. J., 1997, MNRAS, 289, 570

Okamoto T., Eke V. R., Frenk C. S., Jenkins A., 2005, MNRAS, 363, 1299

Okamoto T., Gao L., Theuns T., 2008, MNRAS, 390, 920

Oppenheimer B. D., Davé R., 2006, MNRAS, 373, 1265

Oppenheimer B. D., Davé R., 2008, MNRAS, 387, 577

Oppenheimer B. D., Davé R., Kereš D., Fardal M., Katz N., Kollmeier J. A., Weinberg D. H., 2010, MNRAS, 406, 2325

Oppenheimer B. D., Schaye J., 2013a, MNRAS, 434, 1063

Oppenheimer B. D., Schaye J., 2013b, MNRAS, 434, 1043

Ostriker J. P., Peebles P. J. E., 1973, ApJ, 186, 467

Ott J., Walter F., Brinks E., Van Dyk S. D., Dirsch B., Klein U., 2001, AJ, 122, 3070

Owen R. A., Warwick R. S., 2009, MNRAS, 394, 1741

Pannella M. et al., 2009, ApJL, 698, L116

Pasquali A. et al., 2008, ApJ, 687, 1004

Pawlik A. H., Schaye J., 2008, MNRAS, 389, 651

Peñarrubia J., Navarro J. F., McConnachie A. W., 2008, ApJ, 673, 226

Peacock J. A., Smith R. E., 2000, MNRAS, 318, 1144

Pellegrini E. W., Baldwin J. A., Ferland G. J., 2011, ApJ, 738, 34

Peng Y.-j. et al., 2010, ApJ, 721, 193

Penzias A. A., Wilson R. W., 1965, ApJ, 142, 419

Perlmutter S. et al., 1999, ApJ, 517, 565

Perna R., Gaensler B. M., 2004, ApJ, 606, 326

Persic M., Rephaeli Y., Braito V., Cappi M., Della Ceca R., Franceschini A., Gruber D. E., 2004, A&A, 419, 849

Petkova M., Springel V., 2011, MNRAS, 412, 935

Planck Collaboration et al., 2013, ArXiv e-prints

Pontzen A., Hewett P., Carswell R., Wild V., 2007, MNRAS, 381, L99

Press W. H., Schechter P., 1974, ApJ, 187, 425

Price D. J., 2007, PASA, 24, 159

Prochaska J. X., Hennawi J. F., Simcoe R. A., 2013, ApJL, 762, L19

Puche D., Westpfahl D., Brinks E., Roy J., 1992, AJ, 103, 1841

Puchwein E., Springel V., 2013, MNRAS, 428, 2966

Rahmati A., Schaye J., Pawlik A. H., Raicevic M., 2013, MNRAS, 431, 2261

Rasmussen J., Ponman T. J., 2009, MNRAS, 399, 239

Read J. I., Hayfield T., 2012, MNRAS, 422, 3037

Reed D., Governato F., Quinn T., Gardner J., Stadel J., Lake G., 2005, MNRAS, 359, 1537

Rees M. J., 1986, MNRAS, 218, 25P

Rees M. J., Ostriker J. P., 1977, MNRAS, 179, 541

Rhode K. L., Salzer J. J., Westpfahl D. J., Radice L. A., 1999, AJ, 118, 323

Riess A. G. et al., 1998, AJ, 116, 1009

Robertson B., Bullock J. S., Cox T. J., Di Matteo T., Hernquist L., Springel V., Yoshida N., 2006, ApJ, 645, 986

Robertson B., Yoshida N., Springel V., Hernquist L., 2004, ApJ, 606, 32

Robertson H. P., 1935, ApJ, 82, 284

Robotham A. S. G., Driver S. P., 2011, MNRAS, 413, 2570

Roll P. G., Wilkinson D. T., 1966, Physical Review Letters, 16, 405

Roškar R., Teyssier R., Agertz O., Wetzstein M., Moore B., 2013, ArXiv e-prints

Rubin V. C., Peterson C. J., Ford, Jr. W. K., 1980, ApJ, 239, 50

Rujopakarn W. et al., 2010, ApJ, 718, 1171

Salim S. et al., 2007, ApJS, 173, 267

Santini P. et al., 2012, A&A, 538, A33

Sawala T., Guo Q., Scannapieco C., Jenkins A., White S., 2011, MNRAS, 413, 659

Schaye J., Dalla Vecchia C., 2008, MNRAS, 383, 1210

Schmidt M., 1959, ApJ, 129, 243

Shapley A. E., Steidel C. C., Pettini M., Adelberger K. L., Erb D. K., 2006, ApJ, 651, 688

Shapley H., 1919, PASP, 31, 261

Shen S., Wadsley J., Stinson G., 2010, MNRAS, 407, 1581

Sheth R. K., Mo H. J., Tormen G., 2001, MNRAS, 323, 1

Sheth R. K., Tormen G., 2004, MNRAS, 350, 1385

Siana B. et al., 2007, ApJ, 668, 62

Sijacki D., Springel V., Di Matteo T., Hernquist L., 2007, MNRAS, 380, 877

Silich S., Lozinskaya T., Moiseev A., Podorvanuk N., Rosado M., Borissova J., Valdez-Gutierrez M., 2006, A&A, 448, 123

Silk J., 1977, ApJ, 211, 638

Simpson C. E., Hunter D. A., Knezek P. M., 2005, AJ, 129, 160

Smith S., 1936, ApJ, 83, 23

Smolčić V. et al., 2009, ApJ, 690, 610

Somerville R. S., Primack J. R., 1999, MNRAS, 310, 1087

Sommer-Larsen J., 2006, ApJL, 644, L1

Spergel D. N. et al., 2007, ApJS, 170, 377

Springel V., 2005, MNRAS, 364, 1105

Springel V., 2010a, MNRAS, 401, 791

Springel V., 2010b, ARAA, 48, 391

Springel V., Di Matteo T., Hernquist L., 2005a, MNRAS, 361, 776

Springel V., Frenk C. S., White S. D. M., 2006, Nature, 440, 1137

Springel V., Hernquist L., 2002, MNRAS, 333, 649

Springel V., Hernquist L., 2003, MNRAS, 339, 289

Springel V. et al., 2008, MNRAS, 391, 1685

Springel V. et al., 2005b, Nature, 435, 629

Stadel J. G., 2001, PhD thesis, UNIVERSITY OF WASHINGTON

Stark D. P., Ellis R. S., Bunker A., Bundy K., Targett T., Benson A., Lacy M., 2009, ApJ, 697, 1493

Stark D. P., Schenker M. A., Ellis R., Robertson B., McLure R., Dunlop J., 2013, ApJ, 763, 129

Staveley-Smith L., Sault R. J., Hatzidimitriou D., Kesteven M. J., McConnell D., 1997, MNRAS, 289, 225

Steidel C. C., Pettini M., Adelberger K. L., 2001, ApJ, 546, 665

Stewart S. G., Walter F., 2000, AJ, 120, 1794

Stinson G., Seth A., Katz N., Wadsley J., Governato F., Quinn T., 2006, MNRAS, 373, 1074

Stinson G. S., Bailin J., Couchman H., Wadsley J., Shen S., Nickerson S., Brook C., Quinn T., 2010, MNRAS, 408, 812

Stinson G. S. et al., 2013a, MNRAS, 436, 625

Stinson G. S., Brook C., Macciò A. V., Wadsley J., Quinn T. R., Couchman H. M. P., 2013b, MNRAS, 428, 129

Stinson G. S. et al., 2012, MNRAS, 425, 1270

Stone J. M., Norman M. L., 1992, ApJS, 80, 753

Strickland D. K., Heckman T. M., Colbert E. J. M., Hoopes C. G., Weaver K. A., 2004, ApJS, 151, 193

Taffoni G., Mayer L., Colpi M., Governato F., 2003, MNRAS, 341, 434

Tenorio-Tagle G., Bodenheimer P., 1988, ARAA, 26, 145

Tenorio-Tagle G., Franco J., Bodenheimer P., Rozyczka M., 1987, A&A, 179, 219

Teyssier R., 2002, A&A, 385, 337

Thacker R. J., Couchman H. M. P., 2000, ApJ, 545, 728

Thom C. et al., 2012, ApJL, 758, L41

Toomre A., 1964, ApJ, 139, 1217

Toomre A., Toomre J., 1972, ApJ, 178, 623

Tumlinson J. et al., 2011a, Science, 334, 948

Tumlinson J. et al., 2011b, ApJ, 733, 111

van den Bosch F. C., Abel T., Croft R. A. C., Hernquist L., White S. D. M., 2002, ApJ, 576, 21

van den Bosch F. C. et al., 2007, MNRAS, 376, 841

van der Burg R. F. J., Hildebrandt H., Erben T., 2010, A&A, 523, A74

van der Hulst J. M., 1996, in Astronomical Society of the Pacific Conference Series, Vol. 106, The Minnesota Lectures on Extragalactic Neutral Hydrogen, E. D. Skillman, ed., pp. 47–+

Vogelsberger M., Genel S., Sijacki D., Torrey P., Springel V., Hernquist L., 2013, MNRAS, 436, 3031

Wadsley J. W., Stadel J., Quinn T., 2004, New Astronomy, 9, 137

Walter F., Brinks E., 1999, AJ, 118, 273

Walter F., Brinks E., de Blok W. J. G., Bigiel F., Kennicutt, Jr. R. C., Thornley M. D., Leroy A., 2008, AJ, 136, 2563

Warren S. R. et al., 2011, ApJ, 738, 10

Weaver R., McCray R., Castor J., Shapiro P., Moore R., 1977, ApJ, 218, 377

Weiner B. J. et al., 2009, ApJ, 692, 187

Weinmann S. M., Neistein E., Dekel A., 2011, MNRAS, 417, 2737

Weinmann S. M., Pasquali A., Oppenheimer B. D., Finlator K., Mendel J. T., Crain R. A., Macciò A. V., 2012, MNRAS, 426, 2797

Weisz D. R., Skillman E. D., Cannon J. M., Dolphin A. E., Kennicutt, Jr. R. C., Lee J., Walter F., 2009a, ApJ, 704, 1538

Weisz D. R., Skillman E. D., Cannon J. M., Walter F., Brinks E., Ott J., Dolphin A. E., 2009b, ApJL, 691, L59

Whitaker K. E. et al., 2011, ApJ, 735, 86

Whitaker K. E., van Dokkum P. G., Brammer G., Franx M., 2012, ApJL, 754, L29

White S. D. M., Frenk C. S., 1991, ApJ, 379, 52

White S. D. M., Rees M. J., 1978, MNRAS, 183, 341

Wiersma R. P. C., Schaye J., Smith B. D., 2009, MNRAS, 393, 99

Wilcots E. M., Miller B. W., 1998, AJ, 116, 2363

Wilkins S. M., Trentham N., Hopkins A. M., 2008, MNRAS, 385, 687

Wilman D. J., Erwin P., 2012, ApJ, 746, 160

Wuyts S. et al., 2011, ApJ, 738, 106

Yang X., Mo H. J., van den Bosch F. C., 2003, MNRAS, 339, 1057

Zel'dovich Y. B., 1970, A&A, 5, 84

Zheng X. Z., Dole H., Bell E. F., Le Floc'h E., Rieke G. H., Rix H.-W., Schiminovich D., 2007, ApJ, 670, 301

Zwicky F., 1933, Helvetica Physica Acta, 6, 110

Acknowledgements

I would like to thank my supervisors Andrea Macciò and Greg Stinson for all their guidance and support. Thank you for answering all my questions, offering helpful comments and showing immense patience. Special thanks to Andrea for believing in my abilities and offering me an opportunity to pursue my Ph.D. at MPIA and also for providing me with an additional year of financial support. In addition I would also like to thank my collaborators Joe Hennawi, Sebastiano Cantalupo, Chris Brook, Ben Moster, Fabio Fontanot and Fabian Walter.

I am very thankful to Andrea Macciò & Volker Springel for agreeing to referee my thesis and additionally Eva Grebel and Luca Amendola for agreeing to be in the examination committee. Thanks to Jakob Herpich for his help in translating the thesis abstract into German.

Many thanks to the IMPRS coordinator Christian Fendt. I had great fun during my time here mainly thanks to the great friendships I have built with my fellow students of IMPRS generation 6.

I would like to thank my 'Amma' and 'Acha' for supporting me throughout my studies and always encouraging me to follow my dreams. Finally, a big thank you to Svetlana for all the love and affection she has shown me.